Sensing and Knowledge Mining for Structural Health Management

by

Clyde Coelho

A Dissertation Presented in Partial Fulfillment
of the Requirements for the Degree
Doctor of Philosophy

Approved June 2011 by the
Graduate Supervisory Committee:

Aditi Chattopadhyay, Chair
Lenore Dai
Tong Wu
Santanu Das
John Rajadas
Antonia Papandreou-Suppappola

ARIZONA STATE UNIVERSITY

August 2011

ABSTRACT

Current economic conditions necessitate the extension of service lives for a variety of aerospace systems. As a result, there is an increased need for structural health management (SHM) systems to increase safety, extend life, reduce maintenance costs, and minimize downtime, lowering life cycle costs for these aging systems. The implementation of such a system requires a collaborative research effort in a variety of areas such as novel sensing techniques, robust algorithms for damage interrogation, high fidelity probabilistic progressive damage models, and hybrid residual life estimation models. This dissertation focuses on the sensing and damage estimation aspects of this multidisciplinary topic for application in metallic and composite material systems.

The primary means of interrogating a structure in this work is through the use of Lamb wave propagation which works well for the thin structures used in aerospace applications. Piezoelectric transducers (PZTs) were selected for this application since they can be used as both sensors and actuators of guided waves. Placement of these transducers is an important issue in wave based approaches as Lamb waves are sensitive to changes in material properties, geometry, and boundary conditions which may obscure the presence of damage if they are not taken into account during sensor placement. The placement scheme proposed in this dissertation arranges piezoelectric transducers in a pitch-catch mode so the entire structure can be covered using a minimum number of sensors. The stress distribution of the structure is also considered so PZTs are placed in regions

where they do not fail before the host structure. In order to process the data from these transducers, advanced signal processing techniques are employed to detect the presence of damage in complex structures. To provide a better estimate of the damage for accurate life estimation, machine learning techniques are used to classify the type of damage in the structure. A data structure analysis approach is used to reduce the amount of data collected and increase computational efficiency. In the case of low velocity impact damage, fiber Bragg grating (FBG) sensors were used with a nonlinear regression tool to reconstruct the loading at the impact site.

This dissertation is dedicated to

my parents, Peter and Lynette Coelho,

for their unwavering love and support.

Without you, none of this would be possible.

ACKNOWLEDGMENTS

First and foremost, I would like to thank my advisor Dr Aditi Chattopadhyay for her guidance and support throughout my PhD. Her encouragement and high standards helped me to widen my professional horizons and achieve more than I thought I was capable of. She welcomed me into the group like I was one of her own and I will be forever grateful to her for everything she has done for me.

A special thank you to Santanu Das, first my coworker, then my committee member for helping me learn the ropes in graduate school. I would also like to acknowledge my other committee members Antonia Papandreou-Suppappola, John Rajadas, Lenore Dai, and Teresa Wu for their advice and suggestions.

I would also like to thank Kay Vasley, executive assistant of the AIMS center for all her hard work managing our research group. We would all be drowning in paper work and bureaucracy were it not for you.

Last but not least, I would like to thank all my coworkers and friends, too many to name, for your help and support both personally and professionally. I truly believe that this dissertation was a group effort and I would not have been able to complete my PhD without the unique contribution that each of you made to my life and my work.

The support of the NASA IVHM Program (NNX07AD70A), and AFOSR MURI Program (FA9550-06-1-0309), is also gratefully acknowledged.

TABLE OF CONTENTS

Page

Page

Page

Page

LIST OF TABLES

Table Page

LIST OF FIGURES

Figure Page

Figure Page

Figure Page

Figure Page

Figure Page

Chapter 1

INTRODUCTION

The economic downturn of recent years has led to a decline in U.S. spending in the defense and aerospace industry. As a result, there are fewer new military and civilian aircrafts being ordered, requiring that the existing fleet of aircraft operate well past their expected service lives. In the past, the United States Air Force (USAF) retired aircraft in order to free up capacity for newer aircraft while reallocating maintenance funds for the remainder of the aging fleet [1]. Since the number of new aircraft being ordered is insufficient to maintain the current fleet size, this has meant that older aircraft be kept in service longer. In addition to the cost of materials and training required to maintain such a large, aging fleet, maintenance capacity also needs to be expanded to handle increasing fleet servicing needs. These issues are contributing factors in determining the acceptable cost of keeping older aircraft in service [1]. Maintenance costs typically increase as a system ages; therefore, a significant change in the way aircraft fleets are maintained is required in order to keep these assets mission ready.

The current maintenance paradigm is a mix of preventative (schedule based) and corrective repair and replacement [2]. The schedule based system requires that maintenance action be taken at fixed time intervals regardless of the state of the system. Corrective maintenance is performed once a part has failed. However, this

type of maintenance can often lead to excessive system downtime, particularly if replacement parts require lead time to be procured. In the aerospace industry, the schedule based maintenance system has been the preferred mode of fleet servicing because it safeguards against failure of a critical system or subsystem that can lead to significant economic and human loss. The frequency of this type of inspection involves a trade-off between the cost of inspection and the risk of induced damage, which takes into account the expected loads and environmental conditions of the structure. Often, this design load envelope is very different from the loading that is actually seen by the structure in service. Consequently, as part of the servicing schedule, several components replaced even though they have considerable safe operating life remaining. This is because a thorough inspection is expensive and time consuming, and replacement is often a cheaper alternative.

Figure 1 shows the typical progression of damage in a structure. Initially, there may be some flaws that develop in the system that are small enough and do not affect performance or safety of the system. Current non-destructive evaluation (NDE) techniques cannot detect these flaws. Once the damage becomes detectable, the structure may show signs of degradation, but it can still be operated safely. At this point the damage grows at a relatively slow rate. Designers typically specify a critical damage type or size, at which the part must be repaired or replaced, either because the damage growth rate will increase rapidly and lead to failure, or because the performance of the system has degraded beyond a certain limit. Figure 1 shows that there could be significant savings if remedial measures were only taken prior to the damage becoming critical.

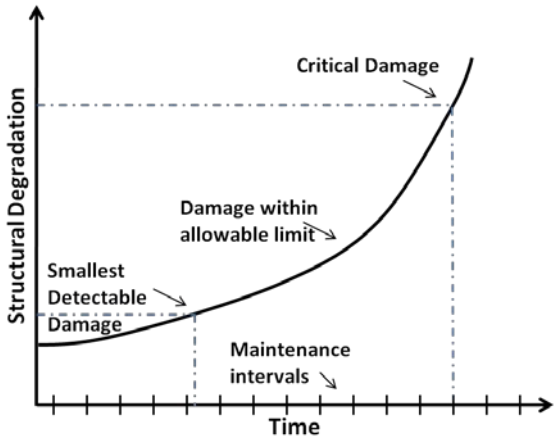

Figure 1: Typical damage state at various inspection points.

Condition based maintenance (CBM) is the process of using the actual state of the system to schedule repairs and maintain performance. If implemented, such a system has the potential to dramatically reduce life cycle cost, improve safety, and reduce weight since components could be designs using reduced margins. CBM also increases productivity since the system would have less down time due to unnecessary maintenance. The logistics enterprise required to maintain a large fleet can also be streamlined so that parts can be ordered and delivered just before they are needed, reducing inventory cost and lead time. A comparison of the traditional maintenance approaches with CBM [2] is presented in Table 1.

The prospect of reductions in maintenance cost and time due to CBM has made structural health management (SHM) research a priority for the aerospace community. SHM is the process of detecting, classifying, localizing, and quantifying damage for residual life estimation. One aspect of SHM is implementing traditional NDE approaches within a framework for *in situ*, real-

time damage assessment. To accurately assess damage information from onboard sensors, traditional NDE, performance metrics, and load (mechanical and environmental) histories must be mined to estimate the current state of the system and predict its safe operating life.

Aircraft, rotorcraft, spacecraft, industrial equipment, and civil infrastructure already have sensors in place that monitor a host of environmental and performance metrics. One method for determining the degradation of a structure is using various data analysis techniques that will

i. perform a trend analysis to check for performance decline, possibly indicating damage.
ii. check if any parameters have crossed thresholds defined by experts.
iii. determine if there is a pattern in the data that corresponds to damage as observed in other similar systems.

The aforementioned data analysis techniques can only provide a short window for preventative maintenance since detection using these approaches requires an appreciable degradation of the system.

Table 1: Pros and cons of different maintenance paradigms

	Corrective Maintenance	Scheduled Maintenance	Condition based maintenance
PROS	Fewer maintanance checks	Easier to plan maintanance budget	Avoid unexpected failure
	No cost/weight penalty for CBM equipment	Greater chance of catching damage before failure	Parts ordered to minimize storage cost & lead time
		Standardized maintenance procedure	Maintenance performed when convenient
		Logistical planning easier for fleet maintenance	Equipment life extended
			No unnecessary maintenance
CONS	Noticeable degradation before maintenance	Maintenance when no faults present	Cost/weight penalty for CBM hardware
	Unpredictable fleet readiness	Unexpected failures still possible	
	High cost/lead time for spare parts	Parts inventory cost	
	Safety hazard		
	Increased labor time/cost		

Since existing sensors and data analysis tools are insufficient for early detection and accurate prognosis, the SHM research community is developing new sensing technologies to measure more useful system parameters and new algorithms to

understand this information, making residual useful life predictions [3] more accurate.

This research focuses on sensor placement techniques and on mining the data from these sensors for damage state awareness. The process of damage interrogation involves a) determining whether sensor information indicates presence of damage, and b) once damage is detected, conducting further analysis to assess damage type and location. Based on information gleaned from these two steps, the state of the system can be assessed and then presented in terms of simple damage metrics. Figure 2 shows the procedure involved in identifying damage in a part or structure.

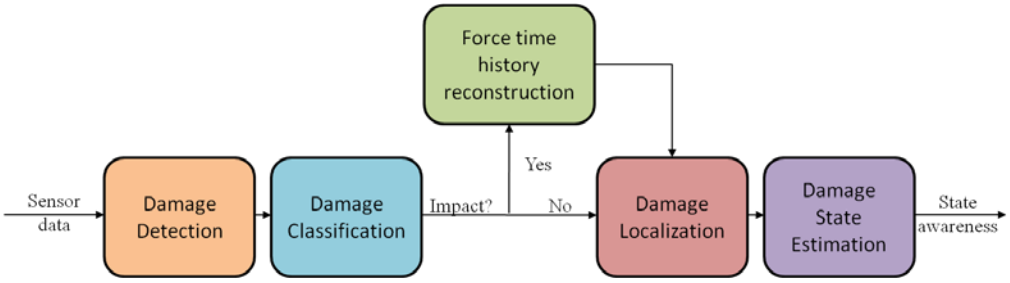

Figure 2: Typical damage detection and identification process.

In this work, the SHM process will be viewed in terms of statistical pattern recognition where the response of a system due to known or unknown loading will be studied and compared against examples of healthy and damaged configurations. For many complex engineering systems, uncertainty and variability in boundary conditions, material properties, mechanical and environmental loading combined with noise can cause large changes in measured

responses that may not indicate the presence of damage. Since there is no way to quantify all these benign signal variations, statistical tools need to be employed to make it easier to interrogate large structures with increased speed and accuracy. The different aspects of damage interrogation will be discussed in the following sections.

1.1. Optimal Sensor Placement

A significant amount of research is being conducted on damage detection techniques and sensors for SHM applications. However, the performance of these approaches is highly dependent on the quality of the information obtained by the sensors. In order to detect damage with maximum efficiency, the sensors need to be placed optimally so that information pertaining to damage in a structure can be quantified with a high degree of confidence. The sensor placement must also address the global requirement that damage in any part of the structure can be detected to prevent failure under service conditions. Since a major deciding factor for the implementation of SHM systems in aerospace structures is cost and weight, approaches for sensor placement must balance the need for redundancy with the associated weight penalty of having many sensors.

A robust SHM framework would require the installation of a distributed sensor network that would enable rapid and frequent damage measurements without significant effort or expense. Several types of sensor networks have been investigated thus far, including strain gauges [4], accelerometers[5], piezo-transducers [6], and fiber optic sensors [7]. Strain gauges, as the name suggests,

measure the resulting strain at a point on a structure due to an applied load. Strain gauges are typically used to check if a structure is deforming more than allowable tolerance, indicating the presence of damage. These sensors are limited in their resolution and sampling frequency, and the point strain information they provide cannot be used to parameterize damage except in very simple structures. Accelerometers can provide a more global view of damage in a structure, but existing technologies are unable to detect the presence of small damage. Another drawback of this type of sensing approach is that significant energy input is required to excite large structures at different frequencies. Piezoelectric transducers show considerable promise for structural monitoring because they use the concept of guided wave based interrogation which can be used to inspect relatively large areas with high fidelity. Another benefit is that the transducers can act as both actuators and sensors, eliminating the need for extra actuation hardware. Data from these sensors provide a lot of information about a structure and can be used to identify, classify, localize, and quantify faults. Fiber Bragg grating (FBG) sensors are advantageous because they can be tailored to include multiple sensors on a single fiber, resulting in a significant weight advantage when implemented on a large structure. Also, FBG sensors are low weight, require minimal space, and are immune to electromagnetic interference, which is a concern in the harsh operating environments of aerospace structures. FBGs are able to provide very high resolution strain measurements and can be embedded in composite systems eliminating sensor-host bonding issues. Since piezoelectric transducers can yield the most information about a structure, they were chosen for

the damage identification research being presented in this dissertation. In addition, FBG sensors were used for impact studies to reconstruct the loading during a low velocity impact.

A substantial amount of literature exists on the issue of sensor placement for wave based SHM. Worden and Burrows [8] developed a technique for placing passive sensors on a structure for detecting damage. This approach used bio-inspired optimization algorithms for placing the sensors to detect modal changes due to damage. Using evolutionary algorithms, Gao and Rose [9] placed transducers for detecting changes in the Lamb wave propagation due to the presence of damage. Their approach focused on sensor networks operating in a pulse echo mode and on minimizing the probability of missed detection. Lee and Staszewski's approach [10] involved placing piezoelectric sensors using a physical understanding of the wave propagation behavior in a structure. This approach requires modeling the structure before and after the introduction of damage and observing the change in wave propagation characteristics. Sensors were then placed in locations where the change in the signal before and after the damage was at its maximum. This approach requires the user to have an idea of the possible damage type and location in the structure, which may not always be possible in real applications. Das et al. [11] placed sensors based on the concept of minimum sensing distance. This passive sensor placement approach considered the maximum distance a perturbation could travel due to damage, but it did not address the excitation energy necessary to produce an acceptable perturbation level. This work was then extended by Soni et al. [12] to include the stress

distribution in the structure to identify the hotspots. A hotspot is a region or component of a structure where the probability for damage to occur is high. Sensors could then be biased to regions of higher stress where damage was more likely to initiate. Flynn and Todd [13-14] designed a sensor placement scheme that incorporates a statistical model of the active sensing approach and takes into account the line of sight between the sensors.

The work presented in this dissertation places sensors so that the entire structure can be interrogated using an active wave based technique with a user-defined probability of false alarm. Loading conditions for the component are taken into account to ensure that sensors are not placed in regions of high stress where they can fail or become debonded. The features used to identify damage are based on conversion of Lamb wave modes due to damage. A simulated annealing based optimization algorithm is used to find the minimum number of sensors required for reliable SHM.

1.2. Information Management

The aerospace systems and civil infrastructure that would benefit from SHM systems typically remain in service from years to decades. This means that the continuous monitoring of these systems would generate massive amounts of data that need to be stored and processed. With typical structures, there will be a lot of uninteresting information that is collected when the structure is healthy followed by short bursts of useful information as damage is introduced in the structure. For this reason it maybe be beneficial to remove redundant information or maintain

information about the system at an aggregate level [15]. One option to reduce the amount of data that is collected over the life of the structure is to switch to an active interrogation approach at discrete intervals. While this does reduce the amount of collected data significantly, it can still produce a lot of data depending on the frequency of interrogation. Within the active interrogation framework, the ideal way to control the amount of data being generated would be by making decisions at the individual sensing nodes and storing only the structural state at the current time. Unfortunately, with current technology, it is not possible to instrument processing units at each node without increasing the weight and power requirement of the entire system. Also, if further processing needed to be performed on some anomalous data, it would not be available. As a result, the information management work in this dissertation focuses on reducing the amount of data after feature extraction in an attempt to increase the computational efficiency of the damage identification tools and reduce the amount of redundant data that needs to be stored.

1.3. Damage Detection

A principal objective of SHM is to be able to detect the presence of defects close to the nucleation stage in order to take measures that avoid system or sub-system level failure. Typical NDE techniques, such as the liquid penetrant inspection method, eddy current and optical microscope inspection [16] can detect fairly small damage especially in metallic structures; however, they require that components or structures be taken out of service and disassembled for inspection. For composite specimens, a variety of NDE techniques exist, such as ultrasonic c-

scanning [17], pulsed thermography [18] and acoustic emission [19] that provide reliable ways of inspecting for damage, however, they too require that internal components be removed for inspection. One method for inspecting a structure for damage is through the use of modal analysis [20], which allows users to estimate the state of a structure based on changes on modal properties that could be caused by damage. There are two issues with this approach that prevent it from being adopted for aerospace structures. The first is the fact that induced damage must be significant before it can be reliably detected using this approach. The other is the shift is modal properties that is observed with change in temperature. In a study of modal properties on the Alamosa Canyon bridge [20], it was found that uneven heating of the bridge caused by the position of the sun resulted in modal changes. Since the position of the sun varies with the seasons and time of day, it is possible that change due to damage could be ignored or that changes due to environmental factors could be mistaken for damage.

Another approach that has been widely adopted by the research community is the use of guided wave propagation to inspect structures for flaws. Wave based techniques are well-suited for this task because sensors can be surface mounted; they do not require much support equipment and the technique works on complex geometry. Passive techniques [21-22] may not be as efficient as active techniques because the frequency of operation of the system may not be the best frequency with which to excite the damage that is present and obtain a sufficiently large response. Also, the ideal frequency for exciting the damage may change as the damage evolves [23]. Active wave based techniques [6, 11, 24-26] are

advantageous because they allow the user to select a somewhat narrow band of frequencies with which to excite the structure depending on the scale of the defect. This allows customization of the input signals for the different types of damage that are expected to occur in the structure.

Finally, the most crucial part of structural health monitoring is the efficient and accurate analysis of the data collected by the sensors. There are many algorithms currently being used for damage detection [4, 6, 23, 27-33], the most common of which are cepstrum analysis, kurtosis, time-domain averaging, crest factor analysis, envelope detection, high frequency resonance technique, discrete cosine transform, neural networks, and matching pursuit decomposition (MPD).

In this dissertation, one-class Support Vector Machines (SVMs) [34] was used as a pattern recognition algorithm that looks for anomalous changes in the sensor signal arising from damage in complex metallic geometries [35]. SVMs are a set of related learning methods that analyze data and recognize patterns and are used for classification and regression analysis. The advantage of using these methods for classification is that they produce reasonably accurate results while using only a fraction of the computational time of other commonly used algorithms [36-38].

SVMs belong to a class of data driven methods that can be supervised or unsupervised in nature, based on the way they are trained on the available historical data. In an unsupervised learning technique, the model experiences the nominal behavior of the system and would be capable of identifying unseen abnormalities, if they occur. However, in supervised learning it is assumed that

the given system features have already been classified by a human expert into *m* of *n* categories, based on some prior knowledge, and the training is performed on all possible categories. The drawback of this method is that every possible behavior for a system must be known for accurate classification, which is not practical for real world problems where an infinite number of off-normal behaviors can exist. Since the specimens being used in this dissertation for damage detection are complex, an unsupervised detection scheme was used. This means that the algorithm is trained only with the dataset or attributes extracted from those datasets that characterize the normal behavior of the system, which are then considered as 'observed' features.

The one-class SVM, an unsupervised technique used in this study, utilizes only the nominal state of the system while looking for different fault modes that may occur during its operation. SVM techniques make the classification problem easier by converting a classification problem that is difficult in some input space into a higher dimensional space where a class separatrix can be generated more easily. Although there are multiple ways to map data into different feature spaces, the Radial Basis Function (RBF) kernel is the most popular in machine learning applications [36-37].

1.4. Damage Classification

In certain hotspot applications, the different types of damage that can occur in the structure are known, usually from examples of similar components that have failed in the past. Using this information, it is possible to take sensor data from a

structure and categorize it as being healthy or belonging to a particular damage class. Knowing the type of damage in a structure is useful because different damages grow at different rates, and this information can help in the prediction of residual useful life. Damage classification involves the characterization and identification of the key damage-related features, which can be used within a structural health monitoring (SHM) framework as damage indicators and differentiators. Physics-based modeling techniques can be used to accurately characterize the interaction of the actuation-induced stress wave with a given damage and sample type in order to determine the sensor output [39]. The drawback of this approach is that it is computationally expensive to model all the expected damage scenarios for a particular part and moreover, does not account for imperfections in the material and sensors, unexpected damage, and ambient noise. Also, it is very difficult to solve the inverse problem of finding the change in the system due to damage using the sensor signal alone.

The methodology used for this research is a data-driven approach [6] that uses examples of actual signals from sensors that have been categorized by experts, and also uses these signals as a guide to identify similar damage types. It is assumed that the training data collected from every class of damage contains information within the signals that relates to the wave-damage interaction. Although this method requires a large database of training signals, it takes into account all the variations that are not accounted for in physics based models.

To classify the type of damage in a structure, another application of SVMs have been utilized. SVMs have a strong mathematical foundation [34] and show good generalization when applied to classification problems in a number of fields. Traditional approaches to the classification of multiclass problems have been conducted in the form of ‘one versus one’, ‘one versus rest’, hybrid [37, 40], and clustering [41] algorithms. In ‘one versus one’, the amount of training time required is very large since $k(k-1)/2$ classifiers need to be constructed for a k class problem. For a ‘one versus rest’ scheme, a problem involving k classes of data will require the construction of k classifiers. One problem with the latter case is that each classifier will require the use of the entire training set, which becomes computationally intractable. For both methods, a voting scheme is used in which the classifier that scores the highest for a given data set assigns all the points in that particular set to a given class. Also, in such a case, it is very difficult to decide which class the test data belongs to if two classifiers have similar scores. Clustering schemes are able to learn signal characteristics well and can decide the uniqueness of different classes (or even classes within classes) based on the clustering of data points in a hyperspace. While this approach is promising for damage detection scenarios where all possible damage types cannot be known, the computational expense involved with determining cluster boundaries increases exponentially with the increase in training sets.

This research presents a framework for damage classification that applies a ‘one versus rest’ scheme [42] organized into a binary tree structure that addresses some of the computational issues associated with a large number of classes by reducing

the total number of required classifiers. The novelty of this approach over traditional SVM schemes is twofold. First, it allows the user to prioritize damage cases, making it quicker to identify common or expected damage states. Second, by organizing classifiers correctly, it is possible to simultaneously reduce the number of classifiers necessary as well as the complexity of each classifier. The research presented here shows that this scheme works well for these types of applications.

1.5. Load History Reconstruction for Impact Damage

Survivability of composite structures subjected to dynamic contact loads is of critical importance in many aerospace applications. Low velocity impacts can result in subsurface delamination that cannot be detected using visual surface inspection even though the delamination results in stiffness degradation and a significant loss in structural integrity, especially in thick composites. Impact damage is also highly dependent on the mass, shape, and velocity of the impacting objects.

Due to the weight savings and embedding capability associated with FBG sensors, they were chosen as the sensing system for the study of low velocity impact damage in composites. However, since these sensors only measure strain along the length of the fiber, a prediction scheme that can estimate location and loading using randomly oriented and dispersed sensors is key to damage state awareness. This could reduce installation time and the total number of sensors required to interrogate a complex structure. Unexpected impact loading on an aerospace

structure can often lead to catastrophic failure. Therefore, a passive detection approach [21] is required to ensure that the structure can be constantly monitored and the operator notified immediately if there is an adverse event. A framework that detects the location and estimates the strains induced at the point of impact will allow users to conduct a detailed structural analysis and decide whether to take immediate action or schedule maintenance at a later date.

The work presented in this dissertation focuses on estimating the loading generated in a structure during an impact. Although several approaches exist to determine the location of an impact, only a few provide force-time history reconstruction of the impact event. One method to localize damage uses the guided waves that are emitted from the source of the impact. This method requires explicit knowledge of wave speed, which works relatively well for homogenous structures [43]. In composites, however, the wave propagation speed varies as a function of direction [44], which makes localization more difficult and this approach cannot be used to estimate the induced strains. Kim and Lee [45-46] used a Green's function approach to localize damage in an aluminum plate and reconstruct the load history. This approach assumes an infinite plate when solving for the transfer function between the impact location and sensor response. This same transfer function is used for the recovery of impact load, which means it may not be applicable to small and/or complex structures. Park and Chang [47] proposed a system identification technique that is based on training data from an experiment. Since the designed transfer function does not require a physical model, it represents the observed system response more accurately. However, the

structural deformation must be linearly elastic during the impact process, and the deformation of the structure must be small enough to neglect geometric nonlinearity. The approach used in this paper uses a machine learning technique to take data from experimental or modeling data and use it to build a model that can reconstruct the load history as a function of time. The support vector regression (SVR) technique, based on the popular support vector machines classifier [48], and applied in other fields for time series prediction [49-50], was chosen because it performs well with high dimensional data sets and does not require extremely large training sets for generalization. Using the FBG sensor signals from finite element simulations and a time delay approach, impact force-time curves at the point of impact were estimated. The objective of this work is to build a data-driven framework that can accurately estimate the impact load at random locations even in the absence of complete strain information.

1.6. Objectives

The objectives of this dissertation are as follows:

1. Develop a framework for placing piezoelectric actuators and sensors on a structure for damage interrogation. The resulting framework will allow the user to detect a predefined minimum damage in a structure with a minimum probability of false alarm using the minimum number of sensors. Placement of sensors in high stress regions where failure of the sensors or bonding layer might occur will be avoided.

2. Use advanced signal processing techniques to extract features from sensor signal that provide the most information regarding the state of the system.
3. Manage data from sensors in order to reduce storage cost and improve computational efficiency of the SHM algorithms.
4. Detect the presence of damage in complex structures and classify it accurately and efficiently.
5. In the case of impact loading, reconstruct the load history at the point of impact using randomly dispersed strain measurements so that further analysis regarding the severity of the impact can be conducted.

1.7. Outline of the Dissertation

This dissertation contains 7 chapters and is organized as follows:

Chapter 2 presents a framework for placing piezoelectric transducers on a structure for guided wave based damage interrogation. By determining the sensing region of a pair of transducers for an acceptable probability of false alarm, various placement options can be tested to check the amount of sensor coverage and redundancy. In order to increase the durability of the sensors, the stress distribution of the structure is also taken into account so that sensors are placed in low stress areas. A simulated annealing approach was used to perform the optimization and provide an optimal arrangement of transducers on complex geometries.

Chapter 3 presents a kernel based method to diagnose structural defects. Using time delay embedding features, a one class SVM algorithm was used to identify

anomalies in sensing signals that might indicate the presence of damage. Since minor changes are expected due to noise and changing environmental conditions, a novel scheme is implemented that uses this one class approach to determine if changes in the signal are significant enough to be considered a different class. This approach is tested for damage detection in bolted joints subjected to fatigue loading.

Chapter 4 discusses the classification of damage in both metallic and composite test specimens. Using an SVM classifier organized in a binary tree approach, the number of classifiers that need be built is reduced which could result in computational savings for large problems. The features that were used for classification were generated using matching pursuit decomposition, a time frequency signal processing tool that decomposes signals into a linear combination of atoms that have a physical meaning and can be used for the assessment of damage.

Chapter 5 addresses the problem of information management for long term SHM. The signal features used were generated using a modified linear discriminant analysis (LDA) technique. The resulting features were analyzed based on their geometric properties in the feature space and then reduced by removing data that did not contribute any class discriminatory information. The approach was demonstrated on data obtained from testing on different metal and composite specimens.

Chapter 6 focuses on determining the load as a function of time for low velocity impacts. FBG sensors were used in this study and they provided only one component of the strain at the sensor locations. A support vector regression framework was developed to take the incomplete strain information from the sensors and use it to predict the loads at the impact site. Validation for this study was carried out using ABAQUS simulated data and experimental testing on a composite wing.

Chapter 7 summarizes the research work and highlights the unique contributions of this dissertation in the area of SHM. The future work that needs to be accomplished before these techniques can be implemented is also discussed.

Chapter 2

SENSOR PLACEMENT FOR WAVE BASED DAMAGE INTERROGATION

With research in structural health monitoring (SHM) moving towards increasingly complex structures for damage interrogation, the placement of sensors is becoming a key issue in the performance of the damage detection methodologies. For ultrasonic wave based approaches, this is especially important because of the sensitivity of the travelling Lamb waves to material properties, geometry, and boundary conditions that may obscure the presence of damage if they are not taken into account during sensor placement. The framework proposed in this chapter defines a sensing region for a pair of piezoelectric transducers in a pitch-catch damage detection approach by taking into account the material attenuation and probability of false alarm. Using information about the region interrogated by a sensor-actuator pair, a simulated annealing optimization framework is implemented in order to place sensors on complex metallic geometries such that a selected minimum damage type and size could be detected with an acceptable probability of false alarm anywhere on the structure. The stress distribution of a component subjected to some known loading is also taken into consideration to ensure that sensors are biased towards regions of low stress where the possibility of damage to the sensor or bonding layer is minimal. This approach is demonstrated on a lug joint for crack detection and on a large Naval SHM test bed where the resulting sensor placement allowed for interrogation of all parts of the structure using the minimum number of transducers.

This chapter is organized as follows. Section 2.1 discusses issues that must be considered when trying to implement a sensor network for damage detection using Lamb waves. Sections 2.2 and 2.3 present a theoretical background on the methods used to determine the sensing region for a pair of transducers and optimization scheme. The effectiveness of the sensor placement scheme on some selected SHM test articles is demonstrated in section 2.4.

2.1. Sensor Placement Issues

There are several issues that need to be addressed when placing sensors on complex service structures. Figure 3 lists some of the more important issues associated with implementing a sensor network. Each of the listed issues is interrelated and must be considered together for a given structure.

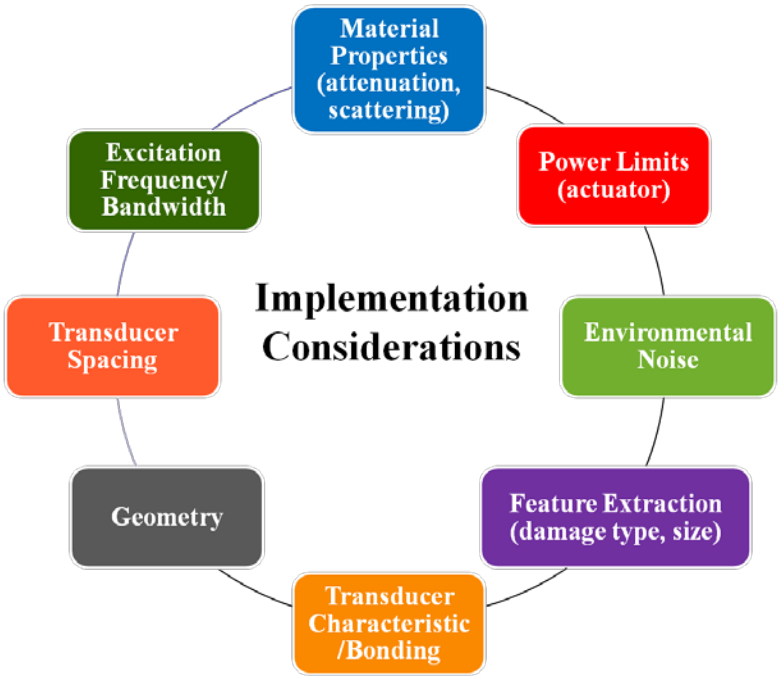

Figure 3: Issues affecting performance of a sensor network.

2.1.1. Effect of Material Properties

The behavior of the material being interrogated is the first and possibly the most important factor in deciding the type of sensors and mode of damage detection. For wave based interrogation in homogenous material systems, the induced strain wave can travel with the same speed and attenuation in all directions. In the case of a heterogenous system such as carbon fiber composites, the guided wave travels slower and sees more attenuation when it travels perpendicular to the fiber direction. The opposite is true for a wave travelling along the fiber direction. The attenuation of the travelling wave is also a function of the material properties.

2.1.2. Excitation Energy

The energy of the excitation used to excite a structure determines the size of the interrogation region. Excitations that are very low in energy can only interrogate small areas and in some cases, the energy may not be sufficient to produce a measurable change in the response of the system. For sensing systems that use mechanical exciters, injecting too much energy into the system could itself cause damage. For the piezoelectric transducers used in this work, the maximum energy that can be used for excitation is limited by the power supply and the physical limitations of the piezoelectric material. For this reason, an acceptable excitation level must be specified before transducers can be placed in optimum locations.

2.1.3. Background Noise

Every sensor measurement contains some inherent error due to background noise. If the noise level is high, the signal that is being measured has larger error. In

some cases, if the noise level is too high, the signal can be completely masked by the noise. In the case of wave based interrogation, the guided wave attenuates as it travels through the media, and there is a point when it can no longer be distinguished from the noise, which can vary based on the environment and operating condition of the system. If an onboard monitoring system is to be implemented, it needs to be able to detect damage under any expected operating condition. The key to making this possible is to determine the worst case scenario and ensure that the sensing system meets the design criteria in those conditions.

2.1.4. Excitation Frequency

In an active detection framework, the frequency of excitation is an important parameter that can affect resolution and performance. Figure 4 shows the dispersion curves for Lamb wave propagation in an aluminum plate. It can be seen that for a single excitation at a given frequency, multiple modes can be generated in the structure with the number of modes increasing with frequency. Typically, it is possible to detect smaller damages using high frequency Lamb waves. However, at high frequencies, since more modes are generated in the structure, it is more difficult to analyze changes in the signal. Also, the varying phase velocities for each of the excited modes causes a distortion of the wave packets making it more difficult to discern the presence of additional modes due to damage or other types of changes in the signal. For the work presented in this dissertation, an excitation frequency range was selected such that only the a_0 and s_0 modes were excited. Within the range of frequencies where only a_0 and s_0 were

present, the frequency that produced the highest response from the piezoelectric transducers was selected as the central frequency of the induced burst excitation.

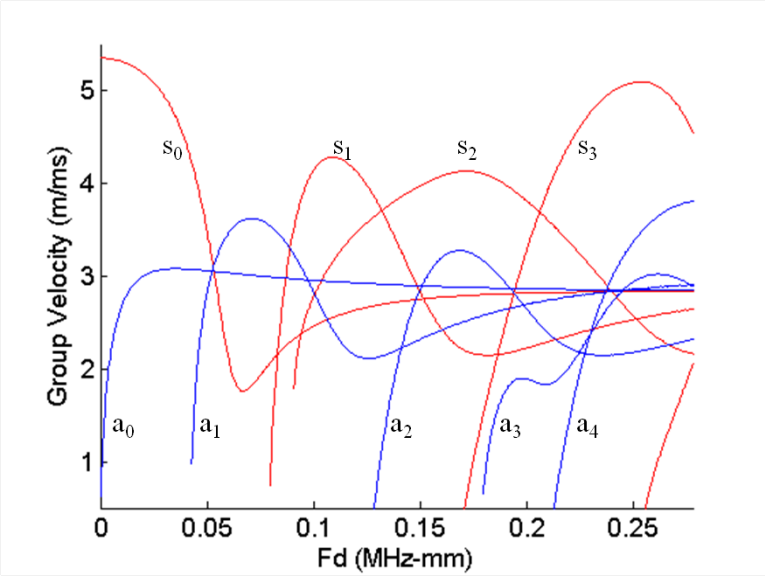

(a)

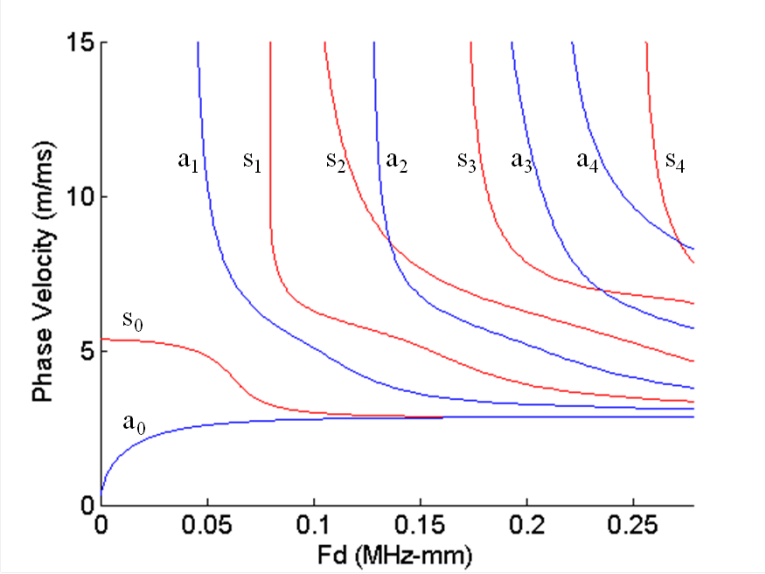

(b)

Figure 4: Dispersion curves for aluminum (a) group velocity curves, (b) phase velocity curves.

2.1.5. Signal Features for Damage Interrogation

There are many different types of signal features that can be used to indicate changes in sensor readings caused by damage. Each of these features will have different sensitivities to changes in damage type and size. Therefore, it is important to ascertain the type of features that will be extracted ahead of time so that the sensitivity of these features under different damage cases and environments can be evaluated. For the work in this chapter, the types of damage being studied behave like through thickness asymmetries to a propagating Lamb wave, resulting in the generation of additional modes in the structure. The signal features that were used attempted to capture this phenomenon. In the case of crack damage, the crack tip acts as a source of asymmetry (or thickness change) that causes mode conversion. The effect of thickness on Lamb wave propagation is illustrated in Figure 5. At a given product of frequency and thickness (fd_1), a_0 and s_0 modes are generated. For the sake of simplicity, the concept of mode conversion will be illustrated in Figure 5 using only the s_0 mode. Without any changes in thickness, this mode travels through the structure at a constant group and phase velocity. If a through-thickness asymmetry is encountered, it acts as a thickness change for the traveling s_0 mode, and the energy of the s_0 (at fd_1) mode is used to generate an a_0, s_0 and a_1 mode (at fd_2). The detection of these unexpected modes can be used to detect the presence of damage.

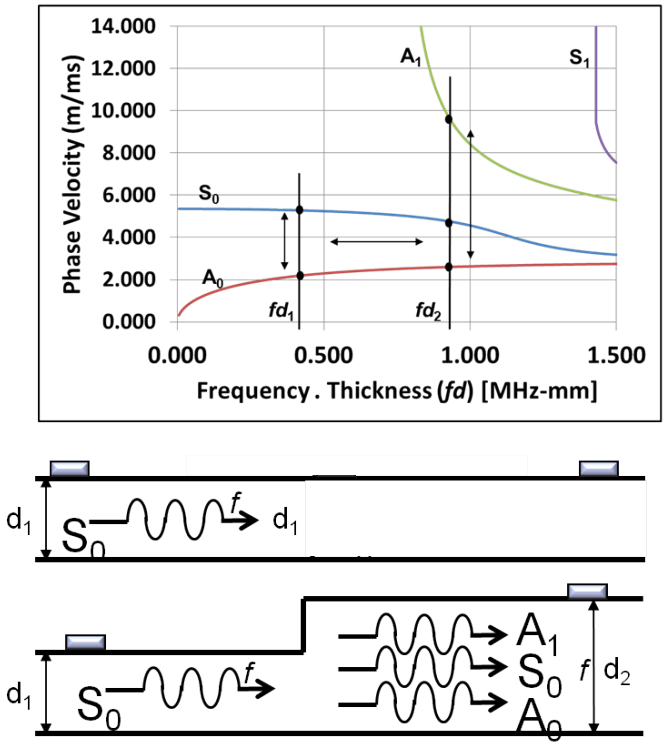

Figure 5: Effect of thickness change on Lamb wave propagation

2.1.6. Transducer Bonding, Spacing and Structural Geometry Considerations

As mentioned in the previous section, the presence of geometric variations can produce additional modes in the sensing signals. These effects need to be considered prior to interrogating a structure. For example, if a structure has varying thickness, it may be prudent to select an actuation frequency such that a minimum number of modes are excited in the thickest part of the structure. Figure 5 shows that an increase in thickness (with constant frequency) can lead to additional modes being generated. However, if the frequency is selected such that the maximum $f.d$ results in only two modes being generated, then for any thinner section of the structure, no additional modes will be created. The locations of all the boundaries also need to be taken into consideration when placing transducers.

If transducers are placed too close together, all the modes may arrive very close together making it very difficult to discern expected from unexpected modes. In order to monitor aerospace systems that are in service for long periods in varying conditions, the quality of the bonding between the sensor and the host structure is a critical issue. Current bonding methodologies for smart sensors are unable to provide the required durability characteristics. This results in sensors debonding or failing before the structure. In such cases, information from these compromised sensors could indicate that maintenance is required for a healthy structure or cause the missed detection of real damage.

2.2. Sensing Region

In wave based damage detection, the first step towards optimal sensor placement is to determine the region in a structure that can be interrogated by an actuator-sensor pair. This region depends on a number of factors, including transducer excitation frequency/bandwidth, actuation energy, and host structure properties. To address this, the first step is to experimentally determine the signal attenuation at a set frequency for the Al 6061-T651 material, which is used in both test structures. The excitation signal is a Gaussian windowed sine wave with a central frequency of 200 kHz. This excitation frequency was chosen because the APC 850 type lead zirconate titanate (PZT) transducers that were used in this experiment showed acceptable actuation energies at this frequency. This frequency also resulted in clear damage features being introduced into the signal for the damage cases that were investigated. A collocated transducer approach is used to extract features from the signal that result from the introduction of

damage to the structure. Since the damage induced in the structure causes mode conversion, a time frequency based signal analysis approach, such as the matching pursuit decomposition (MPD) technique [51], can also be used to extract the converted modes. However, the collocated sensor approach used provides a simple way to extract the modes without the wave mode approximation errors that occur with MPD. Once the damage modes are extracted, the amount of the symmetric (S_0) excitation mode that gets converted into an antisymmetric mode (A_0) is calculated and the maximum sensing region is calculated. The theoretical formulation of this approach is presented in the following subsections.

2.2.1 Threshold voltage and attenuation calculation

In this approach, the sensing region for a transducer is calculated based on an acceptable probability of false alarm (P_{fa}) [12] which is given by,

$$P_{fa} = e^{\left(-\frac{V_{th}^2}{\sigma^2}\right)} \tag{1}$$

where V_{th} is the threshold voltage or the perturbation in the sensor signal caused by damage and σ^2 is the variance of the background noise. As the perturbation due to damage gets closer to the background noise level, P_{fa} increases. In the present case, the background noise level was measured, and an acceptable probability of false alarm was set at 0.01% and the voltage threshold was calculated. This implies that any signal below this voltage cannot be reliably sensed.

Next, the attenuation in the media must be calculated to determine how far the excited and converted Lamb wave modes can travel before they drop below the voltage threshold. Figure 6 shows the setup of the PZT actuators and sensors used to conduct this study. To take into account the bond quality and the variation in the electromechanical property of the PZT transducers, actuator A2, which is equidistant from sensors S1 and S2, was used to excite the structure (Figure 6). Since both sensors should receive the same signal from A2, the effects due to actuator/structure coupling are eliminated. The sensor information can be used to quantify the relative differences in the received signal due to the difference in electromechanical property of the sensors and the sensor/host bond quality itself. The energy ratio of the sensors can be related using the following.

$$\frac{\sum_{n=0}^{N-1} E_{S1_{A2}}^{n}}{\sum_{n=0}^{N-1} E_{S2_{A2}}^{n}} = \left(\frac{T_{me1}}{T_{me2}}\right)^{2} \tag{2}$$

where $\sum_{n=0}^{N-1} E_{S1_{A2}}^{n}$ and $\sum_{n=0}^{N-1} E_{S2_{A2}}^{n}$ represent the total energy received from actuators by S1 and S2, respectively, determined over N time intervals, and T_{me1} and T_{me2} are the transfer functions for sensor 1 and 2, respectively. Since the differences in sensor properties have now been quantified, the attenuation coefficient (α) and energy ratio of the sensor signals between S1 and S2 (Figure 6) can be found using the following relations:

$$\frac{\sum_{n=0}^{N-1} E_{S1_{A2}}^{n}}{\sum_{n=0}^{N-1} E_{S2_{A2}}^{n}} = \left(\frac{T_{me1}}{T_{me2}}\right)^{2} e^{-2\alpha|R_{AS1}-R_{AS2}|} \tag{3}$$

$$\alpha = -\frac{1}{2|R_{AS1} - R_{AS2}|} \ln\left(\frac{\sum_{n=0}^{N-1} E_{S1_{A1}}^{n} \sum_{n=0}^{N-1} E_{S2_{A1}}^{n}}{\sum_{n=0}^{N-1} E_{S2_{A2}}^{n} \sum_{n=0}^{N-1} E_{S1_{A2}}^{n}}\right) \quad (4)$$

where R_{AS1} and R_{AS2} are the distances from the actuator to sensors as shown in Figure 6. For this study, the attenuation coefficient (α) was calculated to be 0.693 in^{-1}.

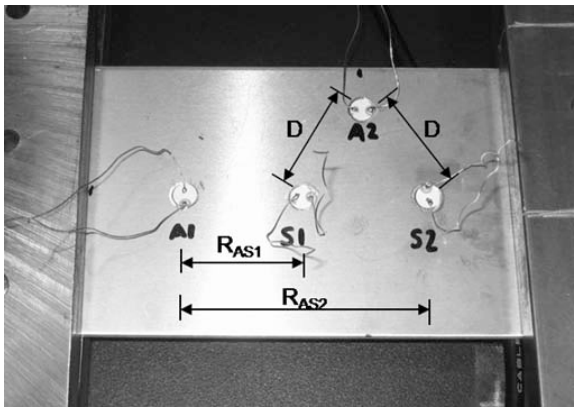

Figure 6: Setup for attenuation measurement.

2.2.2 Calculation of energy conversion for Lamb wave modes

If Lamb waves propagating along a thin plate encounter a discontinuity point such as an open crack, then some portion of the transmitted Lamb wave modes will be converted into other modes. For example, when a S_0 mode arrives at the discontinuity, the transmitted wave is separated into S_0 and A_0 modes (denoted as S_0/S_0 and A_0/S_0, respectively). In a similar manner, an A_0 mode is also divided into S_0 and A_0 modes (S_0/A_0 and A_0/A_0).

The first arrivals of the additional modes due to mode conversion occur between the S_0 and A_0 modes when a notch is located between the exciting and sensing PZT transducers. Figure 7 schematically shows the relative arrival times and phases of various modes generated and sensed using the illustrated actuator/sensor pair. In Figure 7, signal AB denotes a measured Lamb wave signal from PZT A to PZT B. Signals AC, DB, and DC are defined similarly.

Ideally, signals AB and DC (or signals AC and DB) should be the same because the converted Lamb wave modes (S_0/A_0 and A_0/S_0) do not appear in the absence of damage as shown in Figure 7 (a). However, these conditions are no longer valid when the notch is formed because the phases of the converted Lamb wave modes are totally different between signals AB and DC (or signals AC and DB). Based on this finding, Equation (5) was introduced to achieve full decomposition of individual Lamb wave modes from measured Lamb wave signals.

$$\begin{bmatrix} \text{Signal } S_0 \\ \text{Signal } MC_2 \\ \text{Signal } MC_1 \\ \text{Signal } A_0 \end{bmatrix} = \frac{1}{4}\begin{bmatrix} 1 & 1 & 1 & 1 \\ 1 & 1 & -1 & -1 \\ 1 & -1 & 1 & -1 \\ 1 & -1 & -1 & 1 \end{bmatrix}\begin{bmatrix} \text{Signal AB} \\ \text{Signal AC} \\ \text{Signal DB} \\ \text{Signal DC} \end{bmatrix} \tag{5}$$

Note that signal MC_1 will contain only the S_0/A_0 mode (the S_0 mode converted from the A_0 mode) in the presence of damage while signal MC_2 includes the A_0/S_0 mode only. By monitoring the appearance of converted modes in signals MC_1 and MC_2, the presence of damage can be identified.

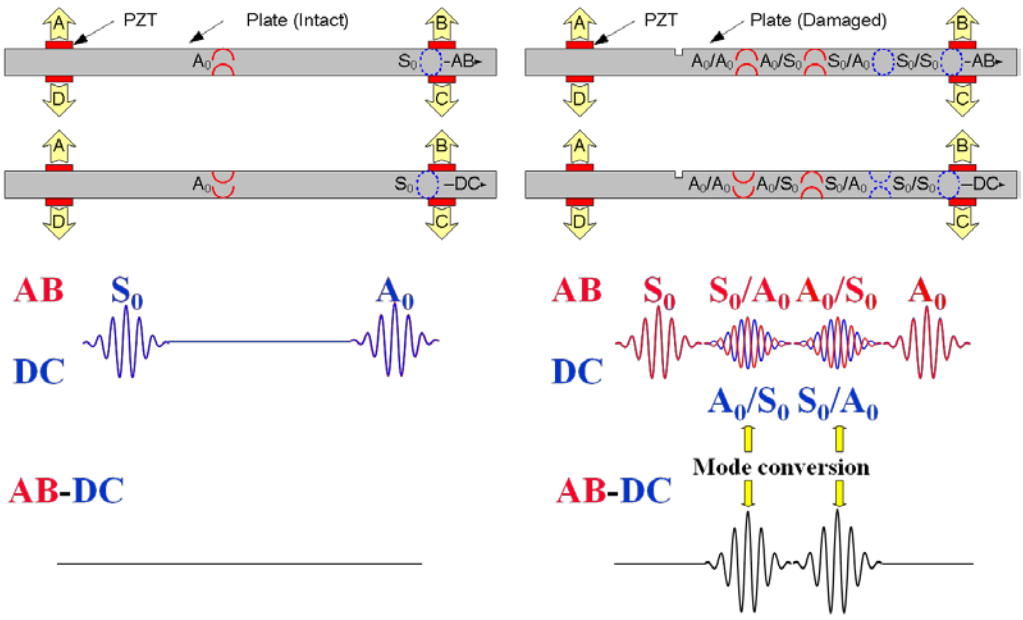

(a) Relative phases of individual Lamb wave modes in a healthy plate

(b) Relative phases of individual Lamb wave modes in a damaged plate

Figure 7: Determination of mode converted waves due to damage using collocated transducers.

Using this approach, the Lamb wave modes were calculated for the two damage cases being tested: a 99g bonded mass and a fatigue crack. For this research, only the S_0 to A_0 converted mode (A_0/S_0 mode) in signal MC_2 was used as a damage indicator. Figure 8 shows the modes that were determined experimentally. Using Equation (5), the MC_2 mode after damage was determined.

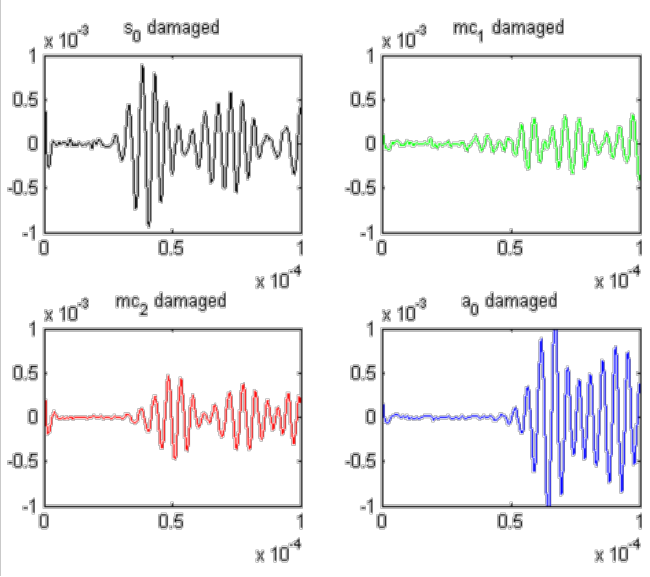

Figure 8: Experimental determination of Lamb wave modes.

2.2.3 Calculation of sensing region

Once the S_0 mode for the healthy case and the S_0 to A_0 converted mode for the damaged case were calculated, the energy of the incident S_0 mode at the damage location as well the mode resulting from S_0 conversion were computed using the experimentally determined attenuation in aluminum. Using this information, the proportion of the S_0 energy that is converted to A_0 can be calculated. Assuming that this energy conversion ratio will remain constant for this type of damage, the maximum distance that a damage mode can travel can be calculated using the following equation:

$$\alpha = -\frac{1}{2R_{AB}} \ln\left(\frac{E_A}{E_B}\right) \tag{6}$$

where E_A and E_B represent the signal energies at any two points A and B, respectively, and R_{AB} is the distance between the two points. Since this critical distance (d_{crit}) is constant, the sensing region around two transducers is an ellipse. Figure 9 shows a schematic of the sensor sensitivity region. When a pair of transducers is spaced farther than d_{crit}, they do not form a sensor-actuator pair as shown in Figure 4(a). The sensing region is elliptical if the spacing is less than d_{crit}, Figure 9 (b), and it becomes more circular as the PZT transducers get closer, Figure 9 (c).

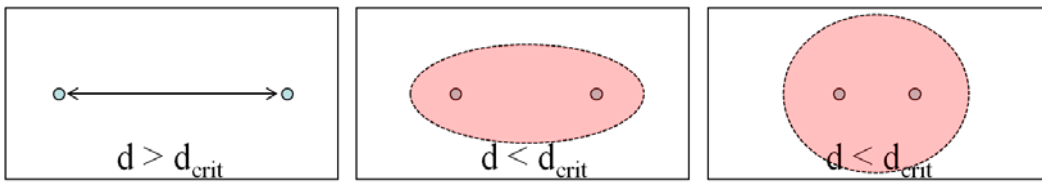

(a) (b) (c)

Figure 9: Sensing region for different transducer spacing.

2.3. Optimization Algorithm

Simulated annealing (SA) has been used for sensor placement optimization. SA is a probabilistic, metaheuristic optimization approach based on the annealing concept in metals where a metal is heated and cooled in a controlled manner to increase the size of the crystals that form and reduce their defects. When the metal is heated, the atoms escape their local minimum energy state. By controlling the rate of cooling the atoms are then able to move around in this higher energy state and find lower energy minima. For the minimization problem addressed in this

work, the SA evaluates nearby solutions at every iteration and replaces the current solution (x^*) with the new solution (x) with a probability (P) that is given by,

$$P = \begin{cases} 1 & , \ if\ x<x^* \\ e^{\left(\frac{x^*-x}{T}\right)} & , \ otherwise \end{cases} \tag{7}$$

where T is the temperature that gradually decreases as the algorithm progresses. From Equation (7), it can be seen that the algorithm will always accept candidate solutions that result in lower function values. However, if all the surrounding x values result in higher function values, the SA can still escape this minimum with a probability that is proportional to the temperature. Initially a large value of T is used to allow the algorithm to explore the function space and not get trapped in local minima. T is reduced after each iteration, thus narrowing the search space of the algorithm. When T=0, the algorithm is limited to only moving 'downhill'.

Figure 10 shows an example of this for a maximization problem. A traditional hill climbing approach would reach a local maximum and then get trapped because all surrounding solutions have a lower function value. The simulated annealing approach, however, can jump randomly, which may lead to the discovery of a better optima in the function space.

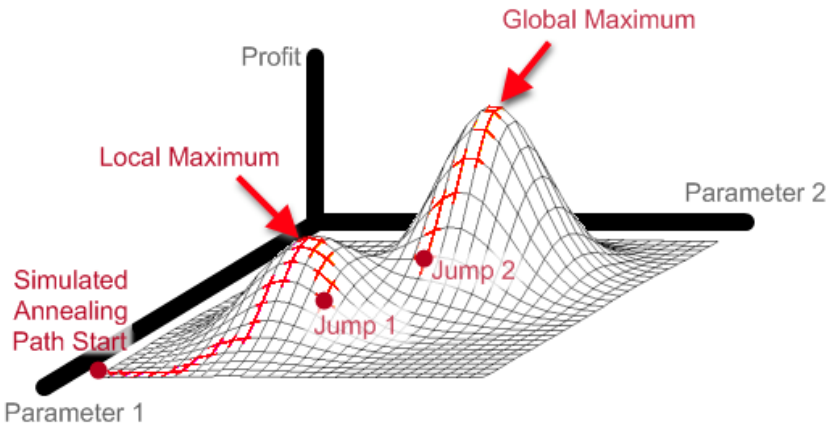

Figure 10: Use of random jumps in simulated annealing to escape local optima and seek global optima.

(http://maxdama.blogspot.com/2008/07/trading-optimization-simulated.html)

In this research, the objective is to have complete sensor coverage of the structure using the minimum number of sensors. To ensure that the result does not have excessive redundancy, a penalty term is introduced in the objective function that penalizes sensors for covering the same space on the structure. The objective function is expressed as follows,

$$Y = w_1(A_{\text{no coverage}}) + w_1(A_{\text{excessive coverage}}) - w_3(A_{\text{good coverage}}) + w_4(N_{\text{transducers}}) + w_5(\sigma_{\text{transducer location}}) \quad (8)$$

where A_x is the area of the plate subjected to sensor coverage condition x, w_i are user defined weight factors that can be used to specify the relative importance of the different terms in the equation, and $N_{transducers}$ is the number of

actuator/sensors being placed on the structure. $\sigma_{\text{transducer location}}$ is normalized stress at the transducer location.

2.4. Results and Discussion

Two different test articles were used to investigate the efficiency of the sensor placement approach. The first is a Navy SHM test bed provided (Figure 11). It consists of two 36”x36” plates bolted together using a doubler and several bolts. Each plate has different diameter holes in them with surrounding bolt holes for added complexity. The top and bottom 3” sections of the plate were reserved for clamping and sensors could not be placed in that region. However, it is important that these regions be covered by the sensing region since damage could initiate due to the boundary conditions. The same applies to the joint at the center of the structure where the two plates are bolted to each other using a doubler.

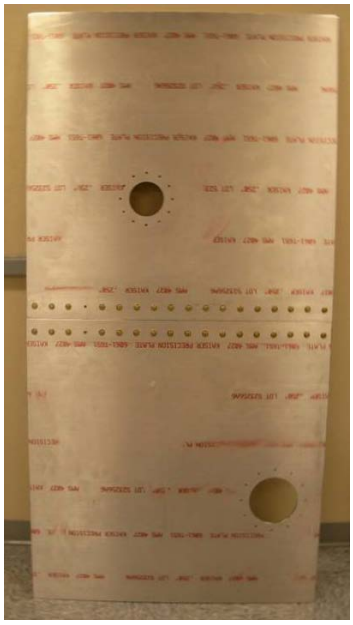

Figure 11: Navy SHM test bed.

Figure 12(a) shows the initial random configuration of the transducers before optimization. The right of the figure shows the regions where sensors cannot be placed but where damage could still occur (red), and the location of the holes. The left part shows a discretized version of the same structure. Each grid point represents a location that was checked to see if it was covered by a sensor-actuator pair. Blue indicates regions that were not covered by any sensors, green regions have excessive sensor coverage and black regions are covered by 1-2 transducer pairs. The value of d_{crit} that was calculated for the added mass type damage was about 26". Figure 12(b) shows the output of the algorithm and the final placement of all the transducers. For this structure, the loading and boundary conditions were not known so a uniform stress distribution/probability of damage was assumed. Initially, 20 sensors were placed on the structure, but the optimization results indicate that only 11 sensors are required to provide complete coverage to this structure.

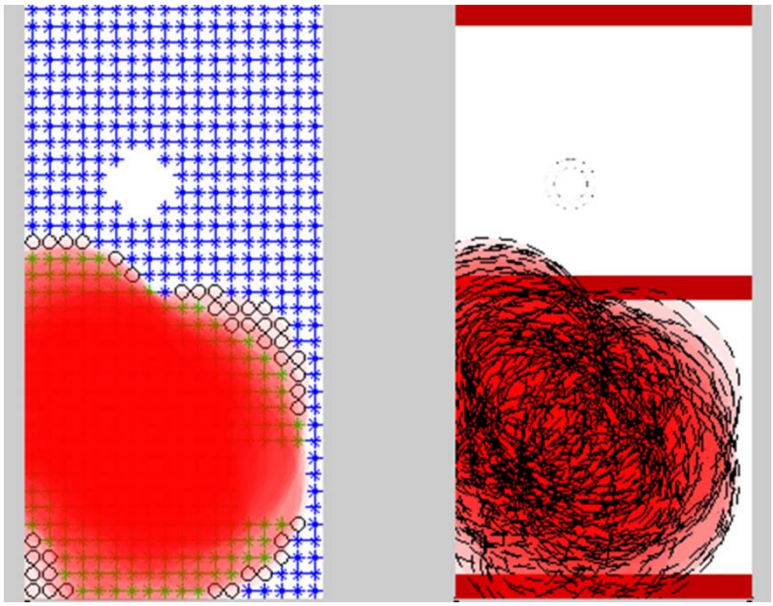

(a)

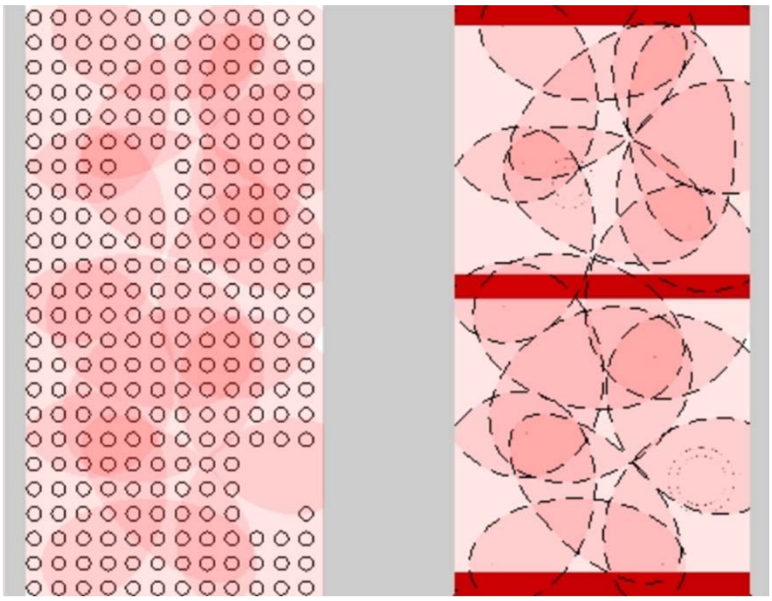

(b)

Figure 12: Initial (a) and final (b) configuration of sensors after optimization.

The second test article is an aluminum lug joint, Figure 13, for which d_{crit} was estimated to be about 6” in the case of crack damage.

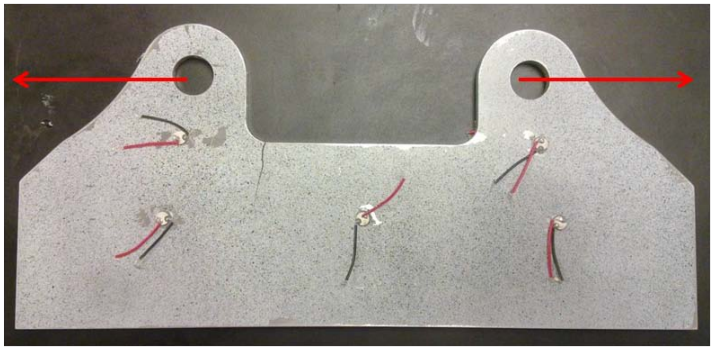

Figure 13: Lug joint specimen with fatigue crack.

The predominant failure mode of the lug joint is through fatigue loading applied at the pin holes, in the direction of the red arrows (Figure 13). Since the loading

for this specimen is known, a finite element analysis (FEA) was carried out to determine the regions of high stress where damage is most likely to occur. Through the optimization procedure, the goal is to not place sensors in these areas but still detect the initiation of damage at these locations with high fidelity. Figure 14 shows the stress distribution in the lug joint. It can be seen from the figure that the most likely location for a fatigue crack to initiate and propagate is at the shoulder of the joint where the stress is highest. In order to utilize this information in the optimization procedure, the stress distribution was converted into a grayscale image where darker regions had higher stress. This image was then converted into a matrix of luminosity values, which were normalized and then used to provide a measure of relative stress at different points of the structure.

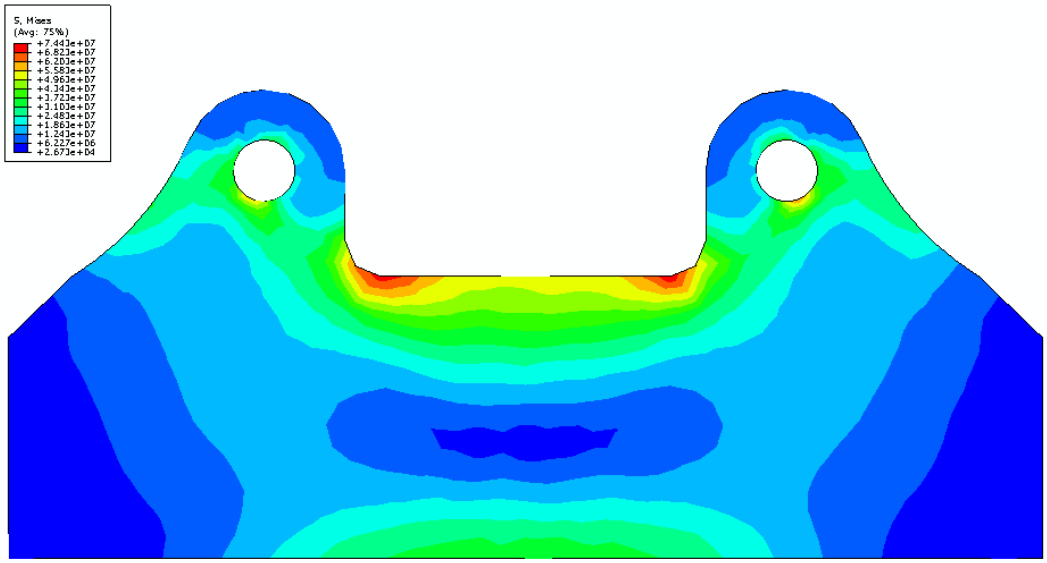

Figure 14: Stress distribution in lug joint

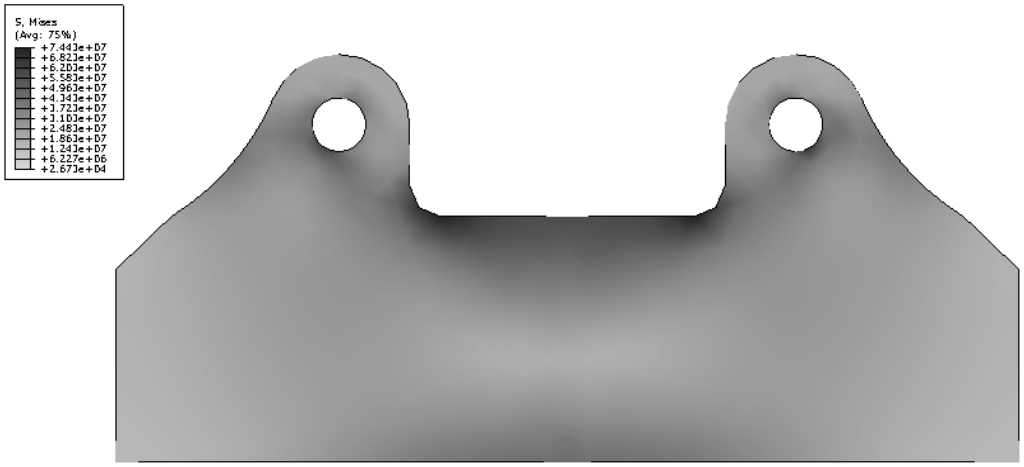

Figure 15: Grayscale stress distribution

Figure 16(a) shows the initial placement of the sensors before optimization. The region covered by each pair of transducers is also indicated. The pin holes of the joint were not discretized since in practice there is a clevis connector that is used when the structure is setup for fatigue testing. This means that sensors cannot be placed in this region. Figure 16(b) shows the result of the optimization reducing the number of transducers from 10 to 6 while maintaining maximum coverage at a user defined probability of false alarm.

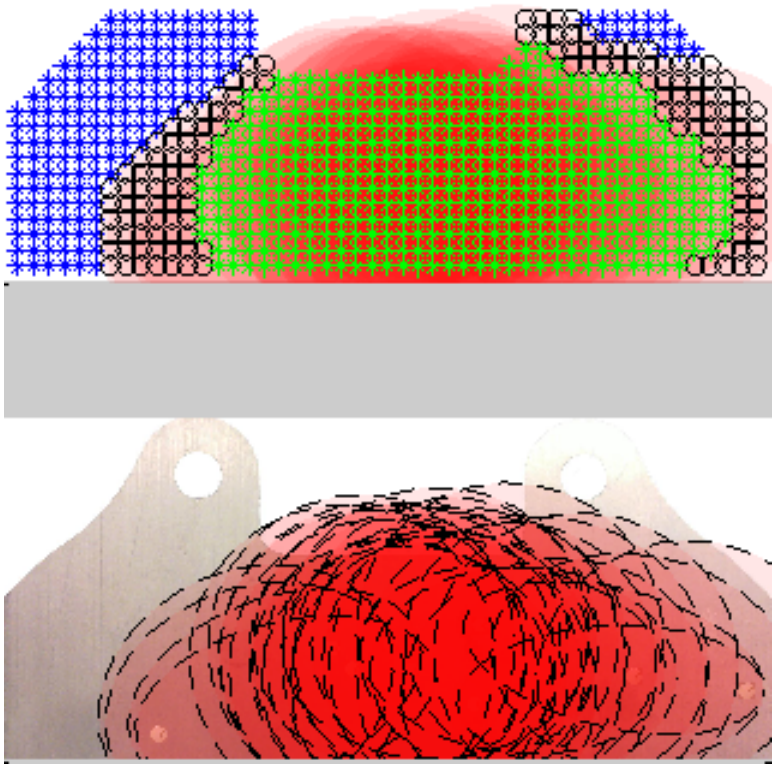

(a)

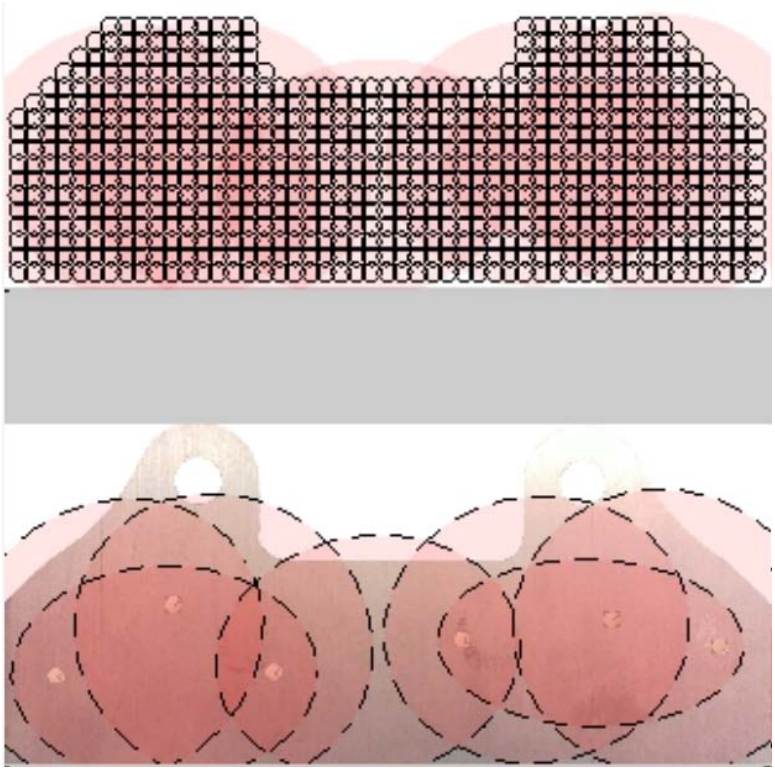

(b)

Figure 16: Initial (a) and final (b) placement of sensors for crack detection on a lug joint

Chapter 3

DAMAGE DETECTION

The principle objective of structural health monitoring is to be able to detect the presence of defects close to the nucleation stage so that steps can be taken to avoid system or sub-system level failure. In a structure, it is well known that the dominant sites for crack nucleation and growth occur at joints because of stress concentrations created by varied geometry and part interfaces. For bolted joints in particular, a loss of torque in one or more bolts can dramatically reduce the fatigue life [52-54] of the part. The role of torque in a bolted joint is to provide a clamping load that increases the friction between the areas of the lap that are in contact, preventing slip during loading. In this way, the applied load is transferred directly from one lap to another through friction. When a bolt becomes loose, there is a stress concentration at the interface between the bolt shank and the edges of the hole due to load transmission through the bolt and plate hole, causing fretting. The motivation of this chapter is to investigate fatigue damage in bolted joints caused by torque loss.

This chapter presents a kernel based method to diagnose structural defects and presents some examples for damage detection in bolted joints. An anomaly detection tool is developed using one-class Support Vector Machines (SVMs) that utilize only the nominal state of the system while looking for different fault modes that might occur during its operation. The fundamental idea behind the

kernel based method is to use a function Θ to map a given dataset, $x \in X$, into the Hilbert space. The transformed features are then manipulated to perform a specific task. Here the objective is to separate different defect signatures (patterns). Specifically, Radial Basis Function (RBF) has been used to do the mapping. The one-class SVMs, an unsupervised technique used in this study identifies outliers in the test dataset and characterizes anomalous behaviors in wave based sensor signatures.

3.1. Time Delay Embedding

The sensor response collected from a piezoelectric sensor is a time series, which can be defined as a sequence of measurements $x(t)$ at different instances of time of an observable x acquired at regular time intervals. In time series applications, the dynamical information of the system can be extracted for a given data set of scalar observations where each of these observations correspond to the projection of the systems' state vector in one dimension. Taken's theorem [55] states that it is possible to reconstruct the attractor in the phase space given $x(t)$. This can be achieved using the time embedding approach where a one-to-one differential mapping between a finite windowed time series can be constructed. Given a time series $x(t)$ with N number of data points, the state space vectors can be represented as follows,

$$y(t) = \begin{bmatrix} x(t) \\ x(t+\tau) \\ x(t+2\tau) \\ . \\ . \\ . \\ x(t+(D_E-1)\tau) \end{bmatrix} \tag{9}$$

where the time instant $t = nT_s$, T_s being the sampling time. The parameter D_E is the embedding dimension and τ is the time delay. Delay reconstruction makes it possible to view the dynamics in terms of the scalar field. The best surface fitting these points represent the approximate dynamics of the system. Figure 17 shows a three dimensional phase portrait generated using sensor signals from a bolted joint structure. This type of visualization makes it easier to identify changes in the signals that are manifest through the introduction of damage.

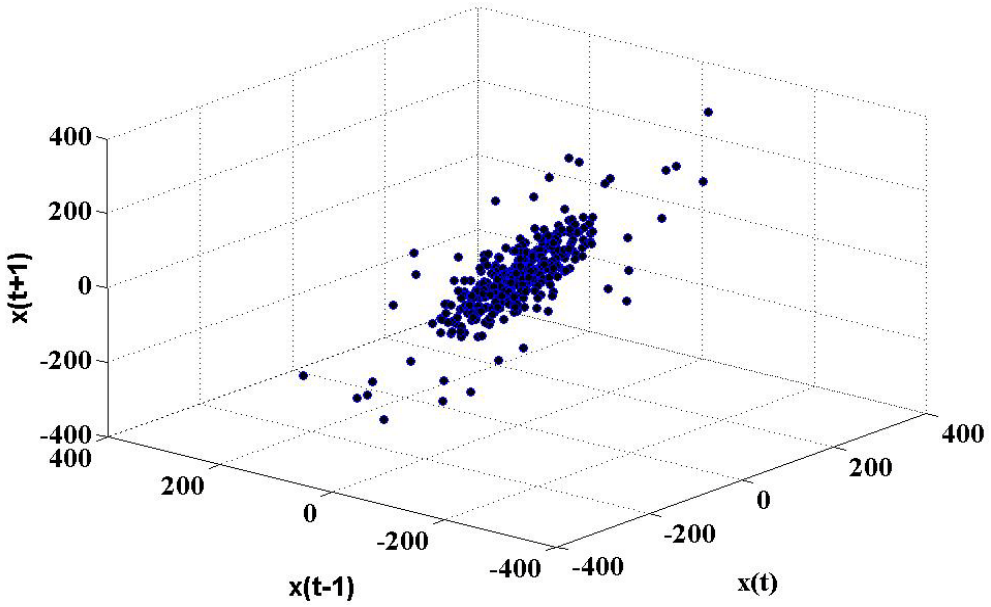

Figure 17: Three dimensional delayed reconstruction of sensor signal from bolted joint (100% torque, 0 cycles)

The time embedding approach is a very popular technique in the field of nonlinear dynamics and is commonly used to predict the future dynamics of a system. To ensure proper reconstruction, the embedding dimension and the time delay have to be assigned properly. In data driven approaches, while introducing delay in experimental data sets, the choice of the time delay is considered to be a very important step. This is because when τ is chosen to be very small compared to the internal time scale of the system, the successive components of the delay vectors $x(t)$ and $x(t+\tau)$ are almost linearly dependent, that is, they are highly correlated. On the other hand, a very large delay τ, can result in an "over-folding" of the attractor. A practical way to choose the proper τ is to assign an interval $0 < \tau < 0.5T_{fm}$, where T_{fm} is the reciprocal of the dominant frequency present in

the spectrum. In the present work, D_E has been taken as 11 and τ as the interval between two consecutive sample points. This means that each measurements *x(t)* would lead to 11 dimensional input vectors. Figure 18 represents the closeness of the phase portrait in 2D for three different measurements taken by a sensor from a bolted joint at the same damaged state (100% torque at 0 kcycles). Figure 19 shows how the phase portrait differs when the dynamics of the system changes under different torque conditions (100%/60%/30% cases).

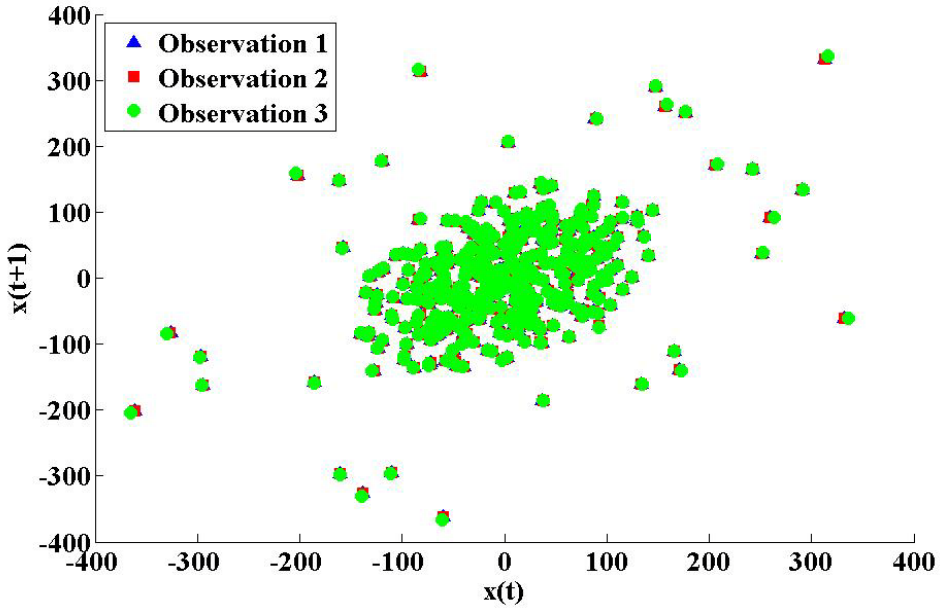

Figure 18: Phase portrait *x(t)* vs *x(t+1)* for 3 measurements without change in damage state.

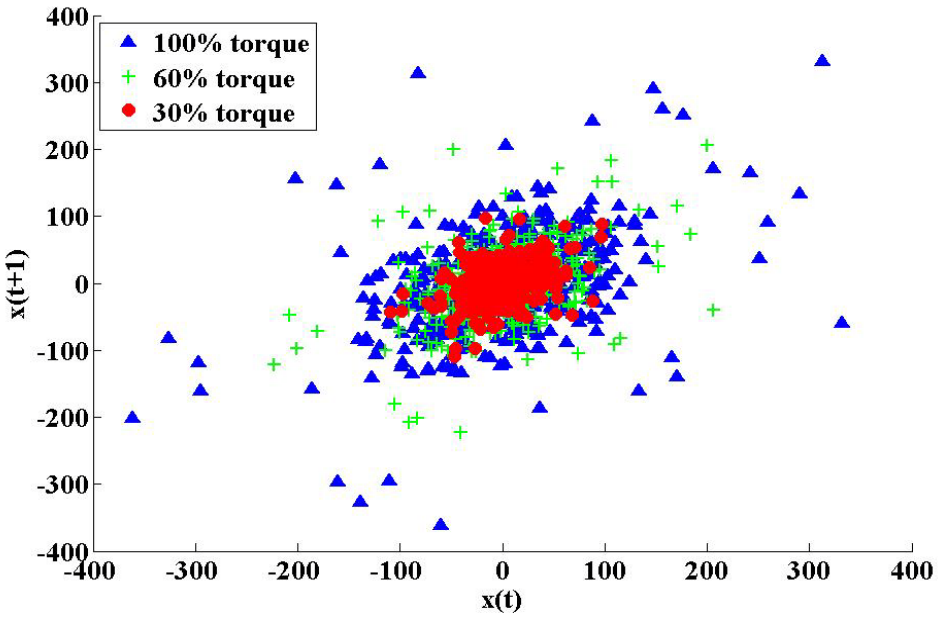

Figure 19: Phase portrait *x(t)* vs *x(t+1)* for 3 measurements made at different damage states

3.2. One Class Support Vector Machines

SVM is a machine learning technique that maps the extracted feature vector of input space to high dimensional domain known as feature space and, thereafter constructs an optimal hyperplane to separate the features by solving a quadratic optimization problem. Often, in the real world, patterns are nonlinearly separable in input space. The idea is to map the n- dimensional vectors of the input space into a high-dimensional (possibly infinite dimensional) feature space (Figure 20) where the transformed image of the input patterns are linearly separable. This can be achieved using Cover's theorem, which states that a multidimensional input space can be transformed to a feature space where the transformed image of the

input patterns are linearly separable provided the transformation is nonlinear and the dimensionality of the feature space is high enough.

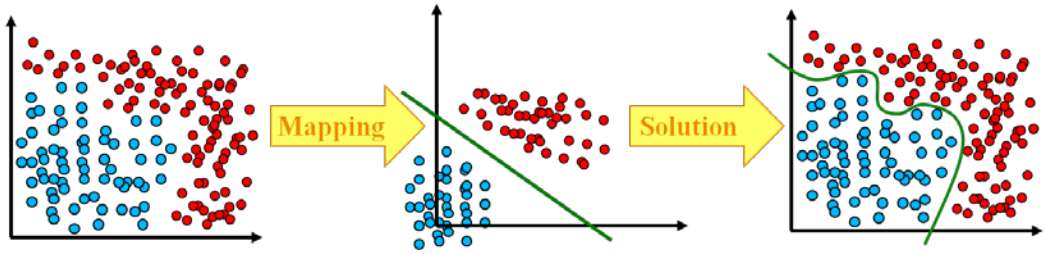

Figure 20: Finding complex separatrix through high dimensional mapping.

The high dimensionality of the feature space enables the construction of a linear separating hyperplane in the space. However numerical optimization schemes in high dimension would suffer from the problems associated with dimensionality. Such computational complexities can be avoided by taking advantage of the inner–product kernel where the dot product in the feature map is implicitly computed by evaluating the simple kernel, thus avoiding the explicit calculation of the feature map. In the present study, the input data is mapped into an infinite-dimensional feature space using a Radial Basis Function (RBF) kernel and can be expressed as,

$$K\left(\vec{x}, \vec{x}_i\right) = \exp\left(-\frac{1}{2\sigma^2}\left\|\vec{x} - \vec{x}_i\right\|^2\right) \tag{10}$$

where the two vectors correspond to the input vector $\vec{x}$ and the i^{th} input pattern $\vec{x}_i$. RBFs [56] are popular for interpolating scattered data as the associated

system of linear equations is guaranteed to be invertible under very mild conditions on the locations of the data points. For example, the thin-plate spline only requires that the points are not co-linear while the Gaussian and multiquadric place no restrictions on the locations of the points. In particular, RBFs do not require that the data lie on any sort of regular grid. Once the data is mapped to the N dimensional space, an N-1 dimensional hyperplane is constructed, which maximizes the separation of the data from the origin taking into account the nonlinear relationship of the data and treats the origin as belonging to the second class. Traditional methods utilize a structure risk minimization method to minimize the empirical training error [56]. The method employed here maximizes the separation of the data from the origin, thus maximizing the observable difference between the training set and data that belongs to a different class. The classifier uses the outliers as representatives of data that have not been observed in the training set. This optimization problem is aimed at finding the optimal set of hyperplane parameters for which the margin of separation between the origin and the support vectors are maximized. This is same as minimizing the Euclidean norm of the weight vector ($\vec{w}$). For non-separable patterns, the primal problem can be formulated as follows.

$$\min_{w,\rho,\xi,b} \frac{1}{lv}\sum_{i=1}^{l}\xi_i - \rho + \frac{1}{2}\langle w, w\rangle \tag{11}$$

subject to $\langle w, \Theta(x)\rangle \geq \rho - \xi_i, \xi_i \geq 0$ $\langle w, \Theta(x)\rangle \geq \rho - \xi_i, \xi_i \geq 0,$ for $v \in [0,1]$,

where Θ is the feature map, ρ is the separation of the hyperplane from the origin,

v is the training error limit, and ξ is the non-zero slack variable. Formulation of the dual problem (Equation (15)) is achieved by first constructing the Lagrangian function, which is expressed as:

$$J\left(\vec{x},\rho,\alpha\right)=\frac{1}{2}\vec{w}^{T}\vec{w}-\sum_{i=1}^{N}\alpha_i\left[y_i\left(\vec{w}^{T}\vec{x}_i+\rho\right)-1\right] \tag{12}$$

The two optimality conditions are:

$$\frac{\partial J\left(\vec{w},\rho,\alpha\right)}{\partial w}=0 \tag{13}$$

$$\frac{\partial J\left(\vec{w},\rho,\alpha\right)}{\partial \rho}=0 \tag{14}$$

Using the Kuhn-Tucker conditions of optimality[57] on the Lagrangian function, with some simple manipulation, it is possible to construct the dual problem which is expressed as

$$\min_{\alpha}\frac{1}{2}\sum\nolimits_{i,j}\alpha_i\alpha_j K(x_i,x_j) \tag{15}$$

subject to, $0\le\alpha_i\le\frac{1}{lv},\sum\alpha_i=1$, where α_i is the Lagrange multiplier. The offset parameter (ρ) can be recovered for all values of α_i. Once this optimization problem is solved, all the parameters necessary to construct the optimal hyperplane are known. Mathematically, features with non-zero Lagrangian

multipliers ($\alpha_i \geq 0$) are termed as support vectors. Once $\Theta(x)$ and α_i are available, the offset can be calculated from the following relation.

$$\rho = \sum_i \alpha_i K(x_i, x_j) \tag{16}$$

Although all the points in Θ are separable, it may not be computationally effective to compute the canonical hyperplanes for data sets that are not linearly separable; therefore an allowable training error ν is introduced [58]. Even though this results in a hyperplane that is not canonical, it rapidly yields acceptable solutions. In this study, an allowable error of 10 percent was used as the maximum allowed, which means that a 90 percent classification rate must be achieved when constructing the hyperplane using the training data. This parameter allows the user to make a trade-off between model complexity and training error. The main advantage of the one-class SVM becomes apparent while training the algorithm because only one class of data belonging to any arbitrary reference can be used [30]. Since there is often no data pertaining to the healthy state of an existing structure, an algorithm must not be greatly affected by a change in the training data. To achieve the optimum classification rate, the algorithm minimizes the upper bound of the generalization error by maximizing the separations of the most similar patterns or support vectors in hyperspace. As a consequence, the margin between the data and the separating hyperplane is also maximized. During classification if the test data points are sufficiently different from the training data, they are placed near the origin on the opposite side of the decision plane. This represents a change in the state of the system most likely due to structural or

sensor damage. To determine on which side of the hyperplane a particular point belongs, a decision function is used to test each new data point. The decision function for a given test vector *Θ(z)* is expressed in terms of the RBF kernel by the following function:

$$F(z) = sign\left(\sum_{i=1}^{l} \alpha_i K(x_i, x_j) - \rho \right) \tag{17}$$

where *F(z)* is the decision function that decides whether a training point should lie on the same side of the hyperplane as the training data or near the origin if it is from a different class. A data point that is from the same class is assigned a value of +1 and data that is not from the same class is assigned a value of -1 (Figure 21).

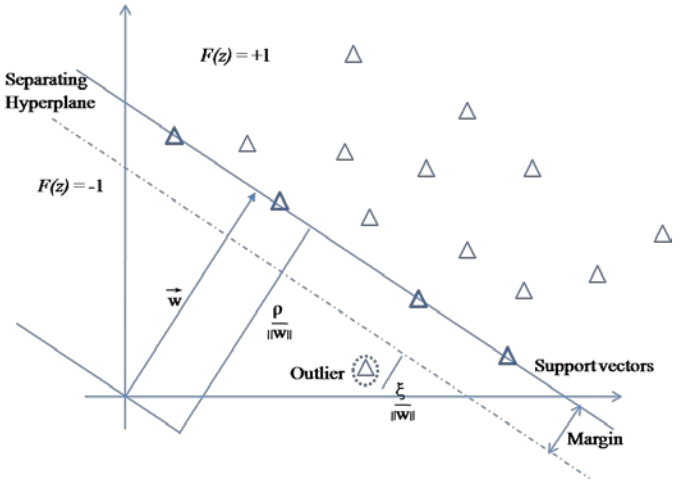

Figure 21: Graphical representation of hyperplane construction.

In order to design the SVM classifier, it is necessary to select an appropriate kernel parameter for each class of data. The parameter controls the smoothness of

the kernel function and is tuned based on the model parameter, such that the upper bound on the classification error is satisfied. The parameter σ acts as an in-built tuning parameter that controls the quality of the training. The kernel width has a regularization effect on the cost function, which is minimized during training in order to achieve the upper bound of the allowable error *v* [59]. Since choice of this parameter is application specific, it is important to calculate an optimum value for a given training set. A simple brute force method is adopted to do this [60]. First, α_i and ρ are calculated for a range of kernel parameters and the data is classified using these parameters. The optimal σ is selected as the smallest kernel parameter that reduces the misclassified data to *v* percent of the training data. A graphical representation of this selection is shown in Figure 22.

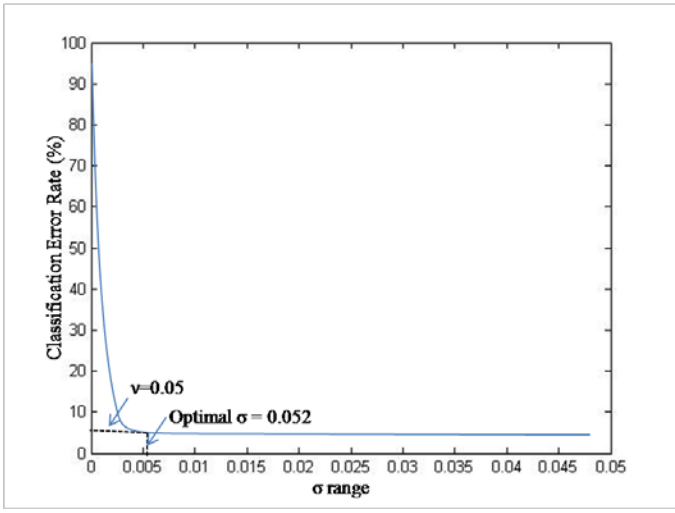

Figure 22: Demonstration of optimal σ selection

3.3. Experimental Setup

The test specimens used for testing were machined out of an Al 6061-T651 plate, 1/8” thick. The dimensions of the laps were chosen so that they were representative of commonly used joints in aerospace structures. Since the location of the notch was known before testing, sensors were only mounted on the center lap. The single lap bolted joint was instrumented with 0.25 in diameter, 0.01 in thick, APC 850 pzts in an optimized arrangement. The fatigue loading of the bolted joint was carried out on an Instron 1331, 22 kip capacity servo hydraulic load frame. The joint was subjected to a 2 kip max load (R=0.1) at 20Hz. To speed up the testing, one bolt was left completely loose while the other bolts were tightened to 100 in-lb of torque. Figure 23 shows the setup that was used.

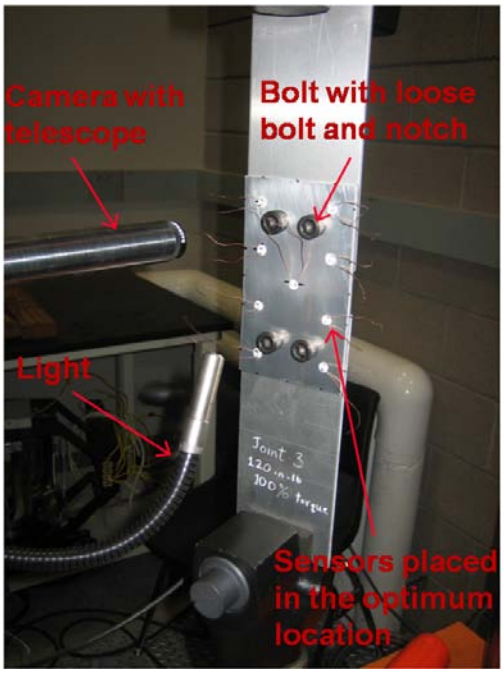

Figure 23: Experimental setup used when testing bolted joints.

In order to know the exact initiation site for the crack, the bolt hole with the loosened bolt was notched using an Electrical Discharge Machining wire. The fatigue test was paused frequently during the test to take PZT measurements and pictures of the damage. Pictures were taken using a camera attached to an optical camera focused on the notch. In order to improve the picture quality and make it easier to distinguish surface scratches from a growing crack, only the viewing surface was polished using 1200 grit paper. The rest of the contact surfaces were untouched so that the fatigue behavior of the structure was not significantly altered. The bolted joint was left on the frame when data was collected to ensure uniform boundary conditions for all the readings. The level of torque in the loosened bolt was also adjusted to 30, 60, and 100 percent to show the effect of torque on the observed signal at a given crack length. A 130 kHz, Gaussian windowed sine wave was used as the excitation signal. The acquisition was carried out at a rate of 2 MSa/s with 100 observations taken for each sensor.

Before the test specimen could be instrumented with detection hardware, it is necessary to determine the wave attenuation in the aluminum media. By understanding the extent of the attenuation in the material, distance between sensors placed on the structure can be determined so that there is sufficient overlap of the sensing regions in the structure. An optimal sensor placement technique [11] is used to determine the placement of the sensors on the structure. The optimization was constrained so that sensors were not placed too close to the edges or the bolts. The resulting sensor placements are shown in Figure 24. Before the placement of the sensors could be determined, it was necessary to

decide the minimum size of crack that could be detected so that a threshold voltage corresponding to that minimum crack size could be ascertained and any signal with a lower voltage could be ignored as noise.

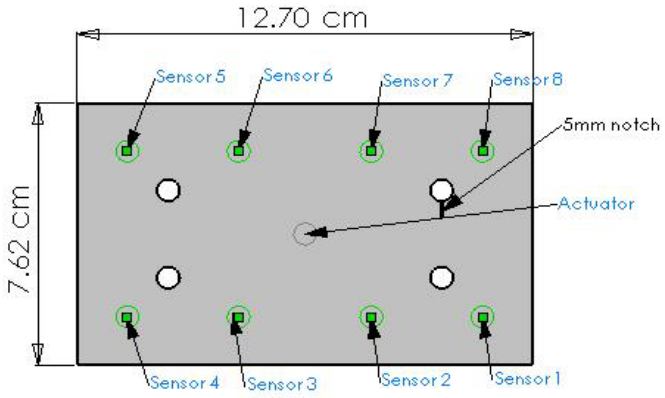

Figure 24: Sensor placement used for data collection on bolted joint.

3.4. Signal Conditioning

Since the data for the bolted joint specimen was collected while it was still mounted on the servo hydraulic frame, the acquired signal had some parasitic parameters that had to be removed before classification. These parameters included broadband noise, a low frequency wiggle since the sample was still mounted on the frame, non-uniform signal energy, and DC clamping. In order to remove these parameters, the data was first processed using band pass filter, allowing frequencies between 10-300 kHz to remove the low frequency wiggle, noise, and DC clamping. The signals were then normalized and down sampled to make the signal processing faster. A matching pursuit decomposition using 60 iterations was used to decompose the signal and then reconstruct it to make the input signal smoother for classification.

3.5. Results and Discussion

Figure 25 shows the length of the crack measured using the optical telescope as a function of the number of cycles. The data collected at different number of load cycles and different torques from the different sensors were combined and used to train the SVM algorithm so that it could identify changes on a system level and not be susceptible to changes local to each sensor. This approach also reduces the computational expense of running several different combinations of data sets. To simulate a more realistic scenario, the system was trained with data from the 100% torque, 0 kcycles case, representing a new structure. The trained algorithm was then tested using data from every other data collection point.

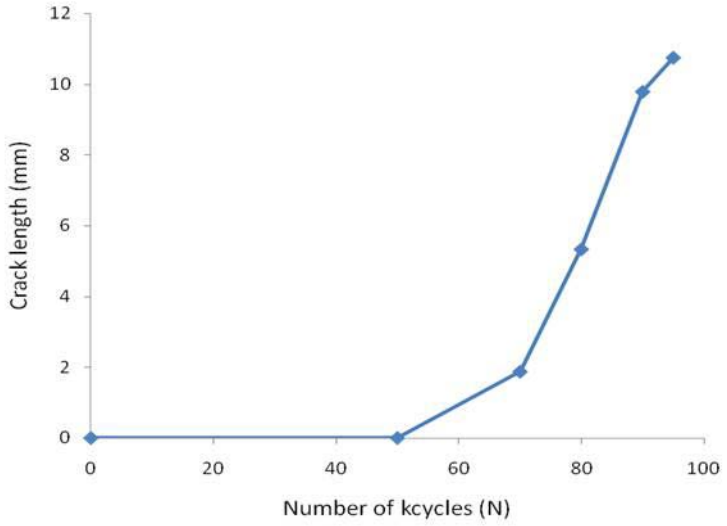

Figure 25: Crack length as a function of number of cycles

Every time the fatigue test was stopped, data was collected from the sensors and combined in such a manner that the algorithm was trained with all the features of

this state. Figure 22 shows the classification error rate as a function of the number of cycles, which corresponds to the increase in crack length. The classification error rate is plotted instead of the classification rate to provide a measure of the anomalous data caused by the presence of damage.

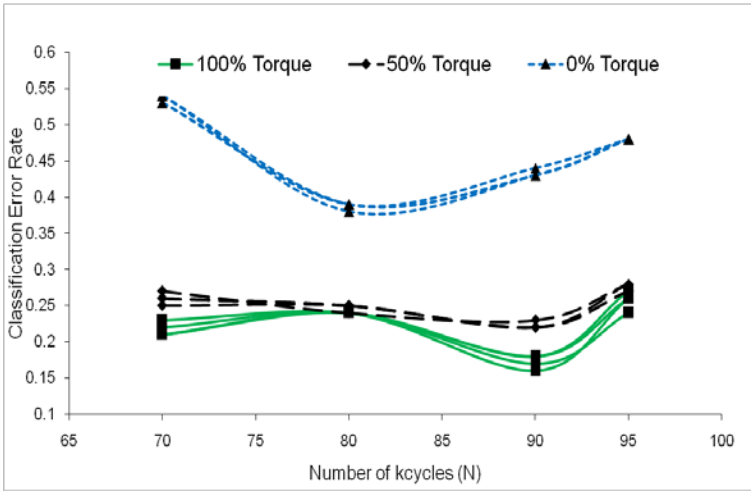

Figure 26: Classification Error Rate (1 - Classification rate) variation with number of cycles, trained with 0 kcycles and 100% torque.

Since a three-dimensional crack that may not be straight through the thickness is generated in the single lap joint, there are a number of possibilities that could contribute to the trends shown in Figure 26. Subjecting a sample to a compressive load caused by torque, causes attenuation of the signal when it reaches the bolt, reducing the small change in the features of the wave. Due to the nature of the load applied, there might be crack closure due to compression reducing the change in the output signal that would be caused by a fully open crack. This makes the wave more likely to be classified as a 'healthy' or nominal data point. When a crack grows out of this compressive region near the bolt, it becomes

easier to identify, resulting in an increase in the percentage of (1-CR). In the case of a completely loose bolt, some of the load gets redistributed to the nearby bolt. It is possible that since the crack length at 80 kcycles was more than half way to the other bolt, it entered the enlarged area of compressive stress around the neighboring bolt.

Figures 27(a) and (b) show displacement fields of the surface of the top lap at 100% torque with 0% torque as the baseline state using an ARAMIS 3D image correlation device. In this figure, the crack originated from the right bolt hole and travelled towards the left bolt. The displacement field plotted shows out-of-plane curvature caused by the application of torque. The apparent buckling of the joint suggests that the crack will be open on the top surface but will be closed on the back surface. There is also a possibility that the buckling changes the load transfer between the laps, in turn changing the stress state around the crack. The exact order or combinations of the aforementioned phenomena that cause the trends shown are not yet fully understood.

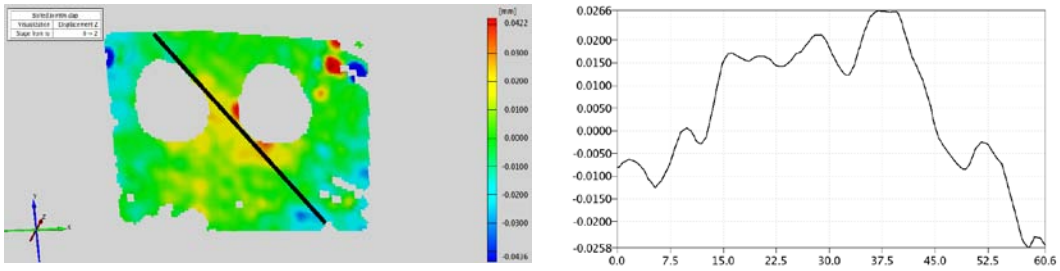

(a) (b)

Figure 27: (a) Displacement field in the z direction, perpendicular to the lap. (b) Relative z variation along the black line in (a).

It is not always possible to obtain healthy state readings for an existing structure, so it is necessary to study the effect of using the current state of a system to see if similar trends in the classification rate are observed. The algorithm was trained using data from 70 kcycles at 100% torque. The results in Figure 28 show that a similar trend is observed.

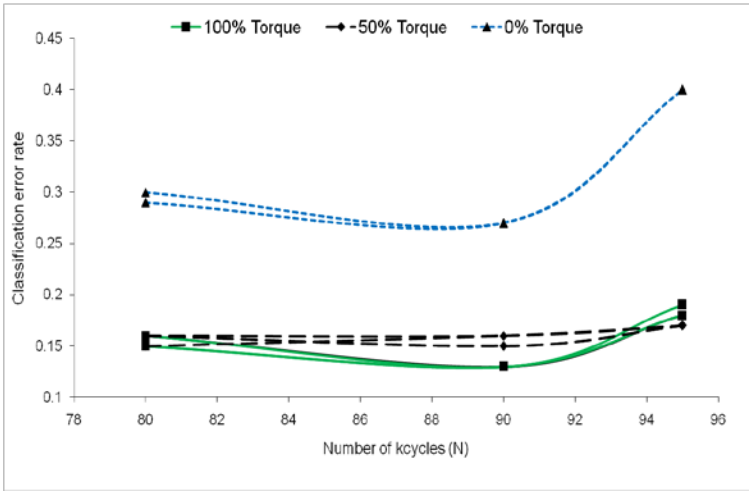

Figure 28: Classification error rate variation with number of cycles, trained with 70 kcycles and 100% torque.

From Figure 26 and Figure 28, it can be seen that there is a large difference in classification error rate between the 0% torque case and the other torque cases. To study the ability of the algorithm to differentiate between the different cases at 50% and 100% torque, the SVM algorithm was trained with every combination of torque and crack length and then tested with every other combination of torque level and crack length. Table 2 shows the different training and testing classes that were used for this analysis.

Table 2: Classes of observations used to study differences in classification rate between 50% and 100% torque.

Data description (fatigue cycles)	Class (*C*)	Torque level	Training/Testing Classes	Total observations
70Kcycs	1	50%	TRC1	40
80Kcycs	2	50%	TRC2	40
90Kcycs	3	50%	TRC3	40
95Kcycs	4	50%	TRC4	40
70Kcycs	5	100%	TRC5	40
80Kcycs	6	100%	TRC6	40
90Kcycs	7	100%	TRC7	40
95Kcycs	8	100%	TRC8	40

Let *A* and *B* represent 2 classes of signals that may or may not be distinct (Figure 29). If we train the algorithm with *A* and test with *B,* it will yield a classification rate *X*. Similarly, training with *B* and testing with *A* yields a classification rate *Y*. If the absolute value of the difference between *X* and *Y* is less than a defined threshold, then the two signals *A* and *B* belong to the same class, and this has been used as a selection criteria. In the present analysis, this difference is taken to be less than five percent of the required classification rate (1-ν). Geometrically, the selection criteria means that the hyperplane constructed for the first case is very similar to the hyperplane constructed in the second case in that most of the data lies on the same side for both cases. In this study, R_{ij} is the number of observations classified as being in the same class in Q_{ij} divided by the total

number of observation combinations. Table 2 shows the results of this analysis. Since there are eight training classes and eight testing classes, there are 64 combinations but only 32 independent results.

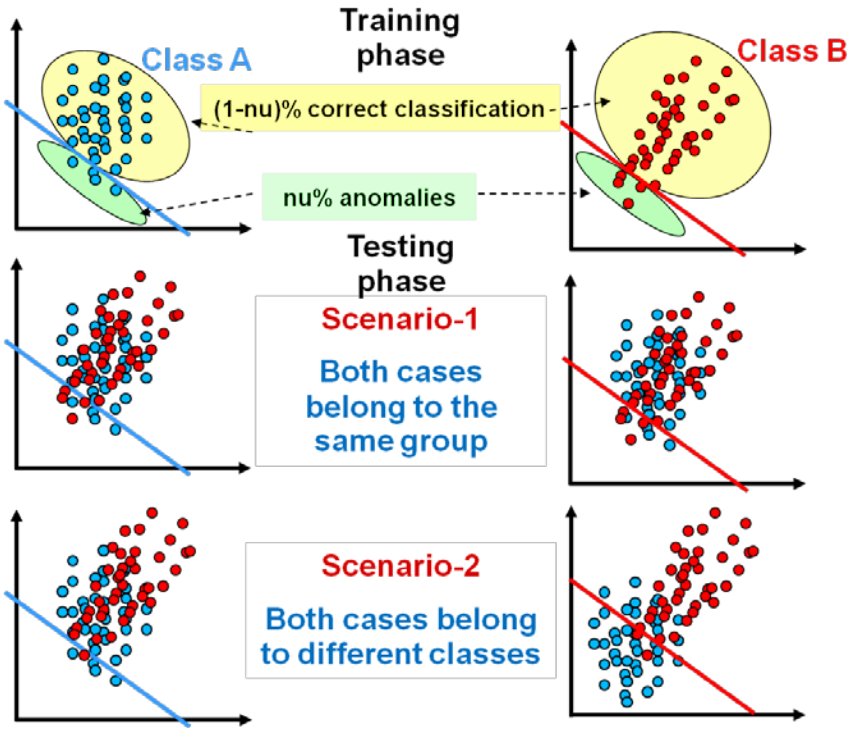

Figure 29: Distinguishing two classes using one-class SVM

Table 3: Classification rate (matrix) for sensor set 1,2,7,8.

S_{ij} ν =0.1 σ		TRC1 (test)	TRC2 (test)	TRC3 (test))	TRC4 (test)	TRC5 (test)	TRC6 (test)	TRC7 (test))	TRC8 (test)
0.08	TRC1 (train)	0.9	0.86	0.75	0.76	0.83	0.85	0.82	0.77
0.065	TRC2 (train)	0.86	0.9	0.77	0.73	0.83	0.85	0.83	0.75
0.085	TRC3 (train)	0.95	0.92	0.9	0.9	0.96	0.95	0.93	0.89
0.075	TRC4 (train)	0.94	0.92	0.86	0.9	0.93	0.93	0.93	0.87
0.07	TRC5 (train)	0.89	0.87	0.8	0.77	0.9	0.87	0.84	0.78
0.065	TRC6 (train)	0.9	0.88	0.79	0.78	0.86	0.9	0.84	0.78
0.075	TRC7 (train)	0.91	0.88	0.8	0.78	0.87	0.88	0.9	0.8
0.075	TRC8 (train)	0.95	0.91	0.87	0.86	0.93	0.94	0.93	0.9

From Table 3, it can be seen that in many cases, S_{ij} is very close to S_{ji}. A selection criteria is defined as follows,

If $\left\|S_{ij} - S_{ji}\right\| \le 0.05(1-\nu)$, $\quad Q_{ij} = Q_{ji} = 1$

Else $\qquad Q_{ij} = Q_{ji} = 0$.

Using this selection criterion, the Q_{ij} matrix is computed and presented in Table 4. Out of the 32 cases that were tested, the algorithm was able to correctly predict 23 cases, resulting in a success rate of 72%.

Table 4: Outcome of the classifier.

Q_{ij}	TRC1 (test)	TRC2 (test)	TRC3 (test))	TRC4 (test)	TRC5 (test)	TRC6 (test)	TRC7 (test))	TRC8 (test)
TRC1 (train)	1	1	0	0	0	0	0	0
TRC2 (train)	1	1	0	0	1	1	0	0
TRC3 (train)	0	0	1	1	0	0	0	1
TRC4 (train)	0	0	1	1	0	0	0	1
TRC5 (train)	0	1	0	0	1	1	1	0
TRC6 (train)	0	1	0	0	1	1	1	0
TRC7 (train)	0	0	0	0	1	1	1	0
TRC8 (train)	0	0	1	1	0	0	0	1

Chapter 4

DAMAGE CLASSIFICATION

Damage classification is an important aspect of structural health monitoring because it gives the user an indication of the type and extent of the damage induced in the structure. Knowledge of the type of damage in the structure also aides in the prediction of damage growth since different damage types grow at different rates when subject to the same loading. This chapter presents a methodology for data mining of sensor signals for damage classification using SVMs.

A hierarchical decision tree structure was constructed for damage classification, and experiments were conducted on metallic and composite test specimens with surface mounted piezoelectric transducers. Damage was induced in the specimens by fatigue, impact, and tensile loading; in addition, specimens with seeded delaminations were also considered. Data was collected from surface mounted sensors at different severities of induced damage. A Matching Pursuit Decomposition (MPD) algorithm was used as a feature extraction technique to preprocess the sensor data and extract the input vectors used in classification. Using this binary tree framework, the computational intensity of each successive classifier was reduced, increasing the efficiency of the algorithm as a whole. The results obtained using this scheme show that this type of classification architecture works well for large data sets because of a reduced number of

comparisons that are required. Due to the hierarchical setup of the classifiers, performance of the classifier as a whole is heavily dependent on the performance of the classifier at higher levels in the classification tree.

This chapter is organized as follows. Sections 4.1 and 4.2 presents a theoretical background on the method used for classification and its organization as a binary tree classifier. The theory behind the extraction of features used for classification is presented in section 4.3. The experimental setup and some details regarding data collection have been discussed in section 4.4. Section 4.5 demonstrates the effectiveness of the classification scheme through selected results from a fatigued lug joint.

4.1. Support Vector Machines

Support Vector Machines have been used for classification in a number of different fields because of their good generalization[42] capability, i.e., they are able to learn the behavior of the system even with relatively few examples. The ability of SVMs to separate nonlinearly separable data is based on Cover's theorem[61], which states that non-separable or nonlinearly separable patterns in input space (low-dimensional space) are more likely to be linearly separable in a new high-dimensional feature space, provided that the transformation is nonlinear and the dimensionality of the feature space is high enough. The patterns in this high-dimensional (say *N* dimension) space are then separated by constructing an *N-1* dimension hyperplane, which takes into account the nonlinear relationship of the data. The mapping kernel used in this research is the Radial Basis Function

(RBF), which is popular in machine learning applications[35, 62] involving data sets that are not linearly separable. The RBF kernel takes the form of

$$K(x, x_i) = e^{-\frac{\|x - x_i\|}{2\sigma^2}}, \tag{18}$$

where $\boldsymbol{x}$ is the input vector, $\boldsymbol{x_i}$ is the i^{th} input pattern, and σ is the width of the kernel that has been optimized during the training phase. Once the training data has been mapped into high- dimensional space, an optimal hyperplane is constructed. The optimal hyperplane is defined as one which maximizes[61] the separation between the two classes allowing the algorithm to learn the differences in the data sets.

The decision boundary for patterns that are linearly separable is defined as,

$$w \cdot z_i + b = 0, \tag{19}$$

where w is an adjustable weight vector, b is a bias and z_i is the mapped input pattern. For an input point (z_i, y_i), where y_i is the corresponding class label, the above equation is subject to,

$$y_i \left(w \cdot z_i + b \right) \geq 1. \tag{20}$$

This is obtained by rescaling w and b such that two parallel hyperplanes for $y_i = \pm 1$ are obtained. The distance between these two hyperplanes defines the margin of the classifier. In most practical applications, the data is nonlinearly separable, and it is not possible to construct a hyperplane without admissible training errors. In

such a case, a soft margin[63] is imposed, which allows a certain number of data points to be misclassified (Figure 30), and the above equation can be modified as,

$$y_i\left(w\cdot z_i+b\right)\geq 1-\xi_i, \tag{21}$$

where $\xi_i \geq 0 \quad \forall i$, is a slack variable. In order to find this optimal hyperplane that minimizes the classification error, the following optimization problem needs to be solved

$$\min \frac{1}{2}\|w\|^2 + D\sum_i \xi_i, \tag{22}$$

subject to the constraint shown in Equation (21) The variable *D* refers to a regularization parameter that can be modified to control the complexity of the model. A large value of *D* means that the classifier will only classify separable data. For this research, a k-fold cross-validation scheme will be used to optimize the hyperparameters σ and *D*. Defining $w(\alpha)=\sum_i \alpha_i y_i z_i$, the dual problem can be constructed as,

$$\max \mathrm{W}(\alpha)=\sum_i \alpha_i - \frac{1}{2} w(\alpha)\cdot w(\alpha), \tag{23}$$

subject to $0\leq \alpha_i \leq D \quad \forall i$ and $\sum_i \alpha_i y_i = 0$. Solving Equation (23) for the Lagrange Multipliers (α), it is possible to recover the solution to the primal problem. The decision function for the classifier becomes,

$$y(x)=\mathrm{sign}\left\{\sum_i \alpha_i y_i K\left(x, x_i\right)+b\right\}. \tag{24}$$

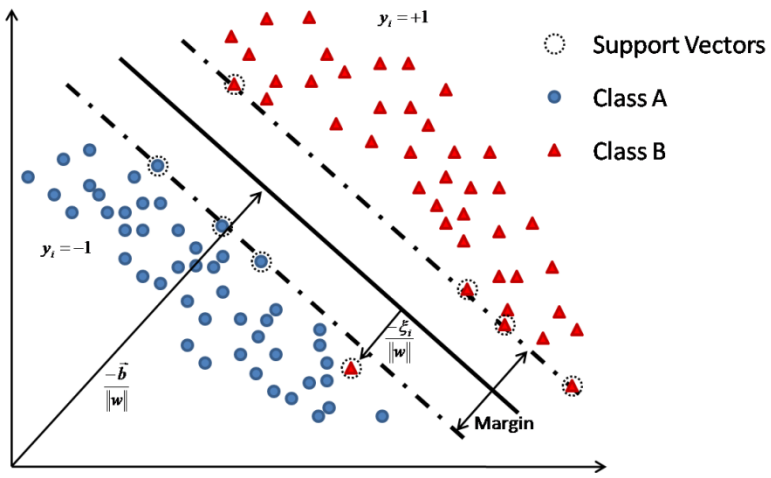

Figure 30: Representation of parameters needed for hyperplane construction in two dimensions.

4.2. SVM as a binary tree classifier

The multi-class classifier used in this paper combines a modified 'one vs rest' algorithm with a binary tree structure[42] to minimize the number of comparisons that are necessary to identify a data class while still taking into account all possible classes. For a four-class problem as shown in Figure 31, the binary tree classifier is setup as follows.

Step 1. A two-class SVM is trained using pattern 1 as Class A and patterns 2, 3, and 4 as Class B, and a hyperplane is constructed.

Step 2. Next, data points corresponding to pattern 1 are removed from the training set and pattern 2 is denoted as Class A and patterns 3 and 4 are denoted as Class B for hyperplane construction.

Step 3. This process is repeated until the last classifier compares the last two patterns.

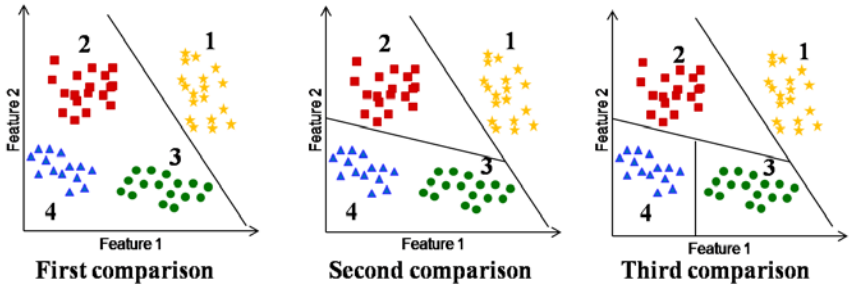

Figure 31: Construction of multiple hyperplanes without overlapping regions for multi-class problems.

The advantage of this approach is that for a *k* class problem, only (*k-1*) hyperplanes need to be constructed. Also, removing patterns after each classifier is constructed reduces the computational expense. In this way, it is also possible to prioritize damage classes and terminate the classification algorithm during testing before checking all possible cases. In this paper, since the damage considered is only of one type, the classifiers are arranged in order of increasing crack length. In a more complex structure like a bolted joint, for example, it would be possible to prioritize torque loss (fault type *A*) over structural damage (fault type *B*), and the algorithm can be terminated midway if a loose bolt is detected[6, 35]. In order to ensure there is no region of overlap where one point could be classified as belonging to multiple classes, a point in the first comparison that is classified as belonging to Class A is removed from the test set, and the points in Class B move on to the next classifier.

4.3. Feature extraction algorithm

Feature extraction is a vital part of any data mining algorithm. The features extracted from the raw data need to be meaningful in the sense that they reflect changes in the system due to different types of damage. In this research, matching pursuit decomposition (MPD) has been used as a feature extraction tool. MPD has been used for various applications such as feature extraction, signal characterization and classification[64], and signal encoding and reconstruction[65]. The working principle of MPD relies on decomposing a given signal into linear expansions of elementary functions (or atoms). The resulting decomposition reveals the waveform's time-frequency structure[51]. A change in the signal is represented by the selection of different atoms that represent the waveform.

In this research, the dictionary elements were composed of Gabor atoms, normalized in both the time and the frequency domain[51]. These atoms were selected since they have energy that is concentrated in the time-frequency domain, and there exists a closed-form[51, 66] analytical time-frequency representation for such atoms. Also, the algorithm is guaranteed to converge if the dictionary used is complete and the atoms have unitary energy[67]. The decomposition of the signal is based on four variables that define each dictionary element: expansion coefficient (C), time shift (τ), frequency shift (f) and atom width (k). The expression for the atoms used is given by

$$g_i(t) = e^{-k_i^2 (t-\tau_i)^2} \cos(2\pi f_i t). \quad (25)$$

Using these atoms, the decomposition after M iterations can be written as,

$$x(t) = \sum_{i=0}^{M-1} C_i g_i + R^M x(t), \tag{26}$$

where $R^M x(t)$ is the residue of the signal after decomposing the signal M times, and $R^0 x(t)$ is the original signal for $M = 0$. As $M \to \infty$, the signal residue will go to zero and the entire signal will be decomposed, that is,

$$\lim_{M\to\infty} \left\| R^M x(t) \right\|_2 = \lim_{M\to\infty} \left\| x(t) - \sum_{i=0}^{M-1} C_i g_i \right\|_2 = 0. \tag{27}$$

The MPD algorithm is adopted because it reduces a given signal into fewer representative components that are more easily classified. Also, for physical systems the number of iterations can be limited so that the part of the signal that contains information is decomposed while the noise is contained in the residue. First, the weighted contribution of the dictionary element that best matches the signal (or the residue) is calculated. The dictionary element that has the highest time correlation with the signal is selected, and the weighted element is then extracted from the signal. The signal residue that is left is put back into the algorithm until the stopping criteria is reached. The stopping criteria can be defined in terms of the minimum energy that is extracted from the signal or the total number of iterations of the algorithm.

4.4. Experimental setup

For this study, experiments were carried out using different damage mechanisms in metallic and composite materials. The damage types investigated were fatigue

cracking in an aluminum lug joint along with delaminations, impact damage, and tensile failure in carbon fiber composite plates.

4.4.1. Fatigue Crack

The specimen tested was a lug joint that was subjected to tensile fatigue loading as shown in Figure 32(a). The sample was machined out of Al 2024 T351. One surface of the lug joint was polished using 1200 grit silicon carbide paper so that more accurate measurements of crack length could be made using an optical telescope. The sample was tested at a load ratio of 0.1 with a maximum load of 1100lbs at 20Hz using an Instron 1331 servohydraulic test frame. Images of the crack length were taken every time the test was halted for data collection from the piezoelectric transducers using a CCD camera. Figure 32(b) shows the placement of the actuator and sensors on the structure. For the active interrogation and detection scheme used in this research, a 130 kHz Gaussian windowed sine wave was used as the excitation signal. The duration of the excitation was 500μs. The data collected from the sensors was sampled at 2MHz. Before preprocessing, each observation was downsampled to 500 kHz with a signal length of 512 points. Downsampling was feasible since the excitation was narrow band and most of the components of the sensor signal were between 100 kHz and 150 kHz, and the Nyquist frequency was still well above the maximum frequency component of the signal. It also made the matching pursuit algorithm computationally more efficient as the required dictionary size is reduced. A total of 300 observations were taken every time the damage state was measured. The fatigue experiment carried out on the lug joint resulted in five different damage states being

measured. The damage states differed in the length of the crack that was present. The different damage states are represented by C*i* where *i* represents a different damage class, corresponding to: a) C1: Healthy; b) C2: 6mm crack (27.1%); c) C3: 8mm crack; (36.2%) d) C4: 10mm crack (45.3%); e) C5: 12mm crack (54.3%). The dimensions in parentheses are relative crack lengths with respect to a total possible crack length (width of the sample) of 1.15in.

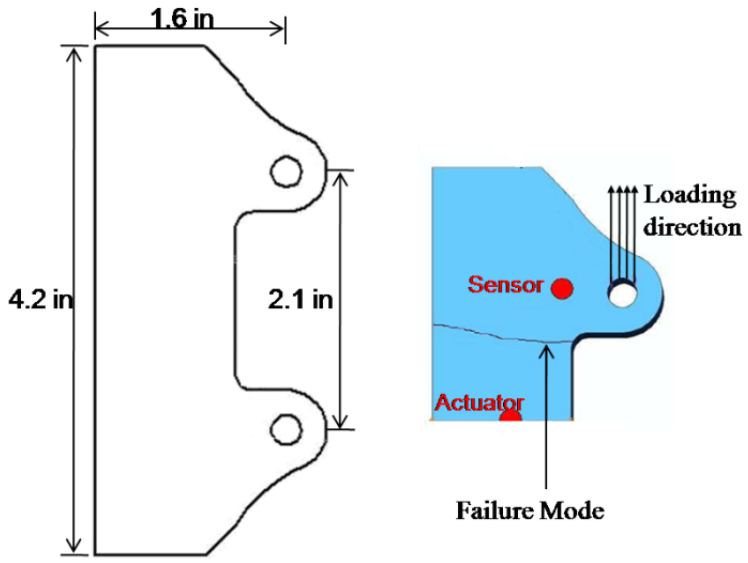

(a) (b)

Figure 32: (a) Specimen dimensions and (b) Specimen with sensor/actuator placements and failure modes

4.4.2 Delamination

Four 12”x12” composite plates each with different delamination cases were tested as shown in Figure 33. The composite material that was used for all of the composite tests was a HexPly 954-3 unidirectional carbon fiber with a cyanate

resin in a $[0,90]_{4s}$ configuration. Again, a Gaussian windowed sine wave was used as the excitation and a total of 360 signals were measured for every different delaminations scenario. A sampling frequency of 500kHz was used when acquiring the data and only data from sensor 3 was used when classifying the data. The different delaminations cases tested were: a) C1: healthy; b) C2: 5% delamination at 4^{th} interface; c) C3: square delamination at the edge of the 4th interface; d) C4: square delamination on the corner of the 4th interface.

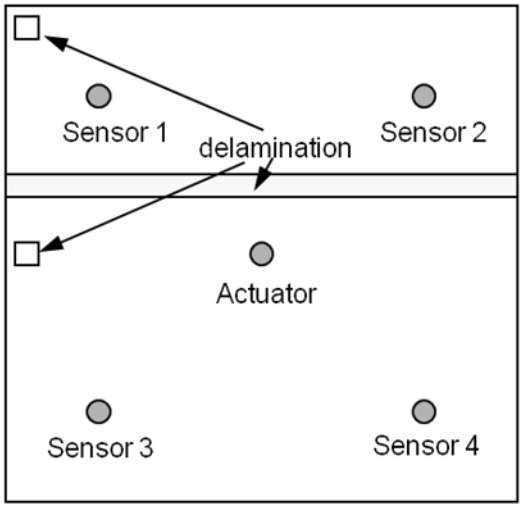

Figure 33: Composite plate with delamination and sensors

4.4.3 Impact

The coupons that were used for the impact tests are shown in Figure 34. Each coupon was impacted at a different velocity, and sensor responses due to a Gaussian windowed sine wave excitation were collected. The sampling frequency used for signal acquisition was 2MHz. A total of 150 signals were collected after impacting the sample. For the impact tests performed, the different damage types

were: a) C5: healthy; b) C6: impact velocity of 2.53 m/s; c) C7: impact velocity of 2.11 m/s; d) C8: impact velocities of 1.71 m/s.

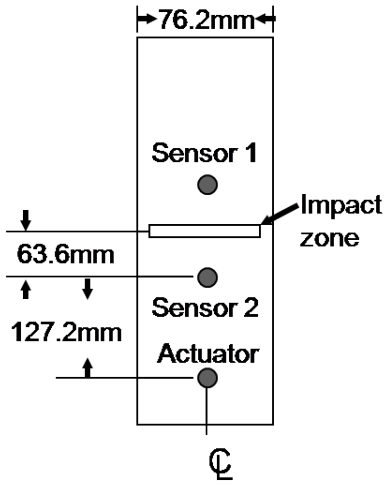

Figure 34: Dimensions of impact specimen.

4.4.4 Tensile Damage

The tensile damage in the composite specimen shown in Figure 35 was induced by first creating a notch in the specimen so that a stress concentration is created and then loading the specimen until failure. The load levels where data were collected were determined by listening to the sample being loaded until a cracking sound was heard. Then the sample was unloaded and data was collected again using a Gaussian windowed sine wave for actuation. The different damage levels were: a) Class 9: Healthy; b) Class 10: 5350 lb tensile loading; c) Class 11: 6500 lb tensile loading; d) Class 12: 7700 lb tensile loading; e) Class 13: 8800 lb tensile loading.

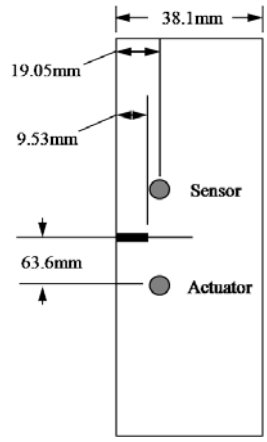

Figure 35: Tensile test specimen

4.5.Results and discussion

Data collected from the experiments were first processed using the MPD algorithm to extract features that are more easily classifiable. Figure 36(a), shows the first three principal components extracted using principal component analysis (PCA) of the raw signals that were collected during the testing of the aluminum lug joint. It can be seen from this figure that there is a tremendous amount of overlap and that accurate separation of these points in this form will be extremely difficult. The true dimension of the data being analyzed is 512x1. Figure 36(b) shows a PCA plot of the same signals after feature extraction. The feature extraction procedure reduced the dimension of the data from 512x1 to 60x1. It can be seen that even though there is still some overlap in the points, separation of these points in high-dimensional space is made easier.

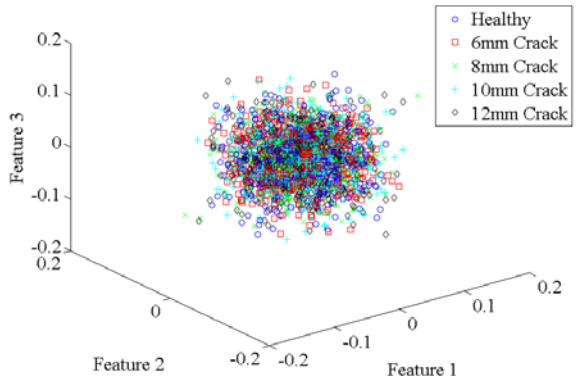

(a)

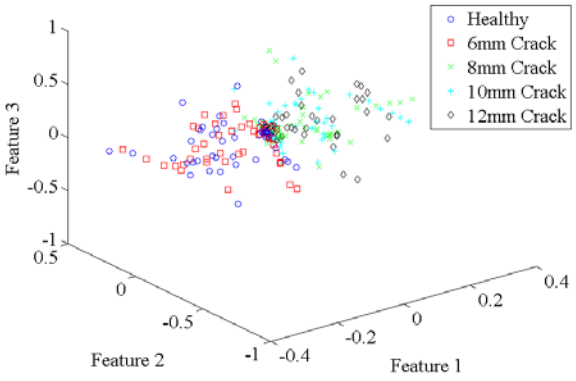

(b)

Figure 36: Principal component analysis of (a) raw signals, (b) MPD features extracted from signals

When classifying the damage state of the lug joint, training of each classifier in the binary tree was completed using 200 examples that belonged to each class. The testing of the classifier was completed using 100 data points from each damage class. A five-fold cross-validation was used to optimize the hyperparameters. The results of the classification algorithm are presented in the

nested binary confusion matrix (Table 5). From Table 1, it can be seen that the classifier performs extremely well in identifying data points that belong to C1, especially considering that a 15% error was permitted when training the classifier. This percentage was selected because of the nature of the overlap of the data patterns. It also prevented the classifier from 'over-fitting' the hyperplane to the data resulting in a loss of generalization.

For data points belonging to the other classes, a small but significant portion of the data was misclassified as belonging to C1. Since points that are positively classified are removed from the test set before further classification, the elements in every column are classification results from a smaller set of data. As an example, the number of points in C2 correctly classified was 70 out 80 test points. A drawback of this classification scheme is that the results of a classifier are dependent on the performance of classifiers that are evaluated at higher nodes in the tree.

Table 5: Results of the nested binary classification scheme (lug joint)

		Predicted Class				
		C1	**C2**	**C3**	**C4**	**C5**
Actual Class	**C1**	94	1	2	1	2
	C2	6	88	2	1	3
	C3	8	7	74	4	7
	C4	3	3	5	85	4
	C5	10	2	4	5	79

In order to better visualize the data overlap, a histogram of the normalized distance of all the points from the hyperplane is constructed (Figure 37). The histogram clearly shows that when testing the decision hyperplane, there are relatively few points from C1 that are mistakenly classified, but there is a much larger number of points belonging to C2-C5 that falls into the C1 side of the decision plane. This causes the relatively large misclassification of points belonging to C2-C5. An optimal selection of training points from C2-C5 may allow for the construction of a more accurate classifier for this case. This will be investigated in future work. Chakraborty et al. [27] have analyzed the data from this experiment and have generated classification results using a Hidden Markov Model (HMM) with 20 MPD iterations. The results obtained have a minimum correct classification rate of 88.6% as compared to the 84% average classification presented for this work in Table 1. While resulting in a slightly lower classification than the HMM algorithm, the binary tree SVM framework proposed here takes substantially less time to run. This feature will become more prominent when the size of the data sets becomes large as in real-world applications.

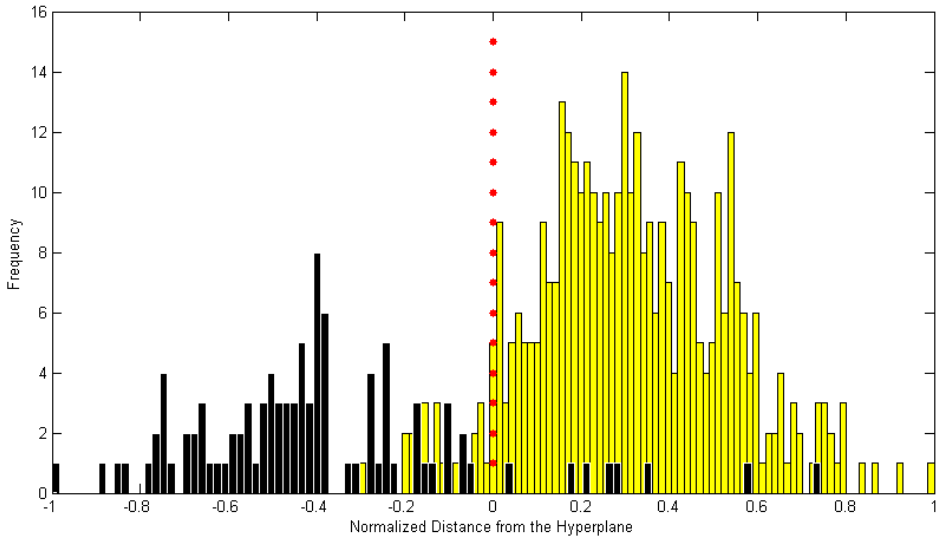

Figure 37: Histogram of distance from the optimal hyperplane

Figure 38 shows the receiver operating characteristic (ROC) curve[68] for each of the constructed classifiers. An ROC curve is a robust way to test the ability of a classifier to discriminate between classes. It allows a user to weigh the cost savings from maintaining or replacing a part after it is damaged but just before failure (true positive) against the added cost of replacing a part when it is still healthy (false positive). An ideal classifier would have a point at (0,1) which means that the classifier was able to correctly identify all the damage states and there was no overlap in the data patterns. If the data patterns do have some overlap, then false positives would occur, since the decision plane is fixed after training. The five classes being studied result in the construction of four classifiers that are constructed at different levels of the binary tree. The curves for each classifier represent the performance of each individual classifier and should not be used to judge the performance of the entire classification scheme. It can be

seen from this plot that all the classifiers have a performance that is well above the line of no-discrimination.

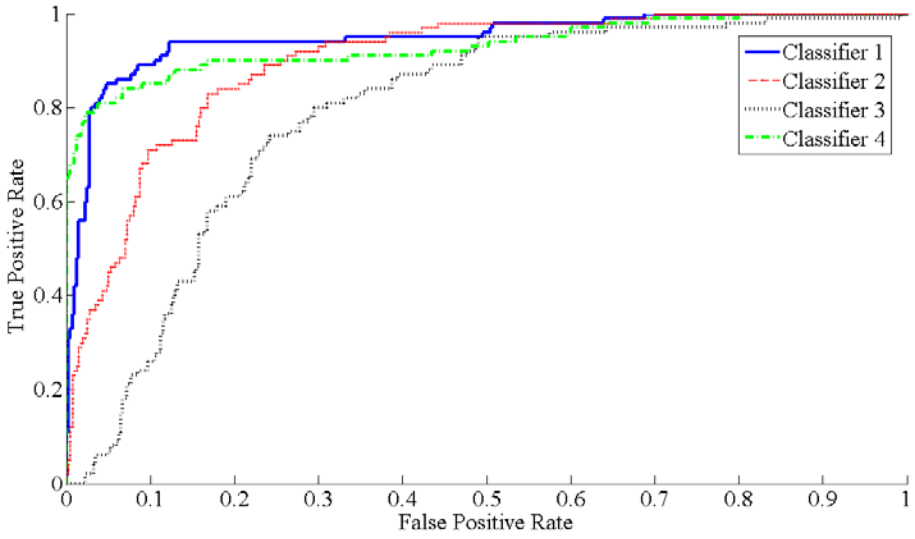

Figure 38: ROC curve for each classifier used

Next, the data from the composite experiments were analyzed in one large classification framework as shown in Figure 39. In the first level of the tree, the algorithm determines whether the damage class is delaminations, impact, or tensile. Table 6 shows the results of the first level of the classifier. For this classification, two thirds of the data was used for training and the remaining data was used for testing. It can be seen that the classifier is able to easily tell the difference between the different damage types because the interaction of the excitation signal with the different damage cases produces very different output signals.

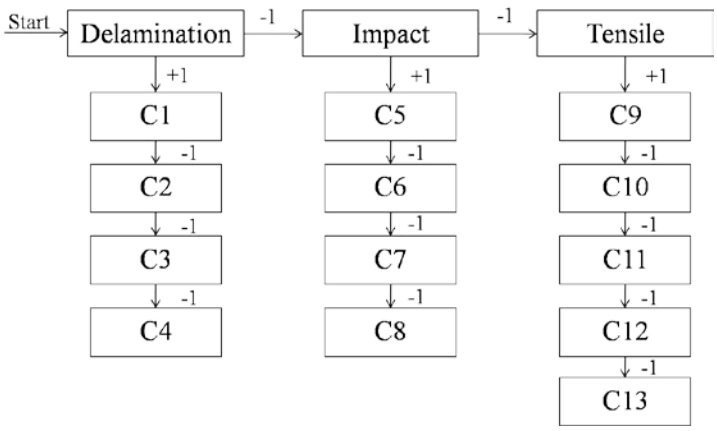

Figure 39: Organization of binary tree classifier

Table 6: Classification of damage type results (composite)

		Predicted Class		
		Delam	**Impact**	**Tensile**
Actual Class	**Delam**	1	0	0
	Impact	0	0.995	0.005
	Tensile	0	0	1

Once the class of damage is selected, the algorithm then goes on to discard data from the other damage types and then assess the extent of the determined damage type. Table 7 -Table 9, which represent level 2 in the hierarchy, show the results of the classifier within each of these damage types. In each of the level 2 classifiers, 100 data points from each class were used for training and 50 points were used for testing. The classification rates of the level 2 classifiers are not as good as the level 1 classifiers because there is more overlap in the sensor signals of a particular damage type. In the case of the seeded delaminations (Table 7), we

can see that the classifier performs very well when identifying C1-C3, but has a little trouble correctly classifying C4. This is probably because the damage is located very far from the sensor and all of the reflected waves from the corner delamination do not reach sensor 3. The high energy components that do reach the sensor are common to the signals in C1-C3, causing them to be misclassified. In the case of damage cause by impact and monotonic loading (Table 8 & Table 9), the classification tool is able to accurately classify all the damage classes C5-C13 indicating that the constructed hyperplane is able to separate the classes while avoiding significant overlap.

Table 7: Classification results for delamination

		Predicted Class			
		C1	**C2**	**C3**	**C4**
Actual Class	**C1**	0.88	0.02	0.04	0.06
	C2	0.04	0.86	0.04	0.06
	C3	0.06	0.04	0.90	0.00
	C4	0.12	0.08	0.06	0.74

Table 8: Classification results for impact damage

		Predicted Class			
		C5	**C6**	**C7**	**C8**
Actual Class	**C5**	0.88	0.04	0.00	0.08
	C6	0.10	0.82	0.02	0.06
	C7	0.06	0.02	0.90	0.02
	C8	0.02	0.04	0.04	0.90

Table 9: Classification results for tensile damage

		Predicted Class				
		C9	**C10**	**C11**	**C12**	**C13**
Actual Class	**C9**	0.90	0.04	0.02	0.02	0.02
	C10	0.06	0.88	0.02	0.00	0.04
	C11	0.08	0.04	0.80	0.06	0.02
	C12	0.04	0.02	0.04	0.86	0.04
	C13	0.08	0.00	0.04	0.04	0.84

Figure 40 shows the computational time required to build the classification tree using sensor data from the tensile test on a composite plate. It can be seen from Figure 40 that in the case of a 3-class problem, the performance of the ‘one-vs-one’ method and the binary tree method are similar but the ‘one-vs-all’ approach is not as efficient. This is because the overlap in the damage classes is significant and the time taken to optimally select the hyperparameters for a ‘one vs all’

approach is longer than the time requirement for extra comparisons required in the ‘one vs one’ approach. However, when the number of classes gets larger, the number of comparisons increases, and this starts to increase the execution time rapidly as shown in the case when 5 classes are considered. It is expected that if more data classes of this type were available, the ‘one vs one’ approach would be less efficient than the ‘one vs all’ approach. In the binary tree approach, the first comparison has the same computational intensity as a ‘one vs all’ approach. As the algorithm proceeds along the tree path, the complexity of each successive classifier is reduced until the last node, where it has the same computational intensity as a ‘one vs one’ classifier. This feature, combined with the reduced number of comparisons necessary for a k-class problem, makes it more efficient, as shown in Figure 40.

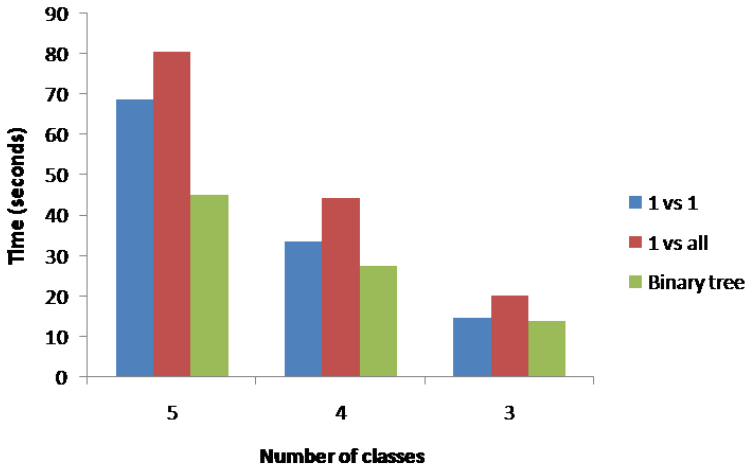

Figure 40: Computational efficiency of different SVM approaches

Chapter 5

INFORMATION MANAGEMENT FOR DAMAGE CLASSIFICATION

The ability to detect anomalies in signals from sensors is imperative for structural health monitoring (SHM) applications. Many of the candidate algorithms for these applications either require a lot of training examples or are very computationally inefficient for large sample sizes. The damage detection framework presented in this chapter uses a combination of Relevance Weighted Linear Discriminant Analysis (RWLDA) along with Support Vector Machines (SVM) to obtain a computationally efficient classification scheme for rapid damage state determination. RWLDA was used for feature extraction of damage signals from piezoelectric sensors on a lug joint and a composite plate generating data clusters that could be analyzed and reduced based on their geometric properties. This data reduction reduces the computational intensity associated with the quadratic optimization problem that needs to be solved during training.

5.1. Linear Discriminant Analysis

A classification algorithm can only perform well when it is provided with features that accurately describe the dynamics of a system. The objective of LDA is to perform dimensionality reduction while preserving as much of the class discriminatory information as possible. LDA is a supervised technique that projects data in a lower dimensional space while considering the label information of the data. In order to find the dimension reducing transformation, LDA

minimizes the scatter within each class and maximizes the scatter between classes in a reduced dimensional space. For a k class problem, finding a projection vector that provides good class separability requires consideration of the cluster means as well as the interclass scatter (S_B) and the intraclass scatter (S_W). The definition of the scatter matrices are

$$S_B = \sum_{i}^{k-1} \sum_{j=i+1}^{k} p_i p_j \left(m_i - m_j\right)\left(m_i - m_j\right)^T \tag{28}$$

$$S_W = \sum_{i=1}^{k} p_i \left(\sum_{j=1}^{C} \left(x_j - m_i\right)\left(x_j - m_i\right)^T \right) \tag{29}$$

where

$$m_i = \frac{1}{N_i} \sum_{j \in i} x_j, \tag{30}$$

C is the number of points in class *k* and p_i is the prior probability of class *i*. A good solution to the LDA problem is one where the class means are well separated, relative to the variances of each data set assigned to a particular class. For the *k* class problem considered here, (*k-1*) projection vectors (r_i) are required, so that

$$z_i = r_i^T x \Rightarrow z = R^T x \tag{31}$$

where $R = \left[r_1 \mid r_2 \mid \ldots r_{k-1} \mid\right]$. Since the problem requires a projection that maximizes the ratio of between-class to within-class scatter, the optimization problem can be stated as

$$\max J(R) = \frac{\left|R^T S_B R\right|}{\left|R^T S_W R\right|} \tag{32}$$

which can be solved as a simple eigenvalue problem.

5.2. Relevance weighting

One issue with the traditional multiclass formulation of LDA is that the resultant projection matrix is very sensitive to small changes in the smaller eigenvectors. To avoid this, a weighting parameter is introduced that reduces the effect of leverage points in the data on the smaller eigenvectors. The dissimilarity measure used for weighting, which has a form analogous to the Mahalanobis distance, is given by

$$L_{ij} = \sqrt{(m_i - m_j)^T S_w^{-1} (m_i - m_j)}. \tag{33}$$

This function effectively reduces the weighting of data points that are very different from the rest of the group allowing for the extraction of features that best represent the nominal behavior of the class. Using this metric, the scatter matrices can be modified as follows

$$S_W = \sum_{i=1}^{k} p_i r_i \left(\sum_{j=1}^{C} \left(x_j - m_i\right)\left(x_j - m_i\right)^T \right) \tag{34}$$

$$S_B = \sum_{i}^{k-1} \sum_{j=i+1}^{k} L_{ij} p_i p_j \left(m_i - m_j\right)\left(m_i - m_j\right)^T \tag{35}$$

where $r_{ij} = \sum_{j \neq i} \frac{1}{L_{ij}}$.

5.3. Feature reduction

The sample reduction algorithm that is implemented in this paper is based on the analysis of the geometry of the data clusters in space. Once the different classes of data have been separated and mapped into a feature space by the LDA algorithm (Figure 41(a)), the data points that do not contribute any information regarding the distinction of the different classes are removed. The distance metric used for this purpose is the Mahalanobis distance because it takes into account the correlations of the data set and is scale-invariant as opposed to the Euclidean distance. The expression used to calculate the Mahalanobis distance of a sample x_i from a population $X = [x_1 \mid x_2 \mid \ldots x_{k-1} \mid]$ is given by

$$d(x_i, X) = \sqrt{(x_i - \mu)^T \Sigma (x_i - \mu)} \tag{36}$$

where Σ is the covariance matrix that can be expressed in terms of the data set as

$$\Sigma = \frac{1}{N_c} XX^T \tag{37}$$

Since this is a supervised technique that uses the provided class labels for every data point, the first step is to look for the interior points in each cluster using the Mahalanobis distance. Once the distance from each data point to its respective cluster (or class) centroid is calculated, the distances are sorted and the points with the smallest distances are removed as shown in Figure 41(b).

Next, the points on the exterior of each cluster that do not affect the construction of a separating hyperplane are removed. The decision is made based on the fact that in a two-class problem, data points with a distance larger than the average distance between the two clusters are unlikely to be chosen as support vectors. Consider Figure 41(c) in which the exterior points of C1 are to be reduced. The average Mahalanobis distance from C2 to C1 and C3 to C1 is calculated as d_{21} and d_{31} respectively. The data points in C1 that have distances larger than d_{21} and d_{31} from C2 and C3 respectively, do not influence the decision boundary and can therefore be eliminated. The data points that are left are given by

$$d^2\left(x_i, N_k\right) \leq d_{ki}^2 \tag{38}$$

Figure 41(d) shows the final result of the data reduction process in 2D.

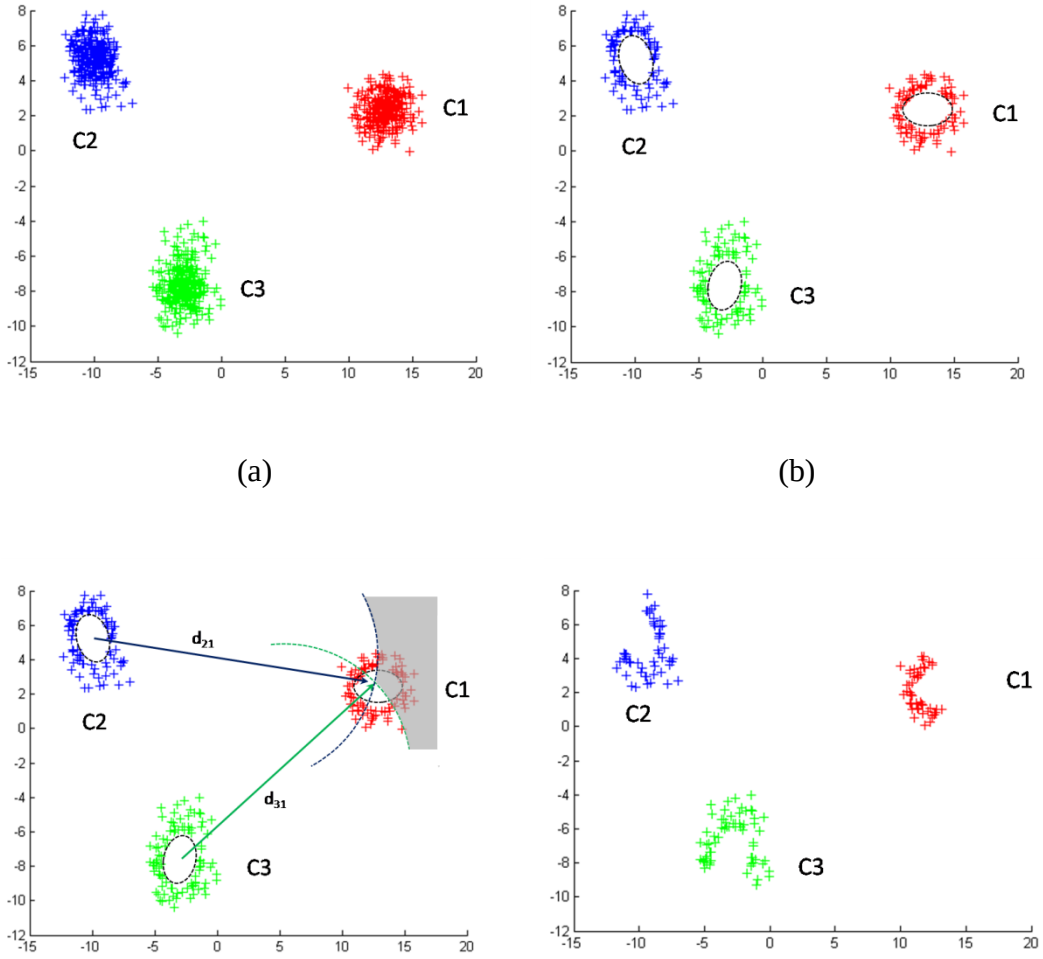

Figure 41: Illustration of data reduction procedure. (a) Initial data set projected into 2D, (b) Data clusters after removing interior data points, (c) Data points greater than the distance between cluster centroids are removed, (d) Remaining points after data reduction.

5.4. Binary tree SVM classifier

In this study, an SVM classifier organized in a binary tree structure is used to classify the detected damage type. For a five-class problem, as shown in Figure 42, the binary tree classifier is set up as follows.

Step 1. A two-class SVM is trained using pattern 1 as Class A and patterns 2, 3, 4, and 5 as Class B, and a hyperplane is constructed.

Step 2. Next, data points corresponding to pattern 1 are removed from the training set, pattern 2 is denoted as Class A, and patterns 3 and 4 are denoted as Class B for hyperplane construction.

This process is repeated until the last classifier compares the last two patterns. Further details on this approach can be found in Chapter 4.

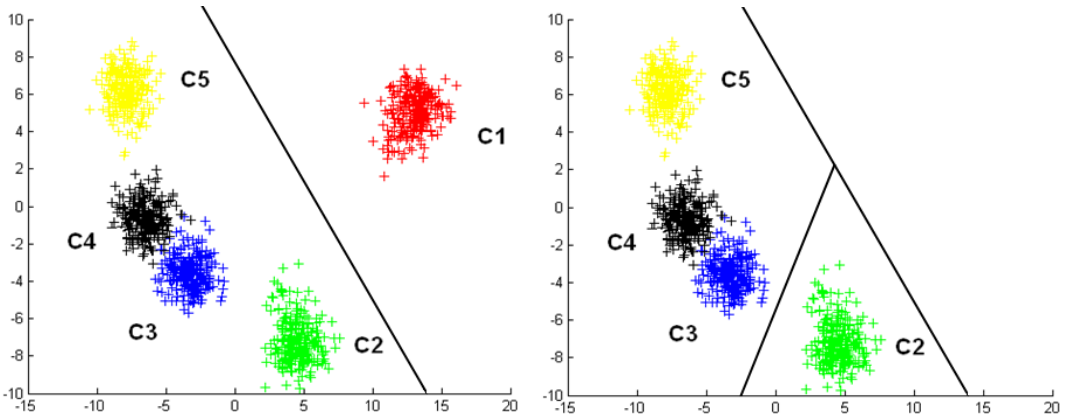

(a) (b)

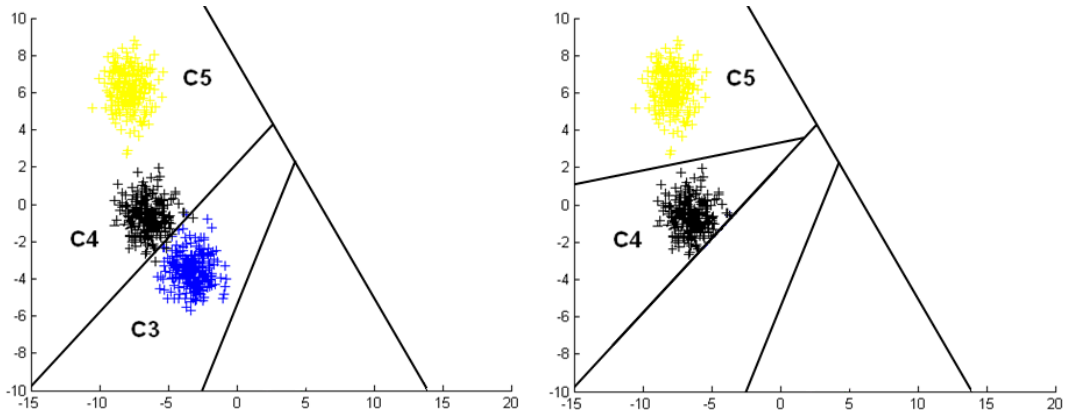

(c) (d)

Figure 42: Schematic of binary tree classification structure

5.5. Experimental setup

5.5.1. Aluminum Lug Joint

The first specimen tested was a lug joint that was subjected to tensile fatigue loading as shown in Figure 43. The sample was fabricated using Al 2024 T351 and polished using 1200 grit silicon carbide paper. The purpose of polishing was to obtain more accurate measurements of crack length using an optical telescope. The sample was tested at a load ratio of 0.1 with a maximum load of 1100lbs at 20Hz using an Instron 1331 servohydraulic test frame. The placement of the actuator and sensor are shown in Figure 43. For the active interrogation and detection scheme used in this research, a 130 kHz, Gaussian windowed sine wave with of duration 500μs was used as the excitation signal. The transient sensor response was sampled at 2MHz. Before preprocessing, each observation was downsampled to 500 kHz with a signal length of 512 points. Downsampling was feasible since the excitation was narrow band and most of the components of the

sensor signal were between 100 kHz and 150 kHz and the Nyquist frequency was still well above the maximum frequency component of the signal.

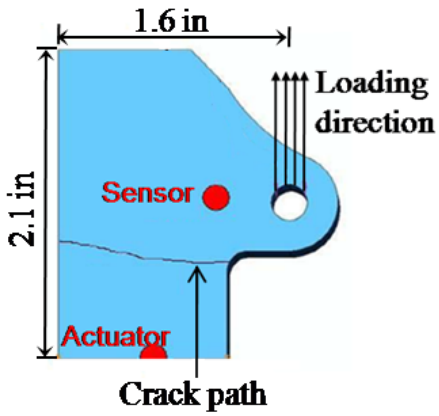

Figure 43: Sensor position and damage path in lug joint

A total of 300 observations were taken every time the damage state was measured. The fatigue experiment carried out on the lug joint resulted in five different damage states being measured. The damage states differed in the length of the crack that was present. The different damage states that were measured during the experiment were: a) C1: Healthy; b) C2: 6mm crack; c) C3: 8mm crack; d) C4: 10mm crack; e) C5: 12mm crack. Each crack length was measured from the shoulder of the lug joint.

5.5.2. Composite Plate

The data used for signal processing was collected from composite plates after different impact scenarios. Impact testing was performed on (0/90)s test specimen fabricated using unidirectional carbon fiber plies with EPON 863 epoxy and EPI-CURE 3290 hardener. The plate in the test fixture, with sensors mounted, is

shown in Figure 44(a). Figure 2(b) shows the dimensions of the square plate along with the locations of the APC 850 transducers used for data collection. Only the transducer labeled 1 was used as the actuator and transducers 2-6 were used as sensors. The samples were secured during impacting and data acquisition in a steel window frame setup (Figure 44(a)) to provide consistent boundary conditions.

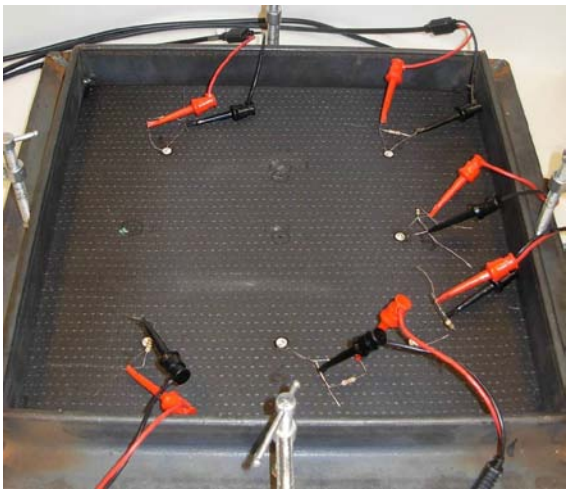

(a)

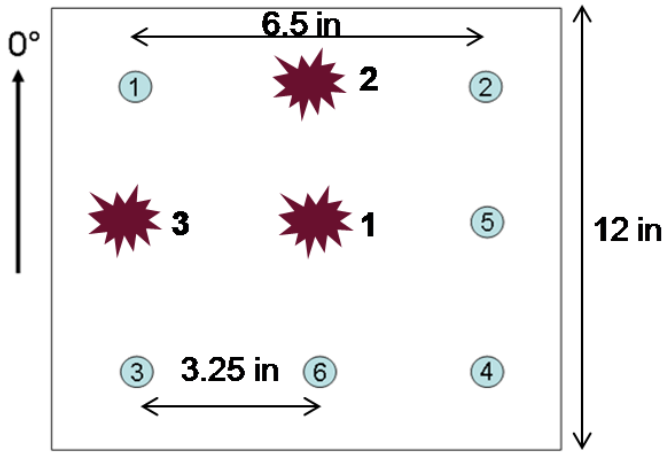

(b)

Figure 44: Experimental setup. (a) Specimen in test fixture with surface mounted transducers. (b) Dimensions of test specimen with damage sites and transducer locations

The composite plate used for testing was impacted at three locations with the order of the impact positions shown in Figure 44(b). The impact damage was induced using an inverted Charpy-style tester with a hemispherical tup 35mm in diameter. The plate was tested using an impact velocity of 5.56 m/s with an energy of 19.93 Joules. The input excitation was a 4.5 cycle burst wave with a

central frequency of 100 kHz, and the data that was collected from each of the sensors was sampled at 2 MHz. 500 observations were made at each of the damage states. Figure 45 shows a plot of the sensor response from the healthy plate and each of the damage cases.

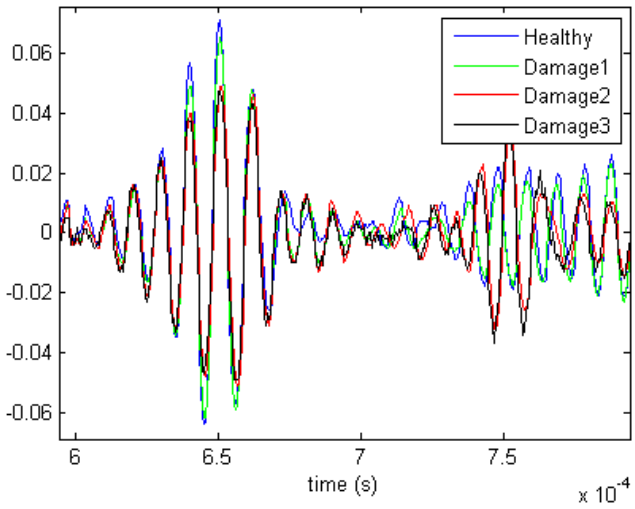

Figure 45: Sample waveforms collected before and after each impact

5.6. Results and discussion

5.6.1. Lug Joint Damage Classification

The result of the LDA when performed directly on the raw sensor data are shown in Figure 46(a). It can be seen from this plot that even in 2D, the individual damage classes are well separated. Increasing the dimension improved the separation of the classes, as expected, and the data set that was used for classification was 4D and showed the best classification results. Before the data could be reduced, a 2D histogram was generated to ensure that the clusters were globular in nature and had a Gaussian distribution, making the data reduction

possible (Figure 47). Figure 46(b) shows the same sensor data in 2D after the points close to the centroid were removed. For this study, the Mahalanobis distances of each point to their respective clusters were arranged in ascending order and the data points that were close to the center of the cluster were removed. A 70% reduction in the amount of training data was achieved by this step. The choice of how much data to remove is dependent on the geometry of the cluster and the dimensionality of the data. The results of the final step of data reduction, which involves removal of exterior points that do not influence the decision plane, are shown in Figure 46(c). The classes on the periphery of the plot can be reduced the most since there are fewer clusters surrounding them. In the case of C3 and C4, however, most of the data is retained since they are surrounded on three sides by other clusters.

Prior to the application of the data reduction algorithm, there were 260 training data points from each of the different damage classes for a total of 1330 points. By removing data points unlikely to be selected as support vectors by the classification algorithm, the data set was reduced to 313 points, which is a total reduction of over 75%.

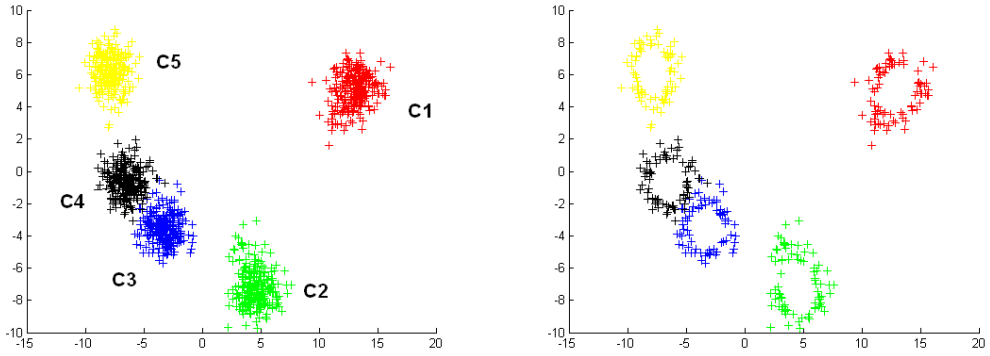

(a)

(b)

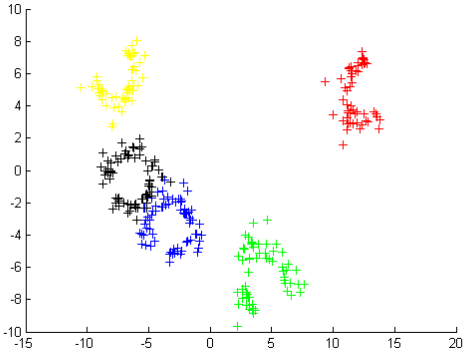

(c)

Figure 46: (a)Results of the LDA (b),(c) Results of the data reduction algorithm

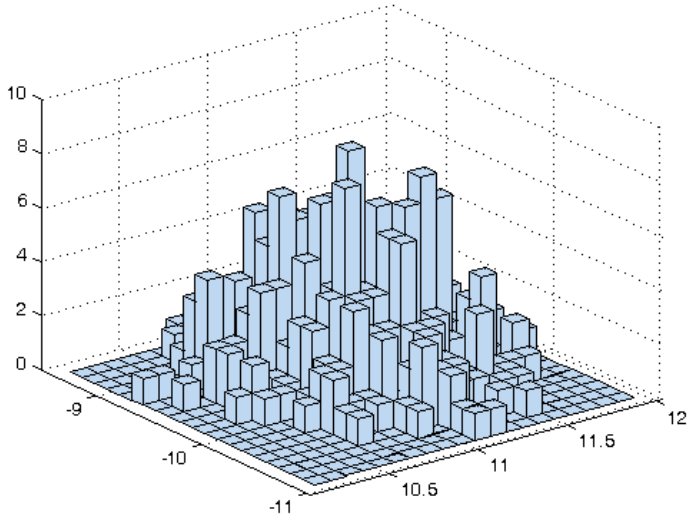

(a)

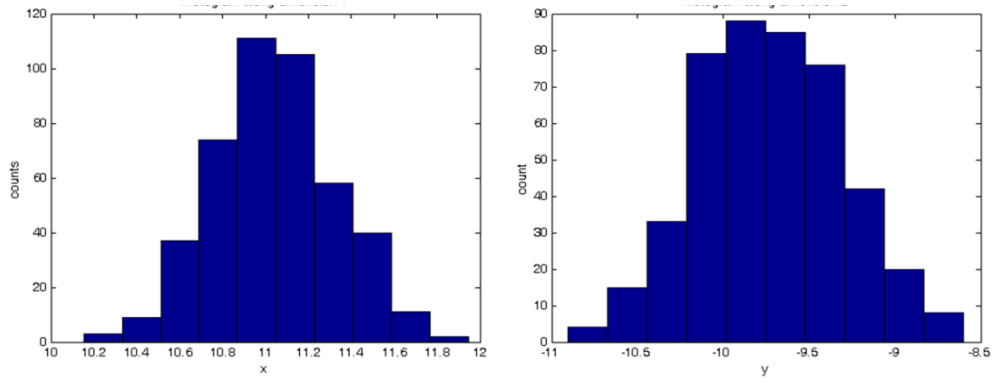

(b)

Figure 47: Histogram of healthy state data cluster (a) 2D histogram, (b) slices along each axis

Figure 48 shows the hyperplane that is constructed for the original and reduced data set. This representative figure corresponds to the first classifier that is constructed between C1 and C2-C5. The hyperplanes that are constructed before

and after data reduction use different support vectors but result in similar decision planes. Since the LDA algorithm provided a large separation between the different classes, the slight change in the hyperplane makes little difference in the confusion matrix that is generated when testing the performance of the classifier. It is also interesting to note that in Figure 48(a) the algorithm did not select any data from the two clusters in the middle as support vectors. In Figure 48(b), the algorithm used data from all the classes as support vectors, which might affect the performance depending on the variance of the test data set.

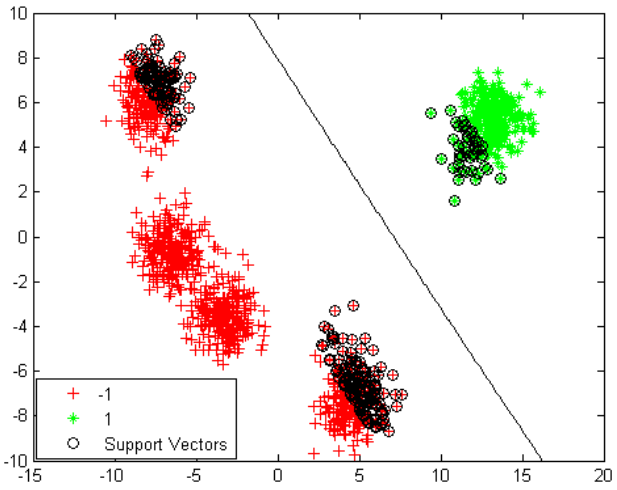

(a)

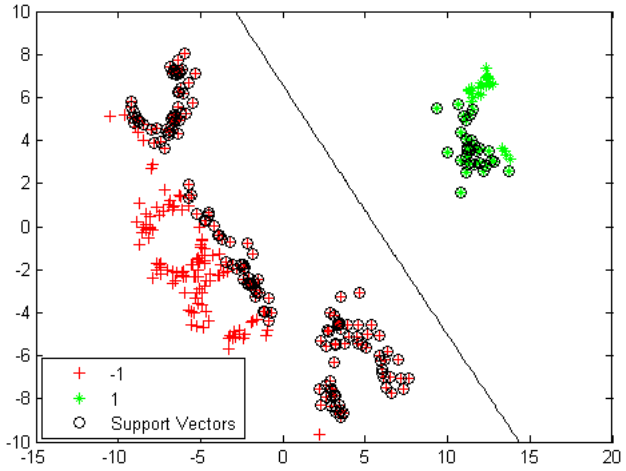

(b)

Figure 48: Decision plane for the first binary classifier for (a) the entire data set, (b) the reduced data set

The confusion matrices demonstrating the performance of the proposed binary tree classification scheme to detect crack damage in a lug joint is presented in Table 10 and Table 11. The training for each classifier used a five-fold cross-validation to optimize the required hyperparameters.

Table 10: Results of the SVM classifier without data reduction

		Predicted Class				
		C1	**C2**	**C3**	**C4**	**C5**
Actual Class	**C1**	1	0	0	0	0
	C2	0	1	0	0	0
	C3	0	0	1	0	0
	C4	0	0	0.16	0.84	0
	C5	0	0	0.12	0.08	0.8

Table 11: Results of the SVM classifier with data reduction

		Predicted Class				
		C1	**C2**	**C3**	**C4**	**C5**
Actual Class	**C1**	1	0	0	0	0
	C2	0	1	0	0	0
	C3	0	0	1	0	0
	C4	0	0	0.04	0.96	0
	C5	0	0	0.08	0.04	0.88

Table 10 shows the confusion matrix when the entire training data set is considered. While the algorithm shows 100% classification for C1-C3, there is some misclassification between C4 and C5, which can be explained by the close proximity of the clusters in the 4D space. Figure 46(a) demonstrates this closeness in 2D. The time taken to run the classification algorithm with the complete training set was 41.47s on a standard Dell XPS 1330 laptop with a T7500 processor and 3GB of RAM. Table 11 shows the results of the same problem when trained with the reduced training set. The results are similar for C1-C3 and there is a marked improvement when classifying C4 and C5. Due to the small Mahalanobis distance between C3-C4 and C4- C5, it is possible that the hyperplanes between these clusters are slightly overfitted for the case when all the data is used for training. Since there were fewer points to be selected as support

vectors after data reduction, it is possible that the resulting decision plane has better generalization. In both cases, the same 50 sensor signals were used as the unseen test set. The time taken to run the classification algorithm on this reduced data set was 24.37s which represents a reduction in CPU time of over 40% when compared with training with the full set.

5.6.2. Composite Panel Damage Classification

The data collected from the impact was first downsampled from 2 MHz to 400 kHz. Since the input excitation was a narrow band excitation centered around 100 kHz, useful sensor information with very high frequencies was expected. The data was also filtered to remove any components of the signal below 1 kHz, eliminating the noise in the signal caused by ambient conditions. In order to train and validate the classification algorithm, the data was partitioned into a mutually exclusive training and testing set. 50 signals from each class were used for testing and the rest of the data was used for training. Feature extraction was then carried out using information from sensor 2 for all damage classes. In order to show the need for relevance weighting, regular LDA was applied to two halves of the training set as shown in Figure 49. It is evident that the two data sets do not map the same even though they belong to the same classes.

For multiclass problems, LDA has problems with generalization and tends to overfit the input data set. This property, combined with the effect of leverage points in the data set, leads to extracted features that do not accurately reflect the damage class. In order to mitigate the effect of these leverage points in the data

set, relevance weighting was added to the LDA and was applied to the same data with the results shown in Figure 50.

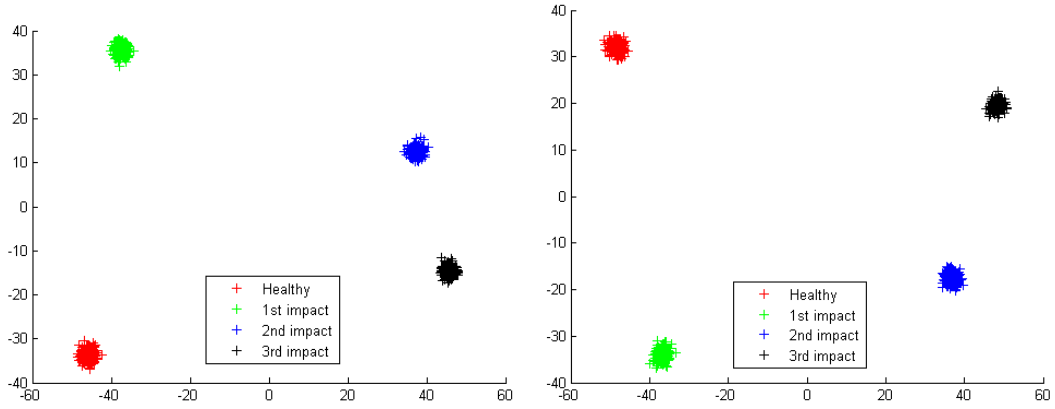

(a) (b)

Figure 49: Resulting clusters in 2D after LDA: (a) using the first half of the training set; (b) using the second half of the training set

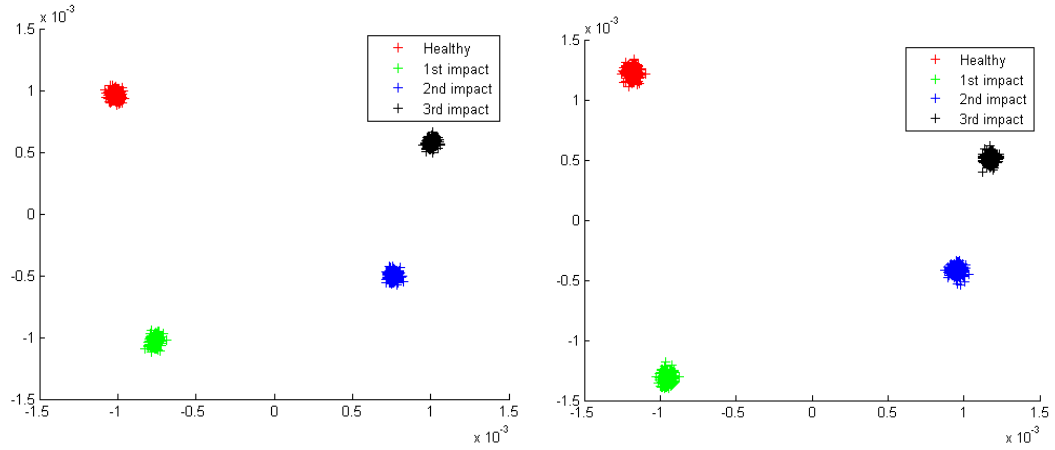

(a) (b)

Figure 50: Features extracted using RWLDA in 2D: (a) using first half of the training set; (b) using second half of the training set

By weighting the points based on their similarity or dissimilarity with the rest of the class, it is possible to reduce the effect of leverage points, allowing the extraction of more useful features for classification as shown in Figure 50. Using the RWLDA algorithm, features were extracted from the entire training set. This was followed by the feature reduction process to reduce the amount of data required to train the classifiers. A step-by-step 2D representation of the procedure is shown in Figure 51. The original training set with 450 data points per class is shown in Figure 51(a). After hollowing out the individual clusters (Figure 51(b)), the amount of data was reduced by 70%. A further 9% data reduction was achieved by eliminating exterior points that were distant from opposing clusters as depicted in Figure 51(c).

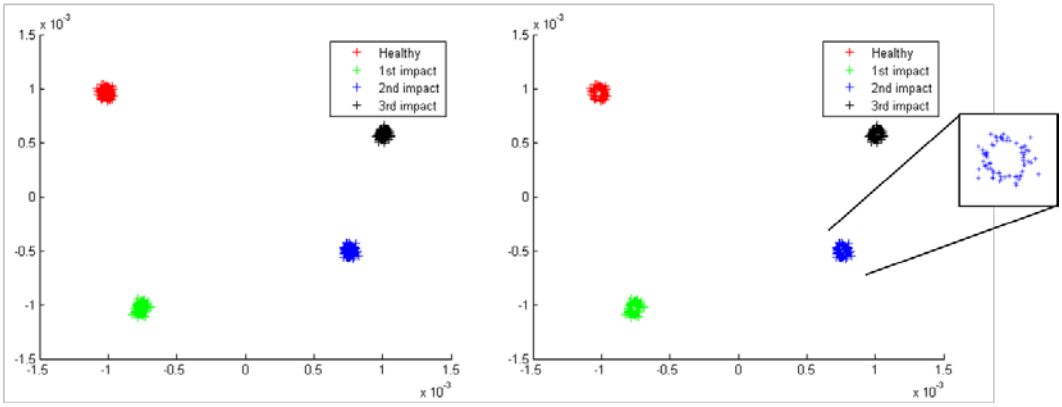

(a) (b)

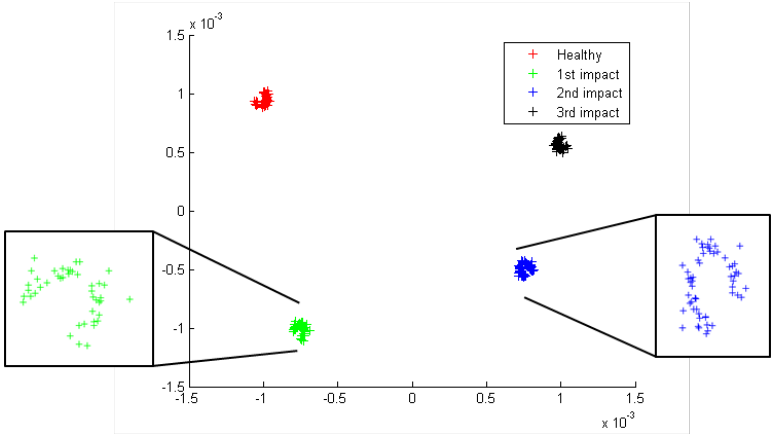

(c)

Figure 51: Results of the feature extraction process: (a) original data; (b) after removing interior data points; (c) after removal of points unlikely to be support vectors

The result of the binary tree classification on the test data showed perfect classification (Table 12). The nomenclature used in the confusion matrix is defined as C0: Healthy, C1: 1st impact, C2: 2nd impact, and C3: 3rd impact. This

result is apparent when considering the large separation between the classes as well as the generalization performance of the RWLDA (Figure 50).

Table 12: Confusion matrix showing classification results using information from sensor 2.

CR		**Actual Damage State**			
V = 0.05		**C0**	**C1**	**C2**	**C3**
Predicted Damage State	**C0**	**1**	**0**	**0**	**0**
	C1	**0**	**1**	**0**	**0**
	C2	**0**	**0**	**1**	**0**
	C3	**0**	**0**	**0**	**1**

In order to test the performance of the classifier and see the effect of material and sensor variability on the resulting sensor response, the classifier was trained using data from one sensor and tested using data from another. For this test, data from sensors 5 and 6 were used because they were equidistant from the first impact site. Since each ply in the plate is unidirectional, sensors 5 and 6 are not truly symmetric with respect to the actuator and this could cause small differences in the response of each sensor. The classification algorithm was trained using data from sensor 5 and then tested with data from the healthy and first impact damage case collected from sensor 6. The result of the classification is shown in Table 13. When data from sensor 6 corresponding to the nominal class is tested, the algorithm is able to identify it as belonging to the healthy class. However, when the first impact case is tested, the algorithm is unable to clearly discern the true class of the damage. From this result it appears that the classifier is only able to

indicate that the first impact case, as observed by sensor 6, does not belong to the healthy class. One possible explanation for this is the fact that the impact caused small regions of delamination on either side of the impactor in the direction of the surface fibers as shown by flash thermography images of the damaged plate (Figure 52). Since the damage is not symmetric with respect to either sensor, it causes differences in the sensor response that cannot be correctly classified using this data-driven approach. Another possible explanation could be that since this classification scheme is a supervised technique, any test point put into the scheme will be classified as belonging to one of the classes regardless of the true nature of the data point.

Table 13: Classification results using data from sensors 5 and 6

CR *v = 0.05*		**Predicted Damage State**			
		S5C0	**S5C1**	**S5C2**	**S5C3**
Actual Damage State	**S5C0**	**1**	**0**	**0**	**0**
	S6C0	**0.79**	**0.06**	**0.15**	**0**
	S5C1	**0**	**1**	**0**	**0**
	S6C1	**0.07**	**0.39**	**0.28**	**0.26**

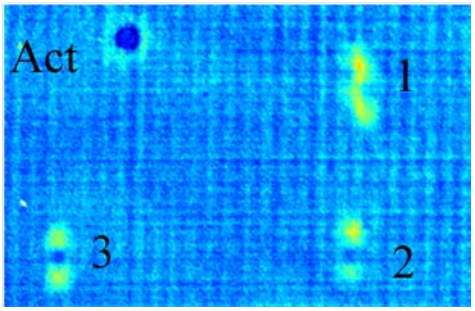

Figure 52: Echotherm image of plate 1 showing impact damage locations and actuator location

Chapter 6

LOAD HISTORY RECONSTRUCTION FOR LOW VELOCITY IMPACT

Low velocity impacts on composite plates often create subsurface damage that is difficult to diagnose. Fiber Bragg grating (FBG) sensors can be used to detect subsurface damage in composite laminates due to low velocity impact. This chapter focuses on the prediction of impact loading in composite structures as a function of time using a support vector regression approach. A time delay embedding feature extraction scheme is used since it can characterize the dynamics of the impact using the sensor signals. The novelty of this approach is that it can be applied on complex geometries and does not require a dense array of sensors to reconstruct the load profile at the point of impact. The efficacy of the algorithm has been demonstrated through simulation results on composite plates and wing structures. Trained using impact data at four locations with three different energies, the constructed framework is able to predict the force-time history at an unknown impact location on a composite plate and composite wing. Experimental validation on carbon fiber reinforced polymer wings is also presented showing low prediction errors even with small training sets.

6.1. Time Delay Embedding

As with sensor signals from piezoelectric sensors, the response collected from an FBG is a time series, which can be defined as a sequence of measurements $x(t)$ at different time instances, of an observable x acquired at regular time intervals.

Using the time delay embedding approach with this data, it is possible to reconstruct the attractor in the phase space given $x(t)$. Given a time series $x(t)$ with *N* number of data points, the state space vectors can be represented as follows,

$$y(t) = \begin{bmatrix} x(t) \\ x(t+\tau) \\ x(t+2\tau) \\ . \\ . \\ . \\ x(t+(D_E-1)\tau) \end{bmatrix} \tag{39}$$

where the time instant $t = nT_s$, T_s being the sampling time, D_E is the embedding dimension and τ is the time delay. Further details regarding a theoretical formulation of this approach have been presented in Chapter 3. The value of D_E and τ chosen for the experimental results presented here are 5 and 2.56 x 10^{-4}s, respectively. The values were chosen based on user experience. A 5-fold cross-validation on the training set was used to make sure these values were appropriate.

6.2. Support Vector Regression

SVMs [69], a popular machine learning based approach, has been adapted for regression [70] problems by using an alternative loss function. The basic idea behind is the construction of a regression line $f(\vec{x})$ that has less than an ε deviation from the target responses *y* for a majority of the training data and is at

the same time as smooth as possible. Smoothness here refers to the complexity of the constructed model. If $f(\vec{x})$ is smooth or "flat," it will be better at rejecting noise, but worse at fitting non-smooth training data when compared with non-smooth $f(\vec{x})$. This tradeoff is controlled by appropriately tuning the hyperparameters during optimization.

Consider a data set *S* that will be used to build a support vector regression model. *S* is given by

$$S = \left\{ \left(\vec{x}_i, y_i \right) \right\}_{i=1}^{m}, \quad \vec{x} \in \mathbb{R}^n, y \in \mathbb{R} \tag{40}$$

where $\vec{x}$ is a feature vector, y is a target function value, and m is the total number of training points. If this data cannot be linearly regressed as is the case with a lot of real-world data, a nonlinear regression approach is required. To solve this problem, consider the following linear estimation function [71] (Figure 53),

$$f(\vec{x}) = \vec{w} \cdot \Phi(\vec{x}) + b \tag{41}$$

where $\Phi(\vec{x})$ denotes a mapping function from the input space to a high dimensional feature space where the inputs can be linearly correlated with the system outputs, $\vec{w}$ is a weight vector, and b is a constant offset term.

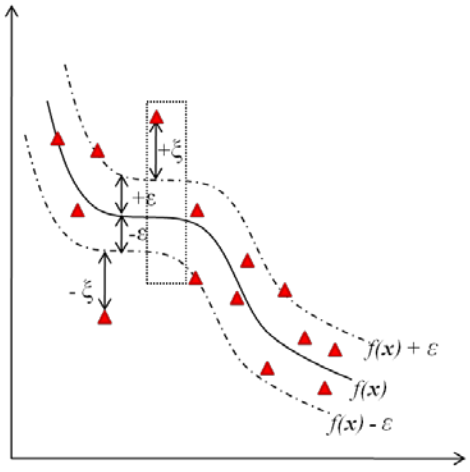

(a)

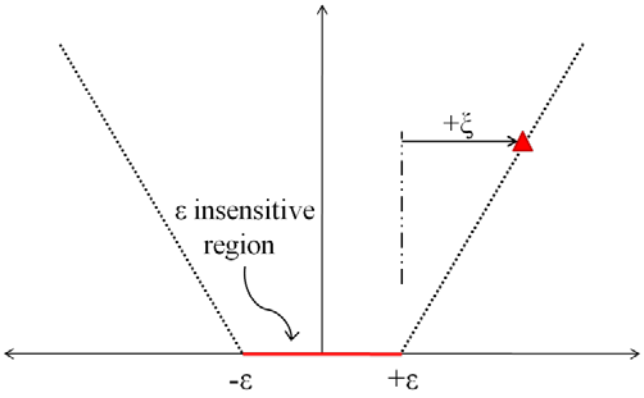

(b)

Figure 53: Schematic of (a) SVR construction and, (b) ε insensitive tube

There are a number of loss functions that can be used in the SVR formulation. Although quadratic, Laplace and Huber's loss function are common loss functions, they do not allow for the selection of a sparse set of support vectors. For this reason, an ε-insensitive loss function (Figure 53) that does not penalize data points within an ε-radius tube around the regression function is used. A

point which deviates from the regression function by an amount larger than ε, gets penalized by an amount proportional to its distance from the exterior of the ε-insensitive zone (Figure 53). These deviations on either side of the zero penalty zone are measured using the slack variables ξ and ξ^*. The loss function is given by,

$$L_\varepsilon\left(f(\vec{x}), y\right) = \begin{cases} \left|f(\vec{x}) - y\right| - \varepsilon & if \left|f(\vec{x}) - y\right| \geq \varepsilon \\ 0 & otherwise \end{cases} \tag{42}$$

The variables $\vec{w}$ and b from Equation (41) can be estimated by minimizing the risk function given by

$$R(C) = C\frac{1}{n}\sum_{i=1}^{n} L_\varepsilon\left(f\left(\vec{x}_i\right), y_i\right) + \frac{1}{2}\left|\vec{w}\right|^2 \tag{43}$$

where $\frac{1}{2}\left|\vec{w}\right|^2$ is the regularization term used to find the flattest function with sufficient approximation qualities and C is a user-defined constant controlling the tradeoff between the empirical risk (training error) and the regularization term, which penalizes complexity.

The risk function in Equation (43) can be transformed into a constrained optimization problem using the slack variables as shown.

$$\underset{w,b,\xi,\xi^*}{Min}\ R_{reg}\left(f\right) = \frac{1}{2}\left|\vec{w}\right|^2 \tag{44}$$

$$\text{subject to, } \begin{cases} y_i - \left(\vec{w}\cdot\Phi(\vec{x}_i)\right) - b \le \varepsilon + \xi_i \\ \left(\vec{w}\cdot\Phi(\vec{x}_i)\right) + b - y_i \le \varepsilon + \xi_i^* \\ \xi_i^*, \xi_i \ge 0, \quad for \quad i = 1,..,n \end{cases}.$$

Equation (44) can be converted into its dual Lagrangian form with the Karush-Kuhn-Tucker (KKT) [57] conditions of optimality to yield

$$\begin{aligned} L_d\left(\alpha,\alpha^*\right) = -\varepsilon\sum_{i=1}^{n}\left(\alpha_i^* + \alpha_i\right) + \sum_{i=1}^{n}\left(\alpha_i^* - \alpha_i\right)y_i - \\ \frac{1}{2}\sum_{i,j=1}^{n}\left(\alpha_i^* - \alpha_i\right)\left(\alpha_j^* - \alpha_j\right)K\left(\vec{x}_i,\vec{x}_j\right) \end{aligned} \tag{45}$$

$$\text{subject to } .\begin{cases} \sum_{i=1}^{n}\left(\alpha_i^* - \alpha_i\right) = 0 \\ 0 \le \alpha_i^*, \alpha_i \le C, \quad i = 1,..,n \end{cases}.$$

The KKT conditions satisfied by the solution are $\alpha_i\,\alpha_i^* = 0$. Solving the Lagrangian optimization problem, the general form of the SVR based regression function is given by

$$f\left(\vec{x}\right) = \sum_{i=1}^{n}\left(\alpha_i - \alpha_i^*\right)K\left(\vec{x},\vec{x}_i\right) + b^*. \tag{46}$$

where the optimal weight vector and bias of the regression hyperplane are given by

$$\begin{aligned} \vec{w}^* &= \sum_{i=1}^{n}\left(\alpha_i - \alpha_i^*\right)K\left(\vec{x},\vec{x}_i\right) \\ b^* &= -\frac{1}{2}\sum_{i=1}^{n}\left(\alpha_i - \alpha_i^*\right)\left(K\left(\vec{x}_i,\vec{x}_p\right) + K\left(\vec{x}_i,\vec{x}_q\right)\right) \end{aligned} \tag{47}$$

In this work, the mapping of the data from the input space to a high dimensional feature space was carried out using a Radial Basis Function (RBF) kernel[48] defined as

$$K\left(\vec{x},\vec{x}_i\right)=e^{-\frac{\left\|\vec{x}-\vec{x}_i\right\|}{2\sigma^2}} \tag{48}$$

6.3. Finite Element Model

6.3.1. Composite Plate Model

A finite element model simulating impact on a twill weave composite plate has been developed using ABAQUS Explicit. The dimensions of the plate specimen are 12in x 12in x 0.06in, and the material properties of the twill weave composite ply are presented in Table 14. A total of 15 simulations was conducted, representing impacts at five different locations (Figure 54(a)), (3,9), (4,4), (6,5), (8,3), (10,10), each with impact energies of 0.5J, 12.5J, and 50J. The bulk elastic properties along with the failure strength of the woven graphite epoxy plies are calculated at the microscale, using MAC/GMC, a micromechanics analysis based on the Generalized Method of Cells approach [72]. The four-ply laminate is modeled using continuum shell elements with clamped boundary conditions. A hemispherical impactor head (Figure 54(b)) with a 1.4in diameter is used. Hard contact and frictionless impact conditions are applied to model the interaction between the tup and the composite structure. The locations of the virtual FBG sensors, from where the strains measurements are obtained, are presented in Table 15.

Table 14: Material properties for twill weave composite.

E_{11} (GPa)	78.5600
E_{22} (GPa)	78.5600
E_{33} (GPa)	9.8330
ν_{12}	0.0252
ν_{13}	0.0392
ν_{23}	0.0392
G_{12} (GPa)	5.4170
G_{13} (GPa)	3.7860
G_{23} (GPa)	3.7860

Table 15: FBG sensor locations on the composite plate

Sensor Number	x-coordinate (in)	y-coordinate (in)	Measured strain component
S1	3.875	2.750	ε_{yy}
S2	8.125	2.750	ε_{yy}
S3	9.375	6.750	ε_{xx}
S4	6.000	9.250	ε_{yy}
S5	2.625	6.750	ε_{xx}

6.3.2. Composite Wing Model

A four-ply twill weave composite wing has also been simulated using ABAQUS Explicit. The cross-section of the wing is based on the NACA 0012 airfoil. The simulated wing has an 11in chord length and a 17in span, with simply supported

edges (Figure 55(a)). A total of 15 simulations was run consisting of impacts at 5 locations [(2,6), (5,8), (8,4), (6.5,5), (13,3)] (Figure 55(a)). The impact energies simulated at each location were 5J, 15J and 50J. Again, the material properties used in the simulation were calculated using the MAC/GMC code. Continuum shell elements were used to model the wing. Again, hard contact and frictionless impact conditions were applied to model the interaction between the tup and the composite wing. When analyzing the results of the FE simulation, it was found that the highest strain component was along the chord length so the FBG sensors were located and oriented as shown in Table 16.

Table 16: Location of FBG sensors on composite wing structure.

Sensor Number	x-coordinate (in)	y-coordinate (in)	Measured strain component
S1	2	2	ε_{xx}
S2	11	2	ε_{xx}
S3	11	9	ε_{xx}
S4	2	9	ε_{xx}

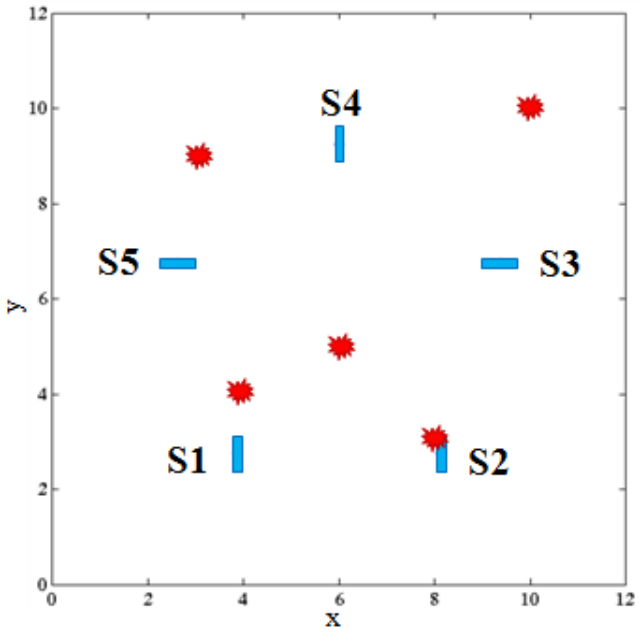

(a)

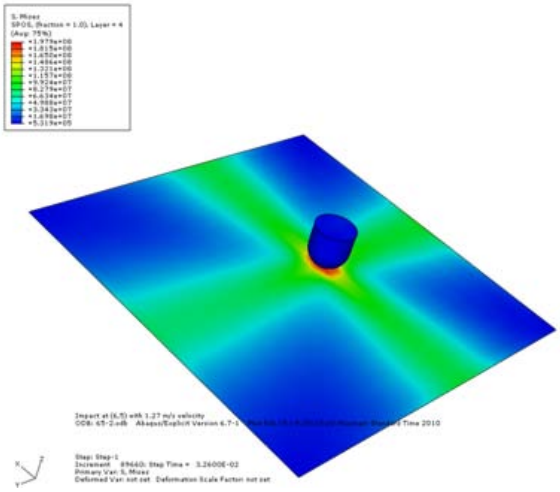

(b)

Figure 54: (a) Locations of FBGs (blue) and impacts (red) [Plate dimensions in inches], (b) finite element simulation showing impact in composite plate

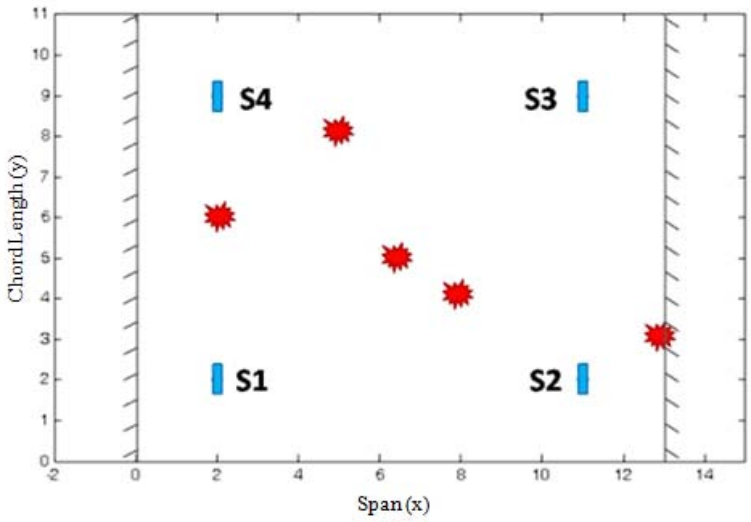

(a)

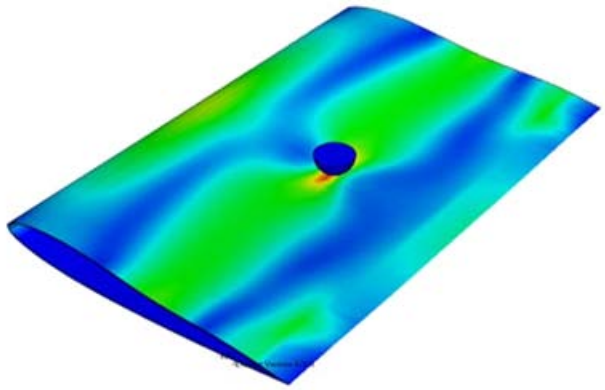

(b)

Figure 55: (a) Schematic of wing showing boundary condition, location of FBGs (blue) and impacts (red) [Plate dimensions in inches], (b) finite element simulation showing impact on a composite wing.

6.4. Results and discussion

6.4.1. Simulation Results

The data collected from the plate and wing simulations were smoothed to remove some minor perturbations in the sensor response in order to make algorithm training easier. Since the signal due to the impact is much larger than the noise present in the signal, smoothing does not adversely affect the result. To train the algorithm, strain data from four impact locations at all three energies were used to train the SVR classifier, and testing was done on the remaining unseen 50J impact. Figure 56 shows a sample load history prediction for impact at (8,4). It can be seen that the predicted loading is very similar to the simulated loading. In order to compare the time series from the simulation and the SVR algorithm, σ_{max} and area under the curve (AUC) were used. In the case of impact on a plate, the response looks Gaussian so it is possible to quantify the result in terms of the maximum value and the variance. However, for more complex structures, the response may not be Gaussian, so AUC is a better metric for evaluating the result.

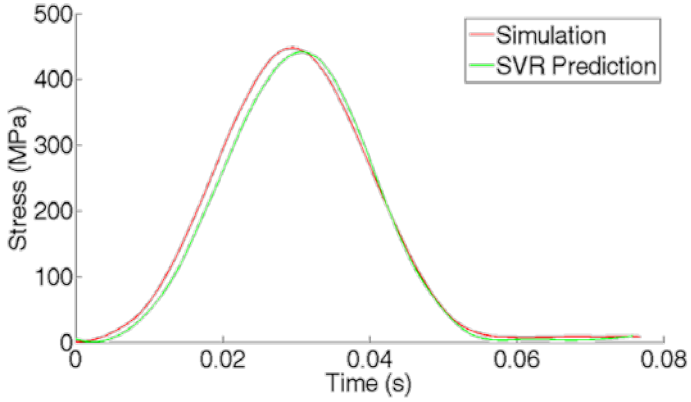

Figure 56: Simulated and predicted load history for impact at (8,4)

The results of the regression framework on a composite plate are shown in Table 17. It can be seen that the errors in the prediction of σ_{max} and AUC are less than 13 percent in all cases. It must be noted that since the simulated FBGs only measure strain in one direction, the strain information used to train the SVR algorithm is incomplete. In a complex structure where the measured loads behave more nonlinearly with variation in impact location and energy, the prediction accuracy of this approach may be adversely affected. In order to mitigate this effect, a larger training set may be used.

Table 17: Impact load history estimation result on composite plate

Impact location	Simulated σ_{max} (MPa)	Predicted σ_{max} (MPa)	Error	Simulated AUC ($x10^6$)	Predicted AUC ($x10^6$)	Error
(10,10)	895	882	1.45%	22.8	21.6	5.26%
(3,9)	988	882	10.73%	27.5	26.0	5.45%
(4,4)	753	848	12.62%	24.3	21.4	11.93%
(6,5)	780	750	3.85%	27.1	27.2	0.37%
(8,4)	821	842	2.56%	26.6	28.7	7.89%

For impact on a composite wing, strain data collected only in the direction of the chord length was used since the strains along the span were insensitive to some

impacts. Since the changes in measured strain along the chord were larger than spanwise strain changes due to varying impact positions, it would provide better prediction results. During data analysis, it was found that only sensors 3 and 4 (Figure 55(a)) contributed useful information about the impact. During the impact, the trailing edge carries only small strains and as such, the information provided by sensors in this region may not be useful. This highlights the need for careful placement of the sensors on the wing so that all the sensors are able to provide useful data. For the current set of experiments, it was found that removal of information from sensors 1 and 2 did not change the performance of the result significantly so they were ignored in the interest of computational efficiency. The SVR framework has been trained using strains from all three impact energies at four locations with the test set being the fifth unseen 50J impact. Figure 57 shows the prediction result for an impact at (5,8). It can be seen that while the algorithm is able to capture the general trend of the loading, the predicted shape differs from the simulated load.

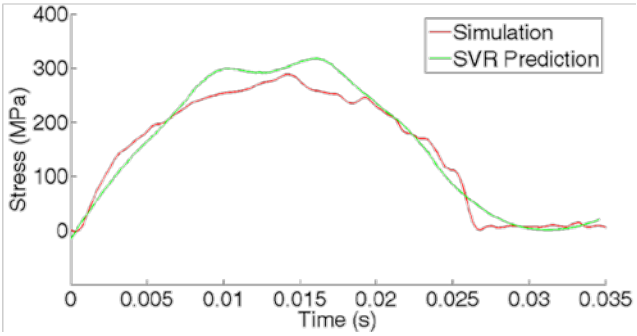

Figure 57: Simulated and SVR prediction result for impact at (5,8)

Table 18 shows the results of the load history reconstruction scheme when tested on a composite wing. For all impacts between sensors 3 and 4, the algorithm was able to estimate the load history to within 10% of σ_{max} and the AUC. For any point along the chord length, prediction results for impacts not between sensors 3 and 4 are inaccurate. One possible explanation for this might be a significant change in sensor response as the impact moves closer to the simply supported boundary condition. Inclusion of more training data closer to the simply supported region may improve the performance of the regression framework and will be investigated further in future work.

Table 18: Impact load history estimation on a composite wing

Impact location	Simulated σ_{max} (MPa)	Predicted σ_{max} (MPa)	Error	Simulated AUC ($x10^6$)	Predicted AUC ($x10^6$)	Error
(8,4)	531	514	3.20%	9.01	8.32	7.66%
(13,3)	577	479	16.98%	6.56	6.05	7.77%
(6.5,5)	541	522	3.51%	10.32	9.49	8.04%
(2,6)	639	522	18.31%	11.77	9.31	20.90%
(5,8)	576	636	10.42%	10.52	11.13	5.80%

6.4.2. Experimental Results

Experimental validation of the SVR impact estimation approach was conducted. The target variable used for prediction was the load measured by a dynamic load transducer at the tup. The input variables were the strains obtained using the

output of the four FBG sensors. Figure 58 shows an example prediction for impact at (6.5,5). Although the amount of training data is limited, the algorithm is still able to capture the general trend of the loading during impact.

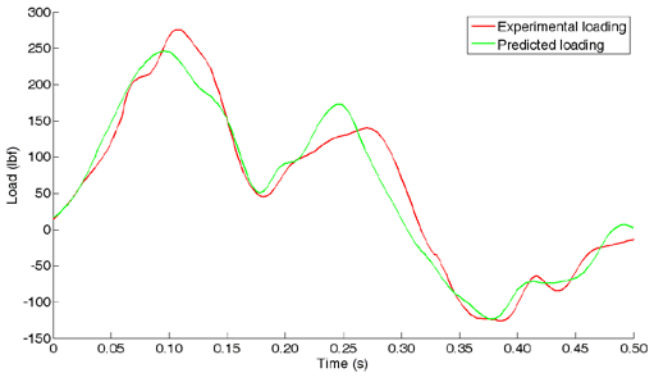

Figure 58. Experimental load cell reading and SVR prediction for impact at (6.5,5).

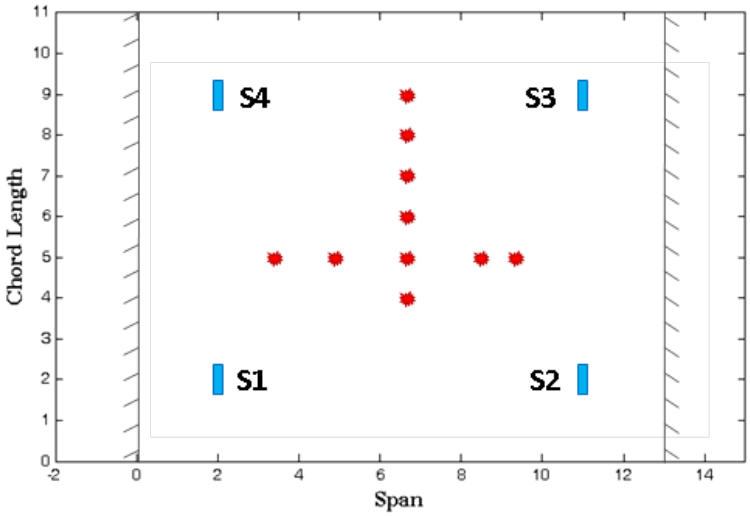

Figure 59: Locations of experimental impacts on the wing.

Table 19 shows the results of the SVR algorithm on the experimental data with the impact locations plotted in Figure 59. For impacts along the span, the algorithm was able to predict the load with accuracies greater than 90%. For impact sites along the chord length, the errors are much larger since there is a significant change in the sensor response due to varying curvature. It must also be noted that after the impact at (6.5,8) the wing started showing signs of matrix cracking and fiber breakage which became very large after the impact at (6.5,9) as shown in Figure 60. This accounts for the high prediction errors at these locations. The use of a larger training set along the chord length or knowledge of the complete strain state at every sensor location should improve prediction results along the chord length.

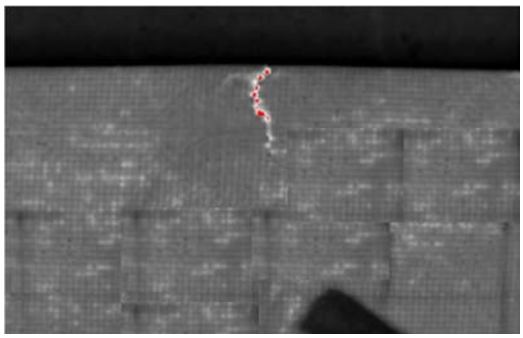

Figure 60. Thermographic image showing damage induced (red) on the leading edge of the composite wing after repeated impacts.

Table 19. Experimental prediction results for impact on a composite wing

Impact location	Expt Max Load (lbf)	Predicted Load (lbf)	Prediction Error	Expt AUC (lbf-s)	Predicted AUC (lbf-s)	Prediction Error
(3.5,5)	201.04	208.59	3.76%	2.49	2.62	5.22%
(5,5)	192.19	208.09	8.27%	2.58	2.60	0.78%
(6.5,5)	192.88	208.63	8.17%	2.54	2.61	2.76%
(8,5)	188.59	199.21	5.63%	2.47	2.55	3.24%
(9.5,5)	211.73	209.16	1.21%	2.74	2.63	4.01%
(6.5,4)	204.26	271.69	33.01%	2.49	2.98	19.68%
(6.5,5)	276.16	247.17	10.50%	2.83	2.75	2.83%
(6.5,6)	288.14	242.83	15.72%	3.05	2.60	14.75%
(6.5,7)	255.88	272.44	6.47%	2.85	2.68	5.96%
(6.5,8)	296.67	244.30	17.65%	3.47	2.60	25.07%
(6.5,9)	175.41	271.85	54.98%	2.32	2.91	25.43%

Chapter 7

SUMMARY AND FUTURE DIRECTION

The focus of the research work presented in this dissertation is on sensing and knowledge mining for SHM. The goal is to develop techniques to instrument an aerospace system with health monitoring sensors and use the collected information for continuous, reliable, and accurate structural state awareness. The proposed framework attempts to reduce the burden of manual inspection by automating the process, enabling more frequent system checks. The methods proposed have been tested on metallic specimens typically used in existing aerospace platforms and on composite specimens, which are the material system of choice for future vehicles. This dissertation addresses the following issues:

1. Sensor placement for detection of damage using Lamb waves
2. Damage detection in complex metallic joints using guided waves
3. Damage classification in metallic and composite components
4. Information management for health monitoring data
5. Estimation of load history for low velocity impact on composite structures using FBG sensors

The following sections summarize the work presented in this dissertation and suggest avenues of further research required to bring the proposed methodologies closer to the technological readiness required for implementation.

7.1. Optimal Sensor Placement

A robust actuator and sensor placement scheme is presented for interrogation of large structures using guided waves. The framework takes into account the available actuation energy, material behavior, probabilities of false alarm for the smallest detectable damage, and durability of the bonding layer. The approach places the fewest transducers such that the entire structure can be checked reliably for damage. First, the smallest detectable damage signal at an acceptable probability of false alarm is calculated. Next, the attenuation of the travelling wave in the structure is determined. Using this information, the region of the structure that could be interrogated using a pair of transducers is calculated. Since the sensing region depends on the distance between the transducers, a metaheuristic optimization algorithm is employed to find the best method to place the piezo transducers. The simulated annealing algorithm is able to solve the multiobjective optimization problem that uses user-defined weights to decide the relative importance of sensor coverage, redundancy, number of sensors, and placement of sensors for maximum durability. In order to place sensors for the longest life, a finite element analysis of the structure under expected loading is conducted and the worst case loading scenario is used. A scaled value of the stress at the sensor locations is then used to penalize sensors being placed in high stress regions. This framework is demonstrated on two complex metallic test specimens and results in the structures being completely covered using the minimum number of sensors.

In order to extend this work of sensor placement on composite systems, the region of interrogation by a pair of transducers needs to be adjusted to take into account variable attenuation as a function of orientation. More complex structures may require further modification of sensing regions to account for interfaces and thickness changes.

The framework presented in this dissertation works well for convex shaped specimens. For irregularly shaped specimens, the algorithm can be extended to include line of sight and boundary considerations. Another extension to this work would be to enable placement of other types of sensors like the FBG sensors demonstrated in Chapter 6. Since these are sensitive in only one direction, it would be very useful to know how to place them on a structure so that damage at any location can be detected.

7.2. Damage Detection

In order to detect damage in complex structures, an unsupervised machine learning tool is used in conjunction with time delay embedded features to identify the presence of a loose bolt or a crack emanating from the site of the loose bolt. Due to the complexity of the changes that occur in guided waves as they travel through such a complex structure, a purely data-driven approach is used that does not require any physics-based knowledge of the damage mechanism. The demonstrated performance of the scheme on bolted joint fatigue test data shows that it is possible to detect small damage using this approach.

Currently, this approach looks at the amount of each signal that is determined to be anomalous. Using a unique training-testing methodology, this approach is possible to determine if the data is different enough to be considered a different class of damage. The approach also uses some user-defined thresholds that may not be appropriate for real world operating conditions where environmental conditions can affect the sensor reading without causing a change in damage state. An adaptive learning method can be implemented to solve this problem. Future work can also experiment with different feature extraction techniques to determine the features that work best for a given SHM application.

7.3. Damage Classification

Once the presence of damage has been detected in a structure, the next step is to determine what kind of damage it is so that its severity and possibly cause can be assessed. To accomplish this task, a supervised version of the SVM classification algorithm was used to classify the damage that was induced in various metallic and composite test specimens. MPD was used to extract features from the collected signals, which were then classified using a binary tree SVM framework that needed fewer comparisons to classify all the available data. The results of this classification scheme were acceptable when tested on a variety of different damage types and material systems.

Before such a framework can be applied to actual systems, investigations must be conducted to see the effect of temperature and other environmental factors on the MPD features. Excessive overlap in features due to extraneous factors would

severely decrease the performance of any classifier requiring the use of alternate features. Determining features that were sensitive to the presence of damage but insensitive to environmental factors would be invaluable for SHM applications. Another route for improvement is to incorporate the dispersive effects that Lamb wave modes see as they travel through a structure into the construction of the MPD dictionary to improve decomposition accuracy in a physically meaningful way. Increases in computational efficiency can also be obtained by implementing an adaptive version of the matching pursuit algorithm.

7.4. Information Management

Aerospace systems outfitted with health and usage monitoring systems generate vast amounts of data that need to be stored and processed to make maintenance planning decisions. The work presented in Chapter 5 attempts to address this problem by reducing the amount of collected data before it could be used for damage classification. This approach uses features generated using LDA because this method shows superior performance for supervised classification of damage in metallic and composite test specimens. A relevance-weighted formulation of LDA is used for the impact testing data because the extracted features show the presence of leverage points that affect feature mapping and proposed data reduction procedures. The implementation of the relevance weighting can enable feature extraction in parts, using subsets of the training set instead of applying it to the entire training set at once. Before the extracted features could be classified, the data is reduced through analysis of the geometry class of data. Data points that would not contribute any useful information to the construction of the separating

hyperplane are eliminated, reducing the storage requirement and in some cases the classification time for the training data set. The classification scheme used was the same binary tree SVM framework used for damage classification in Chapter 4.

While this proof of concept study has shown promising results, further research is necessary to check the scalability of this approach to large data sets.

7.5. Load Reconstruction for Low Velocity Impact

In the case of low velocity impact in composite structures, knowledge of the location of the impact as well as the induced loads in important because of the possibility for subsurface damage not visible at the surface. The work proposed in Chapter 6 uses a distributed set of FBG sensors to reconstruct the loading caused by an impact of a composite wing test specimen. The approach utilizes an SVR algorithm coupled with a time embedding feature extraction to estimate the induced loads at the point of impact using only the unidirectional strain inputs from the FBG sensors. Although the sensor network provided incomplete strain information, the SVR algorithm is still able to capture the trend in strain measurements with impact load to generate a fairly good approximation of the actual loading.

Due to the large difference in sensitivity of the FBG based on its orientation, this system could be improved by an understanding of the regions on the structure that can be reliably assessed so that only sensors providing useful information can be used to do load estimation for a given impact site. Use of a high fidelity impact model to train the model would also reduce the number of training impacts

required. Variations in the angle of impact and impactor shape on the induced loads should also be considered.

REFERENCES

[1] R. A. Pyles, "Aging Aircraft: USAF Workload and Material Consumption Life Cycle Patterns" RAND, Santa Monica, CA(2003).

[2] S. K. Sethiya, "Condition Based Maintenance (CBM)," Jabalpur, (2005).

[3] H. Sohn, C. R. Farrar, F. M. Hemez *et al.*, "A Review of Structural Health Monitoring Literature: 1996–2001," Los Alamos National Laboratory, Los Alamos, NM, (2004).

[4] T. H. T. Chan, Z. X. Li, and J. M. Ko, "Fatigue analysis and life prediction of bridges with structural health monitoring data -- Part II: application," International Journal of Fatigue, 23(1), 55-64 (2001).

[5] A. Getman, C. D. Cooper, G. Key *et al.*, "Detection of mobile machine damage using accelerometer data and prognostic health monitoring techniques," 2009 IEEE Workshop on Computational Intelligence in Vehicles and Vehicular Systems, CIVVS 2009, March 30, 2009 - April 2, 2009, 101-104, (2009).

[6] C. K. Coelho, S. Das, A. Chattopadhyay *et al.*, "Detection of fatigue cracks and torque loss in bolted joints," Health Monitoring of Structural and Biological Systems 2007, 6532, 653204-12, (2007).

[7] C. Hiche, K. C. Liu, M. Seaver *et al.*, "Characterization of impact damage in woven fiber composites using fiber Bragg grating sensing and NDE," Nondestructive Characterization for Composite Materials, Aerospace Engineering, Civil Infrastructure, and Homeland Security 2009, 7294, 72940E-11, (2009).

[8] K. Worden, and A. P. Burrows, "Optimal sensor placement for fault detection," Engineering Structures, 23(8), 885-901 (2001).

[9] H. Gao, and J. L. Rose, "Ultrasonic Sensor Placement Optimization in Structural Health Monitoring Using Evolutionary Strategy," Quantitative Nondestructive Evaluation, AIP Conference Proceedings, 820, 1687-1693, (2006).

[10] B. C. Lee, and W. J. Staszewski, "Sensor location studies for damage detection with Lamb waves," Smart Materials and Structures, 16(2), 399-408 (2007).

[11] S. Das, A. Chattopadhyay, and X. Zhou, "Acoustic Based Structural Health Monitoring for Composites Using Optimal Sensor Placement: Analysis and Experiments," Journal of Reinforced Plastics, 28(1), 83-97 (2009).

[12] S. Soni, S. Das, and A. Chattopadhyay, "Optimal Sensor Placement for Damage Detection in Complex Structures," ASME Conference Proceedings, 48975, 565-571, (2009).

[13] E. Flynn, and M. Todd, "Optimal Placement of Piezoelectric Actuators and Sensors for Detecting Damage in Plate Structures," Journal of Intelligent Material Systems and Structures, 21, 265-274 (2010).

[14] E. B. Flynn, and M. D. Todd, "Bayesian probabilistic structural modeling for optimal sensor placement in ultrasonic guided wave-based structural health monitoring," Proc. SPIE, 7648, (2010).

[15] J. Skyt, C. S. Jensen, and T. B. Pedersen, "Specification-based data reduction in dimensional data warehouses," Information Systems, 33(1), 36-63 (2008).

[16] M. Şimşir, and A. Ankara, "Comparison of two non-destructive inspection techniques on the basis of sensitivity and reliability," Materials & Design, 28(5), 1433-1439 (2007).

[17] F. Aymerich, and S. Meili, "Ultrasonic evaluation of matrix damage in impacted composite laminates," Composites Part B: Engineering, 31(1), 1-6 (2000).

[18] M. Genest, M. Martinez, N. Mrad *et al.*, "Pulsed thermography for non-destructive evaluation and damage growth monitoring of bonded repairs," Composite Structures, 88(1), 112-120 (2009).

[19] Y.-H. Yu, J.-H. Choi, J.-H. Kweon *et al.*, "A study on the failure detection of composite materials using an acoustic emission," Composite Structures, 75, 163–169 (2006).

[20] C. R. Farrar, S. W. Doebling, P. J. Cornwell *et al.*, "Variability of modal parameters measured on the Alamosa Canyon Bridge," Proceedings of the 1997 15th International Modal Analysis Conference, IMAC. Part 2 (of 2), Febrary 3, 1997 - Febrary 6, 1997, 1, 257-263, (1997).

[21] S. Grondel, J. Assaad, C. Delebarre *et al.*, "Health monitoring of a composite wingbox structure," Ultrasonics, 42(1-9), 819-824 (2004).

[22] G. R. Kirikera, V. Shinde, M. J. Schulz *et al.*, "Damage localisation in composite and metallic structures using a structural neural system and simulated acoustic emissions," Mechanical Systems and Signal Processing, 21(1), 280-297 (2007).

[23] C. J. Li, and J. Ma, "Wavelet decomposition of vibrations for detection of bearing-localized defects," NDT & E International, 30(3), 143-149 (1997).

[24] H. Matt, I. Bartoli, F. L. di Scalea *et al.*, "A guided-wave system for monitoring the wing skin-to-spar bond in unmanned aerial vehicles," Smart Structures and Materials 2005: Sensors and Smart Structures Technologies for Civil, Mechanical, and Aerospace Systems, 5765, 758-768, (2005).

[25] D. Miller, S. Das, A. Chattopadhyay *et al.*, "Wave scattering analysis of bolted joints," 6176, 617603-9, (2006).

[26] Z. Su, and L. Ye, "Lamb wave-based quantitative identification of delamination in CF/EP composite structures using artificial neural algorithm," Composite Structures, 66(1-4), 627-637 (2004).

[27] D. Chakraborty, W. Zhou, D. Simon *et al.*, "Time-Frequency Methods For Structural Health Monitoring," Sensor, Signal and Information Processing (SenSIP) Workshop, (May, 2008).
[28] C. K. Coelho, W. Reynolds, and A. Chattopadhyay, "Robust feature extraction for rapid classification of damage in composites," Modeling, Signal Processing, and Control for Smart Structures 2009, 7286, 72860K-11, (2009).
[29] S. Das, A. Papandreou-Suppappola, X. Zhou *et al.*, "On the use of the matching pursuit decomposition signal processing technique for structural health monitoring," 5764, 583-594, (2005).
[30] S. Das, A. N. Srivastava, and A. Chattopadhyay, "Classification of Damage Signatures in Composite Plates using One-Class SVMs," IEEE Aerospace Conference, (2007).
[31] C. R. Farrar, H. Sohn, M. L. Fugate *et al.*, "Integrated structural health monitoring," Proc. SPIE 4335, 1-8, (2001).
[32] K. Ghartey, A. Papandreou-Suppappola, and D. Cochran, "Time-varying techniques for multisensor signal detection," IEEE Transactions on Signal Processing, 54(9), 3353 - 3362 (2006).
[33] S. Soni, S. Das, and A. Chattopadhyay, "Sensor selection and crack growth monitoring using sensitivity studies," 7286, 72860I-12, (2009).
[34] V. N. Vapnik, "Statistical Learning Theory" Wiley-Interscience, (1998).
[35] A. Chattopadhyay, S. Das, and C. K. Coelho, "Damage diagnosis using a kernel-based method," Insight - Non-Destructive Testing and Condition Monitoring, 49(8), 451-458 (2007).
[36] H. W. Park, H. Sohn, K. H. Law *et al.*, "Time reversal active sensing for health monitoring of a composite plate," Journal of Sound and Vibration, 302(1-2), 50-66 (2007).
[37] T. Shon, and J. Moon, "A hybrid machine learning approach to network anomaly detection," Information Sciences, 177(18), 3799-3821 (2007).
[38] L. Zhang, and A. K. Nandi, "Fault classification using genetic programming," Mechanical Systems and Signal Processing, 21(3), 1273-1284 (2007).
[39] P. Kudela, W. Ostachowicz, and A. Zak, "Damage detection in composite plates with embedded PZT transducers," Mechanical Systems and Signal Processing, 22, 1327–1335 (2008).
[40] G.-h. Gao, Y.-z. Zhang, Y. Zhu *et al.*, "Hybrid Support Vector Machines-Based Multi-fault Classification," Journal of China University of Mining and Technology, 17(2), 246-250 (2007).
[41] P.-Y. Hao, J.-H. Chiang, and Y.-K. Tu, "Hierarchically SVM classification based on support vector clustering method and its application to document categorization," Expert Systems with Applications, 33, 627–635 (2007).

[42] S.-F. Yuan, and F.-L. Chu, "Support vector machines-based fault diagnosis for turbo-pump rotor," Mechanical Systems and Signal Processing, 20, 939–952 (2006).
[43] D. C. Betz, G. Thursby, B. Culshaw *et al.*, "Structural Damage Location with Fiber Bragg Grating Rosettes and Lamb Waves," Structural Health Monitoring, 6(4), 299-308 (2007).
[44] T. Kundu, S. Das, S. A. Martin *et al.*, "Locating point of impact in anisotropic fiber reinforced composite plates," Ultrasonics, 48(3), 193-201 (2008).
[45] S.-J. Kim, and S.-K. Lee, "Identification of impact force in thick plates based on the elastodynamics and time-frequency method (II)," Journal of Mechanical Science and Technology, 22(7), 1359-1373 (2008).
[46] S. Lee, "Identification of impact force in thick plates based on the elastodynamics and time-frequency method (I)," Journal of Mechanical Science and Technology, 22(7), 1349-1358 (2008).
[47] J. Park, and F.-K. Chang, "System identification method for monitoring impact events," Smart Structures and Materials 2005: Smart Sensor Technology and Measurement Systems, 5758, 189-200, (2005).
[48] C. K. Coelho, S. Das, and A. Chattopadhyay, "A Hierarchical Classification Scheme for Computationally Efficient Damage Classification," Proc. IMechE, Part G: J. Aerospace Engineering, 223(G5), 497-505 (2009).
[49] Z. Huang, H. Chen, C.-J. Hsu *et al.*, "Credit rating analysis with support vector machines and neural networks: a market comparative study," Decision Support Systems, 37(4), 543-558 (2004).
[50] K.-S. Shin, T. S. Lee, and H.-j. Kim, "An application of support vector machines in bankruptcy prediction model," Expert Systems with Applications, 28(1), 127-135 (2005).
[51] S. G. Mallat, and Z. Zhang, "Matching pursuits with time-frequency dictionaries," IEEE Transactions on Signal Processing, 41(12), 3397 - 3415 (1993).
[52] A. Aragón, J. M. Alegre, and F. Gutiérrez-Solana, "Effect of clamping force on the fatigue behaviour of punched plates subjected to axial loading," Engineering Failure Analysis, 13(2), 271-281 (2006).
[53] P. Lazzarin, V. Milani, and M. Quaresimin, "Scatter bands summarizing the fatigue strength of aluminium alloy bolted joints," International Journal of Fatigue, 19(5), 401-407 (1997).
[54] J. M. Mínguez, and J. Vogwell, "Effect of torque tightening on the fatigue strength of bolted joints," Engineering Failure Analysis, 13(8), 1410-1421 (2006).
[55] F. Takens, "Lecture Notes in Mathematics" Springer, Berlin(1980).

[56] A. J. Smola, B. Schölkopf, and K.-R. Müller, "The connection between regularization operators and support vector kernels," Neural Networks, 11(4), 637-649 (1998).
[57] W. Karush, "Minima of Functions of Several Variables with Inequalities as Side Constraints," M.Sc. Dissertation, Dept. of Mathematics, Univ. of Chicago,Chicago, Illinois, (1939)
[58] K.-K. Seo, "An application of one-class support vector machines in content-based image retrieval," Expert Systems with Applications, 33(2), 491-498 (2007).
[59] N.E.Ayat, M. Cheriet, and C. Y. Suen, "Automatic model selection for the optimization of SVM kernels," Pattern Recognition, 38, 1733–1745 (2005).
[60] R. Unnthorsson, T. P. Runarsson, and M. T. Jonsson, "Model selection in one class nu-SVMs using RBF kernels," 16th conference on Condition Monitoring and Diagnostic Engineering Management, (2003).
[61] B. Schölkopf, and A. J. Smola, "Learning with Kernels: Support Vector Machines, Regularization, Optimization, and Beyond" MIT Press, Cambridge, MA(2002).
[62] C. K. Coelho, S. Das, A. Chattopadhyay *et al.*, "Detection of Fatigue Cracks and Torque Loss in Bolted Joints," Proceedings of SPIE, Smart Structures and Materials & Nondestructive Evaluation and Health Monitoring, 6532, 653204 (1-12), (2007).
[63] N. Cristianini, and J. Shawe-Taylor, "An introduction to support vector machines : and other kernel-based learning methods" Cambridge University Press, Cambridge, U.K.(2000).
[64] P. Vera-Candeas, N. Ruiz-Reyes, M. Rosa-Zurera *et al.*, "New matching pursuit based sinusoidal modelling method for audio coding," Vision, Image and Signal Processing, IEE Proceedings -, 151(1), 21-28 (2004).
[65] P. Vera-Candeas, N. Ruiz-Reyes, M. Rosa-Zurera *et al.*, "New matching pursuit based sinusoidal modelling method for audio coding," IEE Proceedings Vision, Image & Signal Processing, 151, 21 - 28, (2004).
[66] A. Papandreou-Suppappola, and S. B. Suppappola, "Analysis and classification of time-varying signals with multiple time-frequency structures," IEEE Signal Processing Letters, 9(3), 92-95 (2002).
[67] S. Ghofrani, D. C. McLernon, and A. Ayatollahi, "Comparing Gaussian and chirplet dictionaries for time-frequency analysis using matching pursuit decomposition," Signal Processing and Information Technology, 2003. ISSPIT 2003. Proceedings of the 3rd IEEE International Symposium on, 713-716, (2003).
[68] M. H. Zweig, and G. Campbell, "Receiver-Operating Characteristic (ROC) Plots: A Fundamental Evaluation Tool in Clinical Medicine," Clinical Chemistry, 39(4), 561-577 (1993).

[69] V. Vapnik, and A. Sterin, "On structural risk minimization or overall risk in a problem of pattern recognition," Automation and Remote Control, (1977).
[70] A. J. Smola, "Regression estimation with support vector learning machines," Technische Universität München,München, Germany, (1996)
[71] C.-J. Lu, T.-S. Lee, and C.-C. Chiu, "Financial time series forecasting using independent component analysis and support vector regression," Decision Support Systems, 47(2), 115-125 (2009).
[72] B. A. Bednarcyk, and A. S. M., "MAC/GMC 4.0 User's Manual. NASA/TM 2002-212077", (2002).